INVESTIGATION OF CURRENT-PHASE RELATION IN TOPOLOGICAL INSULATOR JOSEPHSON JUNCTION

BY

CAN ZHANG

DISSERTATION

Submitted in partial fulfillment of the requirements
for the degree of Doctor of Philosophy in Physics
in the Graduate College of the
University of Illinois at Urbana-Champaign, 2018

Urbana, Illinois

Doctoral Committee:

Professor Alexey Bezryadin, Chair
Professor Dale Van Harlingen, Director of Research
Professor Smitha Vishveshwara
Professor Jeffrey Filippini

ABSTRACT

In this thesis, we present current-phase relation (CPR) study of S-TI-S lateral Josephson junction (TIJJ). In a magnetic field, localized Majorana bound states (MBS) are predicted to exist at the core of Josephson vortices. One of the key characteristics of such MBS in TIJJ system is that they possess a 4π periodic CPR, instead of conventional 2π sinusoidal CPR. Our measurements of the critical current vs magnetic field modulation patterns have shown even-odd node-lifting effect in our TIJJ devices, which we interpret as evidence for a 4π-periodic $\sin\left(\frac{\phi}{2}\right)$ −component in the Josephson CPR. This has motivated a model for the nucleation and manipulation of these MBS.

We present a comprehensive study of a series of experiments designed to test in detail specific features of this model: (1) testing whether there is an even-odd pattern of node-lifting, (2) identifying irregular changes in the diffraction pattern that could indicate the abrupt entry of Majorana pairs, (3) searching for non-sinusoidal components in direct measurements of the CPR using an asymmetric SQUID technique.

ACKNOWLEDGEMENTS

The completion of this thesis is not possible without the help from many people, thus I would like to briefly express my gratitude towards them in this section.

First and foremost, this thesis is not possible without the support and guidance of my advisor, Prof. Dale Van Harlingen, who is not only a great scientist but also a great academic advisor, I felt that I am a better scientist after being trained by him, and I felt fortunate to be able to conduct my thesis research with him. I was always amazed by his ability to see through a set of complicated data and coming up with a simple, obvious, yet beautiful physical story without compromising too much of the original complicated story's authenticity. I would also like to thank all the help that I received from all the DVH group members, including Erik Huemiller, David Hamilton, Kenneth Schlax, and Adam Weis. Specifically, I am deeply indebted to Erik Huemiller, and I have to admit that I learned almost everything about dilution refrigerator and nano-fabrication techniques from him. I want to thank him for voluntarily spending many late-night hours working with me doing wire bonding, loading samples and getting ready for the cool down. I want to thank David for always ready to discuss Josephson junction physics with me. Although I had a short time overlap with Dr. Guang Yue, I have enjoyed a great deal through physics discussion with him. I would also to thank Prof. Seongshik Oh, and his students Dr. Nikesh Koirala, Maryam Salehi at Rutgers University for providing high-quality Bi_2Se_3 thin films to us.

In addition to academic collaborators and colleagues, I want to express my gratitude towards all the staff of MRL, Tao Shang, Fubo Rao, Xiaoli Wang, Mauro Sardela, Scout Maclaren, Kathy Walsh, Rick Hassch, and Steve Burdin, Doug Jeffers, Ernest Northen, for keeping the MRL facilities running, so that I can keep my experiments moving forward, and special thanks to Tony Banks for training me on using the PPMS and the QCE.

In my first few years at Urbana, I am very grateful to have the opportunity to work with Prof. Jim Eckstein, Mao Zheng, Brian Mulcahy, Carolyn Kan, from whom I learned valuable knowledge about Molecular Beam Epitaxy, and various kinds of thin film characterization techniques.

As an old saying goes, no road is long with good company. Here, I'd like to dedicate special thanks to my friends and physics classmates, Xiongjie Yu, Chi Xue, Xiaoxiao Wang, Shen Li, Xueda Wen, Yanxiang Shi, Wenchao Xu, Fei Tan, Meng Zhang, Maojin Fu, Xiao Chen, Shengmei Xu, En-Chuan Huang, Huihuo Zheng, Chao Wang, and Youngseok Kim, for giving me such a wonderful memory about my time studying at Urbana. I can still remember all the happy hours we spent together, going out for barbecues, movies, pot-luck parties, hot-pot parties, Chinese New Year Parties. Thanks to En-Chuan, who had been roommates with me for two years, I had enjoyed every conversation we had about religion, politics, and physics. Particularly, I want to thank Huihuo Zheng, and Xueda Wen, to me they are not only just hang-out friends, but also teachers in many aspects in life to me, I would not survive my first-year graduate physics course works without them. I want to thank Taylor Byrum, Jamie Byrum, Andrew Blanchard, Laine Blanchard, Keith Cassidy, for inviting me to their house to celebrate Christmas, and Fourth of July with them. I would never forget our routine Sunday basketball playing time in the first year of graduate school. However, there was never a feast, but the guest had to depart. Thank you all for running this PhD "marathon" together with me.

Furthermore, I want to thank my undergraduate professors from Minnesota, Prof. Cheng-Cher Huang and his graduate student Shun Wang, for letting me conduct research work in his lab. I would also like thank Prof. Russell Holmes, who is a great teacher. It was the two material science engineering courses taught by him that brought me into the field of condensed matter physics.

Prof. Daniel Cronin-Hennessy is my favorite undergraduate professor at Minnesota, and he is an excellent professor both in teaching and advising student doing research. If it is not for the cold weather, I would probably have stayed at Minnesota and continued doing high energy physics under his guidance, although I found out later the winter of Illinois is not much warmer than Minnesota at all. I also want to thank Glenn Kenadjian and his family for inviting me to their home for thanksgiving dinner, and helping me with a smooth transition to adapt the U.S. culture during my first semester studying in the U.S. I want to thank my high school physics teacher Mr. Ting-guo Yuan for being an excellent mentor to motivate my interest in physics.

Last and most importantly, I would like to thank my parent for their never-ending support both financially and emotionally throughout all these years since I was born, for their trusting, and for all the encouragement throughout all these years. It is beyond words that how I can describe my appreciation for my wife, Hexin Zhou. I still remember the day that we drove 8 hours together from St. Paul, to Madison Wisconsin, through Chicago and all the way to Urbana with all her stuff packed full in the back of the Volkswagen Beetle in May 2012, thank you for trusting me and moving with me. I want to thank her for the courage to believe in me, for her companionship, for her consolation when my feelings are low, for giving the birth of our lovely son Leo. I must thank my friend Qishen Zhang for fixing our Beetle numerous times in the cold winter for free, so that we can get back on the road.

This work is supported by part of the project ***Creating, Manipulating, and Detecting Majorana Fermion States in Hybrid Superconductor-Topological Insulator Josephson Devices under the award of*** **NSF DMR 16-10114**

To Baba and Mama.

To my wife Hexin, and my son Leo

TABLE OF CONTENTS

List of Abbreviations and Symbols

AFM	Atomic Force Microscopy
ABS	Andreev Bound States
BCS	Bardeen-Cooper-Schrieffer
BdG	Bogouliubov-de Gennes
CPR	Current-Phase Relation
DU	Dilution Unit
DR	Dilution Refrigerator
IPA	Isopropyl Alcohol
I_c	Critical Current
MIBK	Methyl Isobutyl Ketone
MBE	Molecular Beam Epitaxy
MBS	Majorana bound states
MFs	Majorana Fermions
Nb	Niobium
2D	2 Dimensional
2DEG	2-Dimensional Electron Gas
PMMA	Polymethyl Methacrylate
R_n	Normal State Resistance
ξ_N	Normal Metal Coherence length
SEM	Scanning Electron Microscopy
SQUID	Superconducting Quantum Interference Device
JJ	Josephson junction

TI	Topological Insulator
TIJJ	Topological Insulator Josephson junction
T_c	Critical Temperature
ZBCP	Zero Bias Conductance Peak

Chapter 1 Motivation

1.1 Introduction to Majorana Fermions

In 1928, Paul Dirac introduced the relativistic correction to the Schrodinger's equation for spin ½ massive particles. The solution to Dirac's equation was in complex form containing both real and imaginary parts, and it implied the existence of antimatter [1]. Soon after that, the positron was experimentally discovered in a cloud chamber experiment with cosmic rays, and it was later confirmed to be the antiparticle of the electrons [2]. Ettore Majorana later discovered that with a simple modification to Dirac's equations, there can be solutions to Dirac's equation composed of only a real part, which indicate that there exist spin ½ particles could be their own antiparticles [3]. This hypothetical particle was later referred to as the Majorana Fermion (MF) in the field of high energy physics, and the neutrino was often mentioned to be the most promising candidate for a Majorana Fermion. Looking for MF is not only important for fundamental science purposes, but MF is also a very promising candidate for building a fault-tolerant topological quantum computer due to its non-Abelian statistics properties in the field of condensed matter physics [4,5].

In condensed matter physics, MFs are emergent quasiparticle excitations, and they are not elementary particles as they were referred to in high energy physics. Strictly speaking a MF, different from a Dirac fermion, is a type of non-Abelian anyons, occurring only in 2D systems. Any Dirac fermion can be mathematically written as a combination of two MFs, splitting the fermion state into a real and an imaginary part. Particle-hole symmetry comes naturally with superconductivity, and we can express γ as the quasi-particle excitation creation operator from the Bogouliubov-de Gennes (BdG) equation [6],

$$\gamma_k = u_k c^+ + v_k c \tag{1}$$

where u_k , v_k are the probability amplitudes for creating and annihilating a fermionic quasi-particle. u_k , v_k satisfies $u_k^2 + v_k^2 = 1$. From particle-hole symmetry, we have

$$\gamma_k(-E) = \gamma_k^+(E) \tag{2}$$

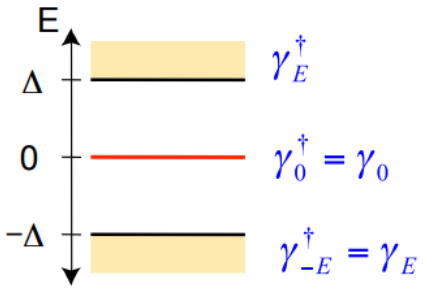

Figure 1.1: A schematic picture of quasi-particle excitation state above and below the zero-energy level [7]

As it is shown in Figure 1.1, when E=0, right at the zero-energy level, we would have the non-degenerate zero energy mode, which is called the Majorana zero-energy mode. Majorana makes the postulation of the following equation:

$$\gamma_k(0) = \gamma_k^+(0) \tag{3}$$

This is true only if $u_k = v_k$, which indicates that the total expectation value for the charge of γ_k will be zero. If we have two Majorana fermions and they collide into each other, which is often referred to as the fusion operation, the final parity state will be forced to pick a value of either 0 or 1. This is the reason why Majorana fermions are considered charge neutral quasi-particle excitations, but two Majorana fermions can turn into one electron through a fusion operation. With a unitary transformation, we can set $u_k = v_k = \frac{1}{\sqrt{2}}$, and rewrite equation 1 into:

$$c = \frac{\gamma_1 + i\gamma_2}{\sqrt{2}} \; and \; c^+ = \frac{\gamma_1 - i\gamma_2}{\sqrt{2}} \quad . \tag{4}$$

Then a MF is its own anti-particle at zero energy as defined by the following:

$$\gamma_1 = \frac{c + c^+}{\sqrt{2}} = \gamma_1^* \tag{5}$$

Thus, we can define the Fermionic number operator as follows [8]:

$$n_{ij} = c^+ c = (1 - i\gamma_1\gamma_2) \; with \, n_{ij} = 0, or \; 1 \tag{6}$$

The value of n_{ij} characterisze the two parity states of the Majorana fermion. When two Majorana fermions fuse together, we can yield a fermionic quasi-particle electron with parity n_{ij}. It is such parity states can be used to encode information and used for building a topological quantum computer.

1.2 Majorana Fermions and Topological Quantum Computing

Short coherence time and error correction have been the two major roadblocks stopping conventional superconducting qubits from scaling up. The bit-flip or dephasing error created by the Pauli matrices can only happen if there is interaction with external environment, such as through tunnel coupling and Coulomb coupling [9]. If two MFs are two spatially localized ground states having a non-negligible hopping probability amplitude, it would be difficult to address them individually. However, for quantum computation, a MF is usually referred as an unpaired MF, which arises from two MFs which are spatially separated to prevent overlap in their wavefunctions. Such highly delocalized fermionic states are protected from most kinds of decoherence, since local perturbations can only affect one MF. Therefore, low-decoherence quantum computation can be

realized by physically manipulating MFs, due to their non-Abelian statistics. This makes topological quantum computation more appealing than conventional quantum computation. For this reason, potential application in topological quantum computation, that looking for MF has attracted much attention in the field of condensed matter physics.

Read and Green pointed out that half quantum vortices (HQVs) in quasi-2D p-wave superfluid will have unpaired Majorana zero-energy states bounded at vortex cores [10]. HQVs were first proposed to exist in A-phase of superfluid 3He [11]. However, it is not very practical to make solid 2D thin films out of 3He experimentally. On the other hand, the existence of HQVs in Sr_2RuO_4 has been only recently confirmed by Budakian [12] through observing the half-height magnetization steps between fluxoid states. The non-Abelian statistics of HQVs in Sr_2RuO_4 had not been evaluated in the experiment. To test the non-Abelian statistics, one needs to perform a braiding operation on the vortices, and read out the parity before and after the braiding operation. However, Sr_2RuO_4 is a very fragile material and its superconducting transition temperature is highly susceptible to impurities and crystallographic disorder in the material, making it a very difficult material to work with [13].

However, this didn't become the primary obstacle in searching for MFs, as theorists have come up with other systems that can be used to simulate a spinless p-wave superconductor. These alternative systems are much more feasible to be implemented experimentally, yet the underlying Majorana physics are equivalent. For instance, Sau et al. have proposed a hybrid system of a conventional s-wave superconductor and a 1D semiconducting nanowire with strong Rashba spin-orbit coupling, such as InAs or InSb [14].

Several groups have reported that they have observed the elusive Majorana fermions in a nanowire system. The Kouwenhoven group observed a zero-bias-conductance peak (ZBCP) via planar tunneling spectroscopy in nanowire InSb [15]. This result was later confirmed and repeated by the Marcus group with a much stronger ZBCP and larger proximitzed superconducting gap [16]. The Van Harlingen group reported similar results in InAs nanowires [17], where they measured the change of ZBCP as a result due to hybridization of the two MFs sitting at the two ends of the wire. The ZBCP splits and reforms because of the fusing two MFs to pick one of the two parity states. However, it is well known that such ZBCP behavior can arise from many different origins, such as the Kondo effect. Whether the observation of such a ZBCP leads to the discovery of MFs remains debatable in the field of condensed matter physics. The non-abelian statistics of Majorana fermions were not tested in all these experiments.

1.3 Motivation

Another pioneering proposal was proposed by Kane and Fu [18], which involves a hybrid Josephson junction system composed of conventional s-wave superconductor contacting onto the surface of a 3D topological insulator. The topological surface states will be proximitized by the two s-wave superconducting leads on the two sides, which would behave effectively as a p-wave superconductor. In this thesis, we will mainly focus on the Kane and Fu model, and we will report our findings on a 3D topological insulator and s-wave superconductor hybrid Josephson junction system. According to theorist A. Kitaev [19], a signature characteristic of MF in a topological insulator Josephson junction (TIJJ) is that its CPR would be 4π periodic containing a $\sin\left(\frac{\phi}{2}\right)$ fractional term, rather than the conventional 2π periodic CPR, which is composed of $\sin(\phi)$ and other possible higher harmonics. The exact physics of how MF is related to the 4π

periodic Josephson effect will be discussed in the introduction to topological insulator section in Chapter 2. Furthermore, a topological insulator is an exotic material that is classified by its topological order instead of the conventional Landau symmetry breaking classification standard. Thus, it is also very important to study the CPR of a Josephson junction made on such an exotic material.

The main effort of this thesis is trying to look for a $\sin\left(\frac{\phi}{2}\right)$ term, or the 4π periodic Josephson effect, in Nb-Bi_2Se_3-Nb Josephson junction systems. Toward this goal, we have conducted the following two experiments to investigate the existence of a $\sin\left(\frac{\phi}{2}\right)$ component:

- Single junction diffraction measurements in perpendicular applied field to study the shape of the diffraction patterns at the even and odd nodes. We expect the odd nodes to be lifted due to the $\sin\left(\frac{\phi}{2}\right)$ term, and the even nodes would pin to zero due to interference effects. We observed the even-odd effect of the lifted nodes due to a combination of 2π and 4π periodic Josephson current.

- Direct CPR measurements using an asymmetric SQUID technique. Here, we have observed skewness in the CPR data for our junctions, which could be attributed to high transparency surface states. We also observed the skewness vanish as we increase the sample temperature, which could be explained by scattering effect between thermal electrons and spin-momentum locked surface state electrons.

1.4 Thesis Outline

In the first Chapter, we will talk about the motivation of this thesis project, which is to look for the existence of MFs in the field of condensed matter physics. In the next Chapter, we will introduce background knowledge about superconductivity, Josephson effect, and the concept of topological insulators. This foundation of knowledge is necessary to understand the importance of Josephson interferometry in studying CPR of TIJJ. In chapter 3, we will talk about experimental instrumentation and device fabrication techniques needed to make these topological insulator Josephson junction devices with Bi_2Se_3 MBE grown thin films, as well as measurement methods. The following 2 chapters will be the results section of each individual project. Each project has the same goal, which is to look for the $\sin\left(\frac{\phi}{2}\right)$ component in the TIJJ. In Chapter 4, we will talk about our search for $\sin\left(\frac{\phi}{2}\right)$ via measurement of even-odd node-lifting effects in the single JJ Fraunhofer diffraction pattern. In chapter 5, we will talk about how to use the asymmetric SQUID technique to directly measure the CPR of TIJJ using an electrical transport measurement. In chapter 6, the conclusion section, we will summarize our findings looking for the 4π periodic Josephson effect in a TIJJ system.

Chapter 2. Theory of Josephson junctions and topological insulators

In this chapter, we will give the theoretical background knowledge needed to understand TIJJ. The concept of superconductivity, Josephson junctions, and topological insulators are discussed first. Then, the physics of topological insulators and Josephson junction are combined. Lastly, I will describe how MF is related to the 4π periodic Josephson effect in TIJJ.

2.1 Introduction to Superconductivity

Superconductivity has been one of the most studied subjects in the field of condensed matter physics since it was first discovered in mercury by Dutch physicist Heike Kamerlingh Onnes in 1911, when he found that the electrical resistance of mercury (Hg) vanished to zero abruptly around 4K [20]. Superconductivity is a quantum mechanical phenomenon where the electrical resistance of a system becomes exactly zero below a critical temperature Tc and it becomes a perfect diamagnetic excluding all external magnetic fields.

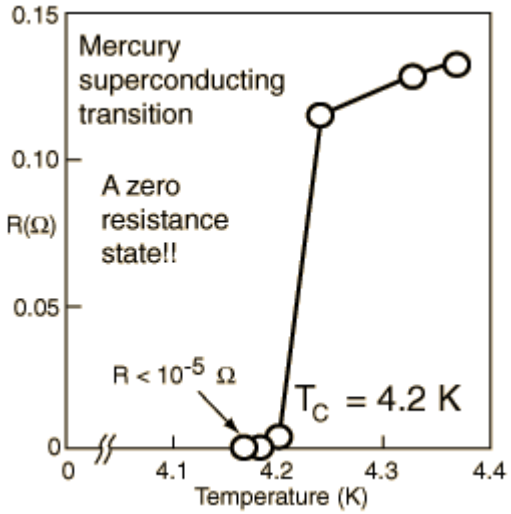

Figure 2.1: Resistance vs Temperature electrical transport data of mercury

Superconductivity appears when Cooper pairs condense into a single many-body ground state, and an energy gap $E_g = 2\Delta(T)$ opens up between the superconducting ground state and the lowest quasi-particle excitation below T_c. Here $\Delta(T)$ is the order parameter that describes the superconducting phase transition. It has units of energy, and it is approximately equal to $\Delta(T) \sim 2k_B Tc$, where k_B is Boltzmann constant and T_c is the superconducting transition temperature. A Cooper pair is a composite boson composed of two spin one-half electrons with equal but opposite momentum and spin. Even though electrons repel each other, in a superconductor there is a net attractive potential that arises due to a combination of electron screening and lattice vibration. As a conduction electron near the fermi level travels through the rigid lattice of a conductor, it draws the nearby positive ions toward it, which increases the positive charge density in the vicinity and attracts another electron passing in the opposite direction. Here is a schematic picture showing higher local positive charge density give rise to an effective attractive potential between two electrons.

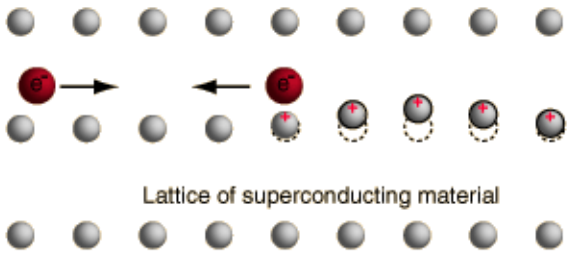

Figure 2.2: A schematic picture for conventional BCS pairing mechanism Cooper pair in a crystal lattice

This effective attractive interaction between two electrons dominates over the screened Coulomb repulsive interaction and yields a small binding energy (~1meV) for the electrons in the Cooper pair. This type of electron-phonon coupling interaction is the origin of Cooper pairing in conventional s-wave superconductor. The rigorous microscopic theory was developed by John

Bardeen, Leon Cooper, and John Schrieffer, and for which they shared the Nobel Prize in 1972. So far, the Bardeen-Cooper-Schrieffer (BCS) theory [21,22] is the most successful theory explaining the mechanism of conventional s-wave superconductivity. The notion of BCS-like pairing in more complicated materials, such as cuprates and other high T_c superconductors, is also widely believed to be true, although the nature of $\Delta(T)$ is more complicated. Superconductors can be categorized by the symmetry of Cooper pairs. Since a Cooper pair is formed by two fermions (electrons), the total wave function of paired electrons must be antisymmetric. For example, even–parity orbital states must have spin singlet states, and odd-parity orbital states must have even spin and be bound in a spin-triplet. Classification of states based on spin and orbital angular momentum is shown in Table 2.1.

Nomenclature of superconducting states

Orbital ang. momentum L	Name	Parity of spatial part	Spin state
0	s-wave	Even	Singlet
1	p-wave	Odd	Triplet
2	d-wave	Even	Singlet

Table 2.1: Classification of superconducting state [23]

The symmetry of a conventional BCS superconductor is s-wave with the total orbital angular momentum of the Cooper pair being l = 0, and correspondingly the spin state is spin-singlet. Unconventional superconductors have Cooper pair symmetry that is not s-wave, such as d-wave and p-wave, and the origin of pairing force is thought to differ from the electron-phonon assisted pairing mechanism invoked by the BCS theory. For example, J.G. Bednorz and K.A. Muller won the Nobel prize in 1986 for the discovery of high Tc cuprates $La_{2-x}Ba_xCuO_4$ (LBCO)

with T_c=35 K [24]. As of 2007, a T_c of 33 K was achieved in the organic compound superconductor RbCsC60 at ambient pressure [25]. In 2008, high T_c superconductivity was found in Fe-based superconductor $LaFeAsO_{1-x}$ with T_c = 56 K [26]. In all these systems, T_c is well beyond the theoretical limit of the electron-phonon coupling interaction, which was calculated to be 28 K by McMillan [27]. Above this limit, electron-phonon coupling is not strong enough to assist the formation of Cooper pairs compared to pairing breaking thermal fluctuations. The definitive pairing mechanism for unconventional superconductivity remains an open question in the field of superconductivity.

Although the physics behind high temperature superconductivity is still not well understood, applications of superconductivity have already widely evolved into many fields, such as the magnetic-levitation train, superconducting electric generators, lossless power transmission, and the ultrasensitive SQUID magnetometer. Particularly, intensive efforts are being put into the field of building a quantum computer using superconducting quantum circuits. In the next section of this chapter, we will discuss the basic physics of the Josephson effect due to the superconducting proximity effect.

2.2 Introduction to Josephson Effect

2.2.1 The first Josephson Equation-Current Phase Relationship (CPR)

Josephson effect is a macroscopic quantum mechanical phenomenon which was first predicted by Brian D. Josephson in 1962 [28]. A Josephson junction enables a supercurrent to flow between two pieces of superconductor with a weak link connecting them due to the tunneling of Cooper pairs. The weak link can be a thin layer (~10A) of insulator forming a SIS junction, where supercurrent is carried by Cooper pair tunneling. The weak link barrier could also be a layer (~300nm) of normal metal forming a SNS junction, where supercurrent is carried by Andreev bound states (ABS). A schematic cartoon of this effect is shown in the following figure 2.3.

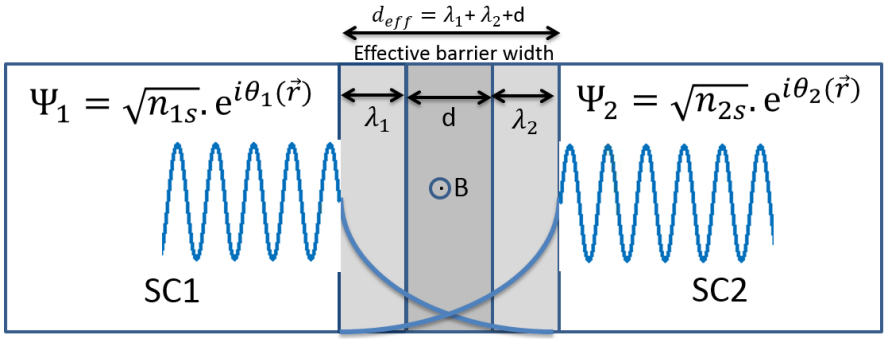

Figure 2.3: A schematic picture how supercurrent flowing across a Josephson junction due to a non-zero amplitude overlapping in the superconducting wave function on the two side of the non-superconducting junction barrier.

The superconducting wave function of the Cooper pair can be written down as

$$\Psi = \sqrt{n_s}\,.e^{i\theta(\vec{r})} \tag{7}$$

with n_s being the Cooper pair density, which is often referred to be the superconducting order parameter in superconductivity, and θ being the arbitrary phase of the wave function in the superconducting region. At the boundary of the superconductor and the weak link, where the weak

link serves effectively as a potential barrier, the sinusoidal wave function would start to decay exponentially. When the two superconducting regions on either side of the weak link have a non-zero overlap in the wave function in the barrier region, a supercurrent can flow freely without resistance across the junction. According to the definition of current density

$$J_s = q^* n_s^* v_s \tag{8}$$

where $q^* = 2e$, n_s^* is the superfluid density of Cooper pair and v_s is the velocity of the Cooper pair, the critical current density across the junction can be written as

$$J_s = q^* n_s^* \frac{\hbar}{m^*} [\nabla\theta(\vec{r}) - \frac{2\pi}{\Phi_0} A(\vec{r})] \tag{9}$$

$$J_s = J_C sin\,(\phi) \quad \text{with} \quad \phi = \theta_2 - \theta_1 - \frac{2\pi}{\Phi_0} A(\vec{r}) \tag{10}$$

In zero external magnetic field, if we integrate the supercurrent density across the junction to get the total supercurrent, we will have the first Josephson relationship, the current phase relationship (CPR):

$$I_s = \int_{-\frac{w}{2}}^{\frac{w}{2}} J_s dS \tag{11}$$

$$I_s = I_C sin\,(\phi) \tag{12}$$

Here, I_s is the actual supercurrent flowing across the junction and I_c is the maximum possible supercurrent of the junction, which is also called the critical current. I_c is independent of the current phase relationship, and it is only related to the geometry of the junction and the superconducting energy gap of the superconductor. ϕ is the phase difference of the two wave functions across the junction,

$$\phi = \int_1^2 [\nabla\theta(\vec{r}) - \frac{2\pi}{\Phi_0}A(\vec{r})] = \theta_2 - \theta_1 + \frac{2\pi}{\Phi_0}\int_1^2 \vec{A}d\vec{l} \quad (13)$$

At zero external magnetic field, we can simply write $\phi = \phi_2 - \phi_1$. This is the Gauge invariance form of phase term. In a more general form, the CPR can be written as a sum of infinite series

$$I_s(\phi) = \sum_{n=1}^{\infty} I_n sin(n\phi_n) \quad (14)$$

For Josephson junctions that are formed by conventional s-wave superconductors, the CPR is usually sinusoidal containing only the 1st order term, and all the higher order harmonics vanish to zero. The coefficient I_n is not directly related to the critical current of the junction, and it represents the amplitude of each harmonic. For Josephson junctions that are formed by unconventional superconductors, such as the d-wave superconductor LBCO, it is predicted that it should host 4e periodicity leading to a pair-density wave state corresponding with a $sin(2\phi)$ component in the CPR [29]. For topological insulator Josephson junctions, it is predicted that it should host single electron channels leading to 4π periodicity [17, 18], corresponding with a $\sin\left(\frac{\phi}{2}\right)$ component in the CPR. We will talk more about the $\sin\left(\frac{\phi}{2}\right)$ component in CPR of TIJJ in section 2.3.

2.2.2 The Second Josephson Equation- Voltage Phase Relationship

The 2nd Josephson Equation is that

$$\frac{\partial \phi}{\partial t} = \frac{2e}{\hbar} V \tag{15}$$

This shows that the rate of phase change is proportional to the potential difference of the two superconductors across the barrier. The 2nd Josephson Equation is also called the voltage phase relation. If we integrate the phase with time, we will get the following equation:

$$\phi(t) = \phi_0 + \frac{2\pi}{\Phi_0} V * t. \tag{16}$$

We plug $\phi(t)$ in to the 1st Josephson Equation, we will get:

$$I_s = I_C sin\, \phi(t) = I_C sin\, \left(\phi_0 + \frac{2\pi}{\Phi_0} V * t\right). \tag{17}$$

Thus, in this case the supercurrent oscillates with frequency $\frac{d\phi}{dt} = \frac{2\pi}{\Phi_0} V$. This is also known as the AC Josephson equation. Knowing the current phase relation and voltage phase relation, we can now calculate the amount of energy stored in the junction, which is known as the Josephson coupling energy. This characteristic energy can be understood as the binding energy of the non-zero overlap of the wave functions at either side of the junction. It can be calculated as follows:

$$E_J = \int_0^T I(t) V(t) dt \tag{18}$$

Plugging in the current phase relation and voltage phase relation, we will get

$$E_J = \int_0^T (I_c sin\, \phi\,) \left(\frac{\Phi_0}{2\pi} \frac{d\phi}{dt}\right) dt \tag{19}$$

With $\phi(0) = 0$ and $\phi(T) = \phi$, we obtain

$$E_J = \frac{I_c \Phi_0}{2\pi} \int_0^T (sin\ \phi\ ) d\phi \tag{20}$$

Which evaluates to $E_J = \frac{I_c \Phi_0}{2\pi}(1 - cos\ \phi\ )$. As one can see, when we ramp up the current through the junction and I_s reaches the maximum possible current I_c at $\phi = \frac{\pi}{2}$, the junction will switch out of the superconducting state and become normal. The energy storage and conservation in the Josephson junction indicate that the junction can be modeled as a non-linear quantized LC oscillator. Recall the current phase relation:

$$I_J = I_C sin\ \phi \tag{21}$$

To understand how the Josephson junction can be modeled as a quantized LC oscillator with capacitance and inductance, now we introduce a small variation on both sides of the equation, and obtain

$$I_J + dI = I_C sin\ (\phi + d\phi) \text{ with } dI \ll I_J \text{ and } d\phi \ll \phi \tag{22}$$

Using Taylor expansion,

$$dI = I_C cos\ \phi\ d\phi \tag{23}$$

thus

$$\frac{dI}{dt} = I_C cos\ \phi\ \frac{d\phi}{dt} \tag{24}$$

Combine the above equation with the second Josephson equation, we obtain:

$$V = \frac{\Phi_0}{2\pi}\frac{d\phi}{dt} = \frac{\Phi_0}{2\pi}\frac{1}{I_C cos\ \phi}\frac{d\phi}{dt} = L_J \frac{dI}{dt} \tag{25}$$

Where L_J is the Josephson inductance defined as:

$$L_J = \frac{\hbar}{2eI_C cos\ \phi} \tag{26}$$

We can easily see that the inductance can be modified by the bias current and initial phase difference between the two superconductors. The concept of inductance is important for studying the CPR of TIJJ in the asymmetric SQUID technique, which we will discuss in section 2.2.4.

2.2.3 Single Josephson junction in a magnetic Field

From the second Josephson relation, we can see that voltage changes alter the phase of a Josephson junction. We will now see that external magnetic field can also change the phase of a Josephson junction. Suppose we place the Josephson in an external magnetic field perpendicular to the direction of current. From equation (10) we know how the critical current density is related to the phase difference across the junction, $J_s = J_C sin\ (\phi)$. In this section, we will investigate how the phase difference relates to the critical current density when the junction is placed in an external magnetic field. The Josephson junction in a magnetic field is described in Fig. 2.4, with the field direction coming out of the page.

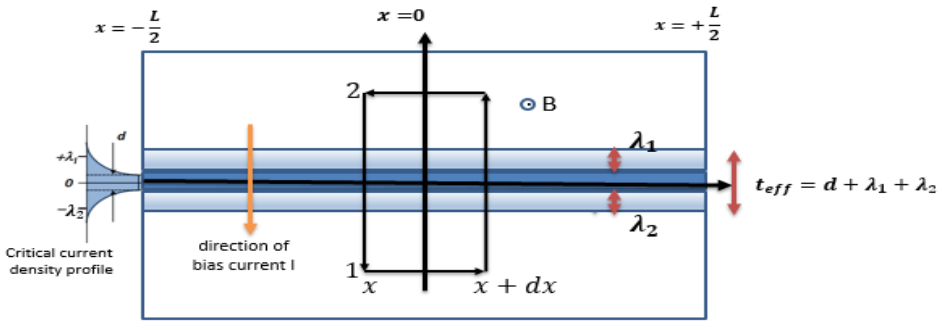

Figure 2.4: A schematic cross-sectional view of a Josephson junction in an external magnetic field

The phase along the path in figure 2.4 can be calculated as the following,

$$\phi = \theta_2 - \theta_1 + \frac{2\pi}{\Phi_0}\int_1^2 \vec{A}d\vec{l} \tag{27}$$

And now we can express ϕ_x and ϕ_{x+dx} using the above equation, and then we will have

$$\phi_{x+dx} - \phi_x = \frac{2\pi}{\Phi_0}\Phi_{x\to x+dx} \text{ and } \Phi_{x\to x+dx} = B_{ext}t_{eff}dx \tag{28}$$

$$\phi_{x+dx} - \phi_x = \frac{2\pi}{\Phi_0}B_{ext}t_{eff}dx \tag{29}$$

The above equation indicates now the phase difference across the junction is not a constant phase anymore. Instead, the phase difference between the two points along the junction x and x+dx is proportional to the magnetic flux passing through the area that is enclosed by the two points. $t_{eff} = d + \lambda_1 + \lambda_2$ is the effective thickness the Josephson junction barrier, where d is the thickness of the barrier itself, and λ is the penetration depth of the superconductor on each side. We can rewrite equation into its differential form

$$\frac{d\phi}{dx} = \frac{2\pi}{\Phi_0}B_{ext}t_{eff} \tag{30}$$

We integrate it over x, and will obtain a new general relationship of phase across the junction as a function of location x, where ϕ_0 is an arbitrary phase difference of the junction that was picked up in the integral

$$\Phi(x) = \frac{2\pi}{\Phi_0}B_{ext}t_{eff}x + \phi_0 \tag{31}$$

We plug this into the first Josephson current phase relationship equation, to get

$$J_s(x, B_{ext}) = J_c(x) sin\left(\Phi(x)\right) = J_c(x) si\, n\left(\frac{2\pi}{\Phi_0} B_{ext} t_{eff} x + \phi_0\right) \quad (32)$$

As we can easily see from the above equation, the critical current density oscillates as a sinusoidal function with respect to both location *x*, and external B field. This tells us that at a different location on the junction, the critical current density varies. To get the total current flowing across the junction, we perform an integral along the whole junction in the x direction:

$$I_s(B_{ext}) = \int_{-\frac{L}{2}}^{\frac{L}{2}} J_c(x) \sin\left(\frac{2\pi}{\Phi_0} B_{ext} t_{eff} x + \phi_0\right) dx \quad (33)$$

Due to the physical constraint that J_c=0 outside the range of $\pm\frac{L}{2}$, we can change the integral range from $x = \pm\frac{L}{2}$ to $x = \pm\infty$, set $\frac{2\pi}{\Phi_0} B_{ext} t_{eff} = k$ and sin(kx)=Im{ k^{ikx}} in order to get

$$I_s(B_{ext}) = Im\{e^{i\phi_0} \int_{-\infty}^{\infty} J_c(x) e^{ikx} dx\} \quad (34)$$

and

$$I_s(B_{ext}) = I_c(0) sin\phi_0 \left| \frac{\sin\left(\frac{\pi\Phi}{\Phi_0}\right)}{\frac{\pi\Phi}{\Phi_0}} \right| \quad (35)$$

where $\Phi = B_{ext} t_{eff} L$ is the enclosed flux of the entire junction due to external magnetic field, and $I_c(0) = LJ_c$ is the total current at zero field. At $\phi_0 = \pm\frac{\pi}{2}$, the total critical current I_s is maximized and positive. The result of the integral is now a Fourier transform of the current density as a function of B field. Due to the mathematical similarity of this equation to the diffraction equation in optics, the result of this equation is also called the Fraunhofer diffraction pattern of critical current vs B field.

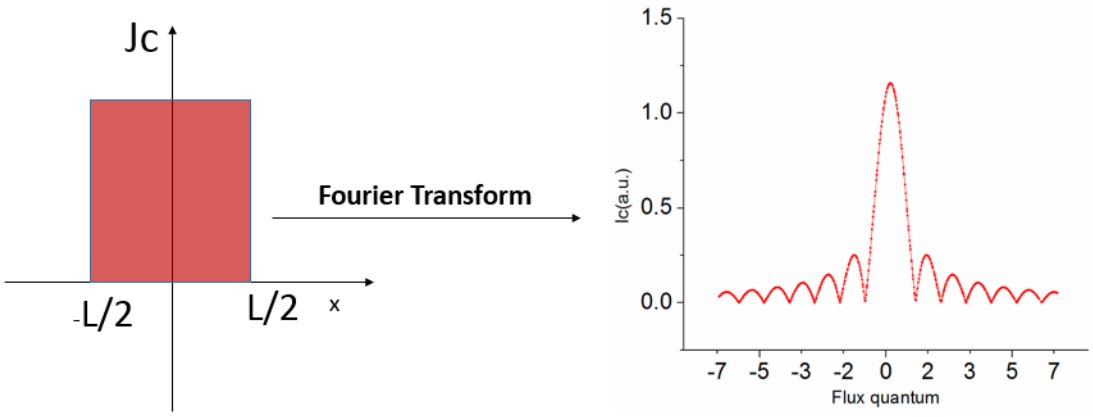

Figure 2.5: Fourier transforming a square function of uniform current density in an external magnetic field yields a I_c vs B pattern analogous to optics Fraunhofer diffraction pattern.

In figure 2.6, we show 4 subplots of the local critical current density of function of the total flux in the junction due to an external magnetic field. The length of the arrow indicates the magnitude of the local current density, and direction of the arrow can be understood as the current flowing direction, which is related to the phase difference at that specific location between the two superconductors. At zero field, the total flux in the junction is zero, and the critical current density $J_s(x, B_{ext} = 0) = J_c sin\,(\phi_0))$ is a constant across the junction along x direction, which is the situation in Figure 2.6 (i). When we start increasing the external magnetic field, $J_s(x, B_{ext}) = J_c sin(\phi(x))$, and $\phi(x) = \frac{2\pi}{\Phi_0}\Phi + \phi_0$. When the total flux is $\Phi = \frac{\Phi_0}{2}$, $\phi(x) = \pi\frac{x}{L} + \phi_0$ and thus $J_s(x) = J_c sin\,(\pi\frac{x}{L} + \phi_0)$. Then, the local critical current density of each spot would behave as shown in situation in (ii) of figure 2.6. When $\phi_{total} = \Phi_0$, J_s would oscillate over a full period of $sin\,(\pi\frac{x}{L} + \phi_0)$, and we would have equal parts positive and negative current along the junction. The total current in the junction would then add up to zero.

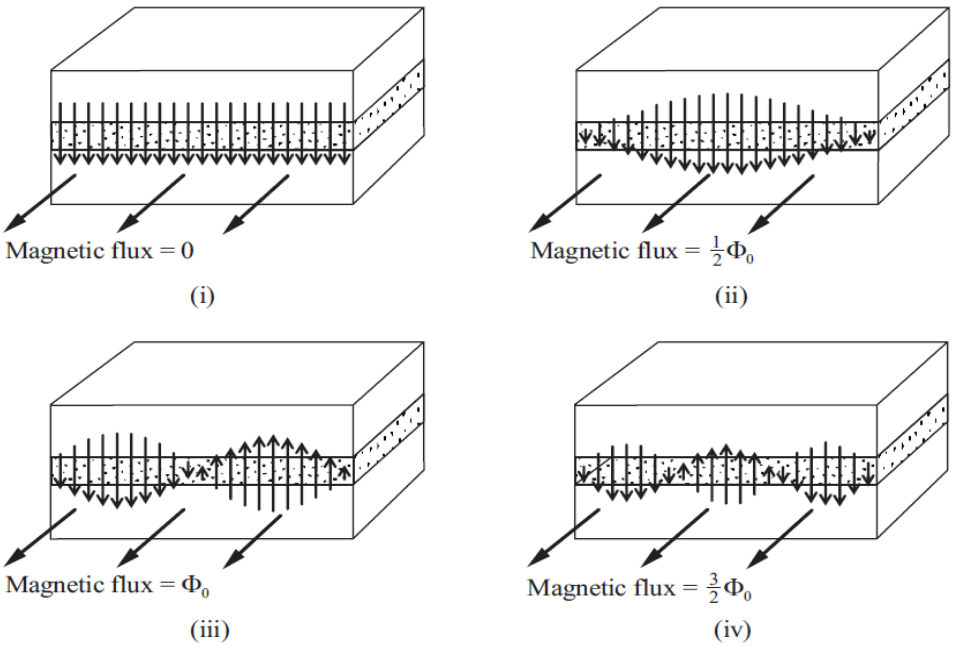

Figure 2.6: Cross-sectional view of local critical current magnitude as function of local phases at different external field strength [30].

In all the above situations, we are only considering the short Josephson junction regime, where the magnetic field generated by the supercurrent in the junction itself is negligible. In other words, the Meissner screening effect is ignored, which is also referred as the flux focusing effect. When we make the junction too long or the barrier too thin, where d is small compared to the penetration depth of the superconductor, the critical current of the junction is so large that it would generate a magnetic field to screen out the external B field through the junction. In this case the critical current density distribution becomes complicated, and it is usually referred to as the long junction limit, and we will not study this type of junction. For this thesis, all the junctions that we made are within the short junction limit, where the flux focusing effect can be ignored.

2.2.4 Superconducting Quantum Interference Device

Another type of Josephson junction device we will be studying in this thesis is called a superconducting quantum interference device (SQUID), A SQUID is one of the most sensitive magnetometers in existence, and it can be used to measure magnetic fields as small as 5×10^{-18} T. The SQUID is a powerful tool to study the CPR physics of Josephson junctions. A SQUID has two Josephson junctions in parallel sitting in superconducting loop, as shown in figure 2.7.

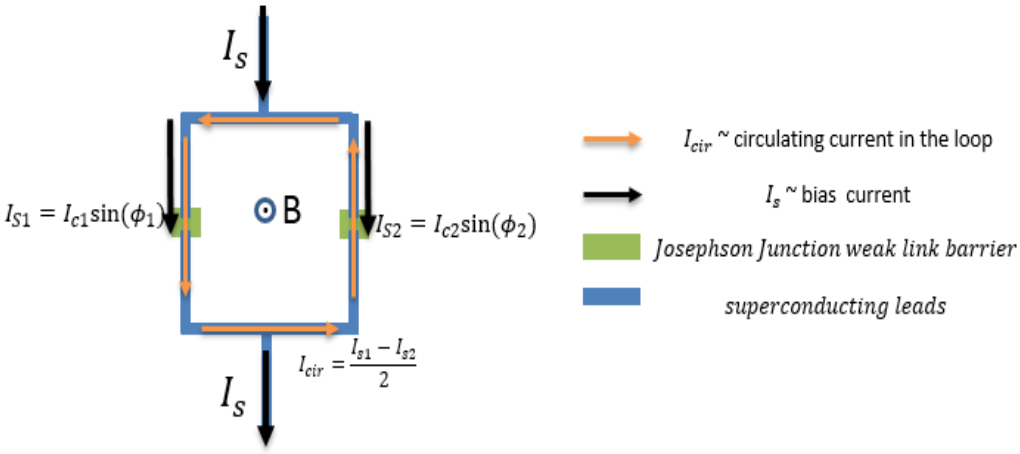

Figure 2.7: A schematic picture of a SQUID

In the ideal case, the two arms of the SQUID loop have identical critical current I_c, and the inductance of each single junction is negligible. By using the current phase relation equation, we have $I_{s1} = I_c\sin(\phi_1)$ and $I_{s2} = I_c\sin(\phi_2)$, then the total current flowing through the SQUID is

$$I_s = I_{s1} + I_{s2} = I_c\,[\sin(\phi_1) + \sin(\phi_2)] \tag{36}$$

The critical current of a SQUID is sensitive to the flux, which enables it to be used as a flux detector. This critical current can be calculated as following. Using trigonometric identities, we can rewrite the above equation into

$$I_s = 2I_c cos\ \frac{\phi_1 - \phi_2}{2}\ sin\ \frac{\phi_1 + \phi_2}{2} \tag{37}$$

Due to the flux quantization condition, the relationship between the phase difference across the two arms of the SQUID loop is $\phi_1 - \phi_2 = \frac{2\pi\Phi}{\Phi_0}$. Plugging this into the above equation, we will get

$$I_s = 2I_c cos\ \frac{\pi\Phi}{\Phi_0}\ sin\ (\phi_1 + \pi\frac{\Phi}{\Phi_0}) \tag{37}$$

Where Ic is the max value of Is. In order to maximize the total critical current flowing across the junction, the junction will adjust the value of the arbitrary phase difference ϕ_1 such that$|sin\ (\phi_1 + \pi\frac{\Phi}{\Phi_0})\ |_{max} = 1$, which is similar to the case in the single junction. For simplicity, if we consider the SQUID loop in the short junction limit where the inductance of the loop is small, the current circulating inside the SQUID loop would not contribute significantly to the phase ϕ. In this limit $\Phi = \Phi_{ext}$, and the phase ϕ is affected solely by the external magnetic field, thus the interference equation for the SQUID loop becomes

$$Max(I_s) = 2I_c \left|cos\ \pi\frac{\Phi_{ext}}{\Phi_0}\right| \tag{38}$$

Thus, the diffraction pattern behaves as pictured in the following graph:

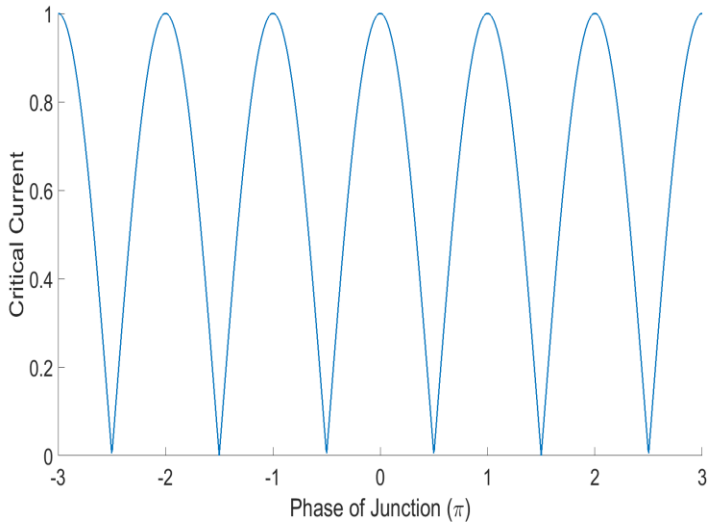

Figure 2.8: Simulated SQUID diffraction pattern with no single junction modulation envelope

In case that the single junction modulation response cannot be ignored, we would get the following form for the SQUID diffraction pattern.

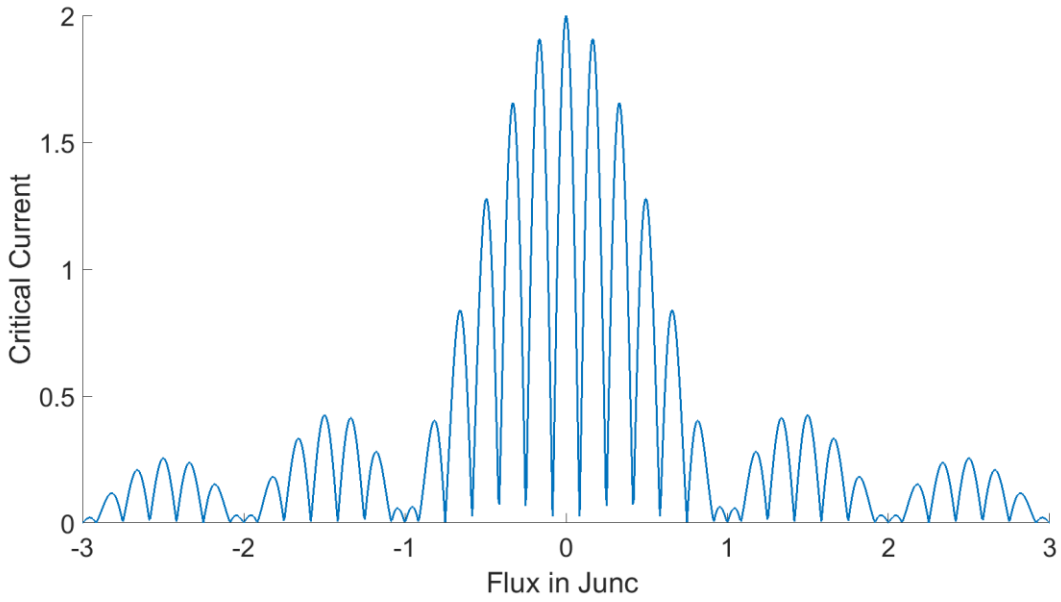

Figure 2.9: Simulated SQUID diffraction pattern with non-negligible single junction modulation

We can see here that the final diffraction pattern is composed of many fast SQUID modulations bounded by a single junction modulation envelop. This would be the case when the phase winding across the single junctions of the SQUID arm is non-negligible compared with the phase winding across the SQUID loop. In fact, this is what we have observed in our asymmetric SQUID for measuring the CPR of the TIJJ, which will be explained in detail in the asymmetric SQUID section.

In the case that the inductance of the superconducting loop is not negligible, the critical current of the SQUID loop would introduce a non-negligible flux in the loop, and we now need to take the phase due the inductance into account, such that $\Phi = \Phi_{ext} + \Phi_L$, and $\Phi_L = LI_{cir} = L\frac{I_{s1}-I_{s2}}{2}$. Plugging the current phase relation of each SQUID loop arm back into the phase equation, we get

$$\Phi = \Phi_{ext} + LI_{cir} = \Phi_{ext} + \frac{LI_c}{2}(sin\,(\phi_1) - \sin(\phi_2)) \tag{39}$$

$$\Phi = \Phi_{ext} + LI_c sin\,\frac{\pi\Phi}{\Phi_0}\,sin\,(\phi_1 + \pi\frac{\Phi}{\Phi_0}) \tag{40}$$

Both equations must be satisfied at the same time. With the constraint set by the extra phase contribution from the inductance of the loop, the critical current through the SQUID loop still must be maximized for a given Φ_{ext}. A new parameter $\beta_L = \frac{2LI_c}{\Phi_0}$ was introduced to describe how the SQUID diffraction pattern evolves as a function of inductance, as shown in the following figure by John Clarke.

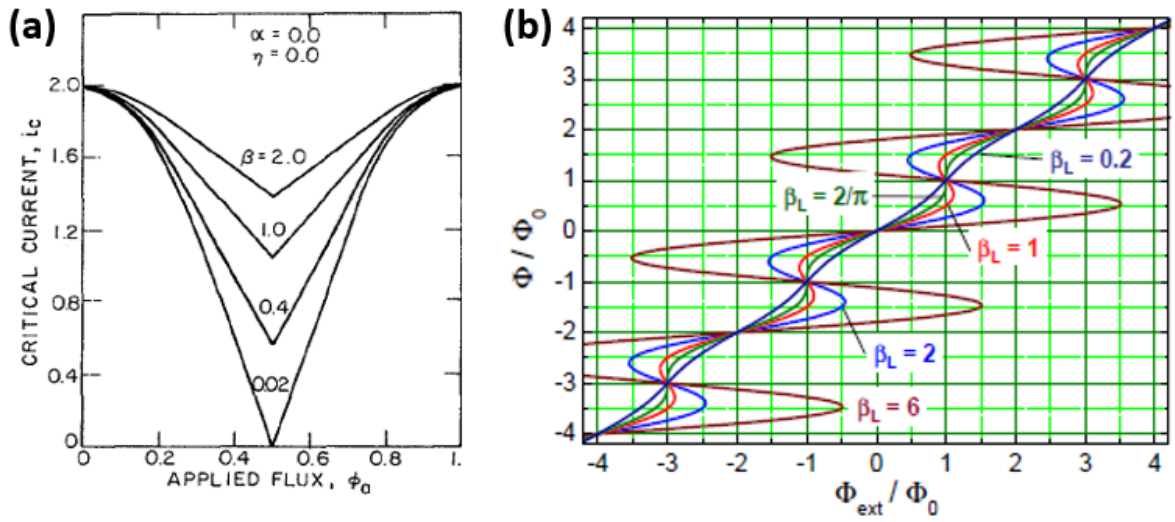

Figure 2.10: a) SQUID node-lifting effect due to large inductance in the SQUID loop. [28] b) total flux vs flux generated by external B field due to different β_L value [31]

In the low $\beta_L = \frac{2LI_c}{\Phi_0} \ll 1$ limit, the flux generated by circulating current, also known as the Meissner current, in the SQUID loop is negligible compared with Φ_{ext} , the flux contribution by the SQUID loop area and the external magnetic field. We get a simple SQUID diffraction equation $I_s = 2I_c|cos\,\pi\frac{\Phi_{ext}}{\Phi_0}|$. At every $\Phi_{ext} = \frac{\Phi_0}{2}$ half flux quantum, the total critical current of the SQUID loop is zero. This can also be understood as $\phi_1 - \phi_2 = \frac{2\pi\Phi_{ext}}{\Phi_0} = \pi$, and

$I_s = I_c[sin\,(\phi_1) + sin\,(\phi_2)] = I_c[sin\,(\phi_2 + \pi) + sin\,(\phi_2)] = 0$ at the half flux quantum point $\Phi_{ext} = \frac{\Phi_0}{2}$. However, as we change the geometry of the SQUID loop such that the inductance increases and $\beta_L = \frac{2LI_c}{\Phi_0} \gg 1$, $\Phi = \Phi_{ext} + LI_c sin\,\frac{\pi\Phi}{\Phi_0}\,sin\,(\phi_1 + \pi\frac{\Phi}{\Phi_0})$ and $\Phi = \Phi_{ext} + LI_c \simeq n\Phi_0$. Now at $\Phi_{ext} = \frac{\Phi_0}{2}$, the total supercurrent of the SQUID loop won't reach zero anymore. Instead, the SQUID nodes are lifted due to the large β_L value. For the junctions that were fabricated in this thesis, we are only concerned with the $\beta_L = \frac{2LI_c}{\Phi_0} \ll 1$, so the inductance effect is negligible.

A more general situation is that when the two arms of the SQUID loop are not contributing equal critical current, which is often referred to as the asymmetric SQUID. Adapting the idea of Goswami group from Delft University, who used the asymmetric SQUID technique to measure the CPR of an encapsulated graphene Josephson junction [32], we will use the asymmetric SQUID technique here to measure the CPR of TIJJ. The asymmetry is caused by the asymmetric contribution of critical current magnitude from the two SQUID arms $I_{c1} \gg I_{c2}$, thus

$$I_s = I_{c1} sin\,(\phi_1) + I_{c2} sin\,(\phi_2) \tag{41}$$

To accurately measure the CPR of the junction, there are two important area ratios to consider. First is the critical current ratio of the two SQUID arms, which we have discussed earlier. Second is the area ratio of SQUID vs the large single junction. This is to ensure that when we are reading out the CPR of the small junction from the diffraction pattern, the total critical current remains constant at the top of the 0^{th} peak, and does not decay too fast.

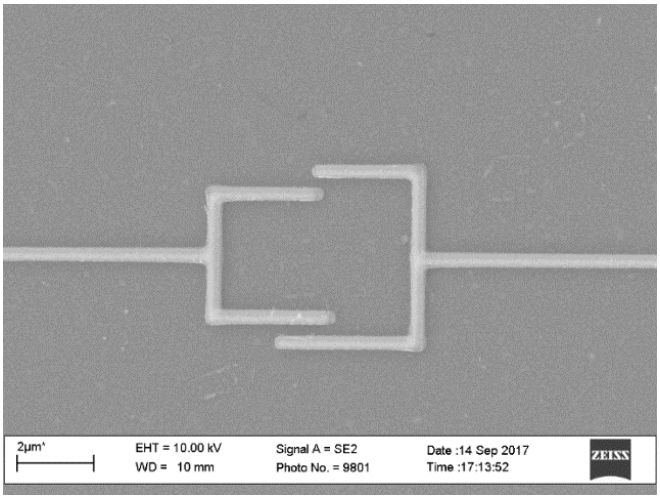

Fig. 2.11: SEM picture of an asymmetric SQUID with two arms of different length

It still must satisfy the flux quantization condition under the assumption that the total critical current is small, and the inductance effect is negligible,

$$\phi_1 - \phi_2 = \frac{2\pi\Phi_{ext}}{\Phi_0} \tag{42}$$

Now we will explain how to directly measure the CPR of the junction by employing the asymmetric SQUID technique. Supposing when the phase drop across the large junction I_{c1} close to be around $\frac{\pi}{2}$, thus we can rewrite equation 41 to be:

$$I_s(\Phi_{ext}) \approx I_{c1} * \sin\left(\frac{\pi}{2}\right) + I_{c2} sin\left(\frac{2\pi\Phi_{ext}}{\Phi_0} + \phi_2\right) \tag{43}$$

This would be corresponding to the peak of the diffraction pattern, where the critical current is at its maximum. Now the phase dependence of critical current is only a functional form of ϕ_2, and we can rewrite the above function to be:

$$I_s(\Phi_{ext}) \approx I_{c1} + I_{c2}(\Phi_{ext}, \phi_2) \tag{44}$$

From equation 44, we can easily see that when the phase of the large junction is fixed at $\frac{\pi}{2}$, where the critical current of the large junction is at its maximum. The I_c vs external magnetic field modulation is a function of the phase created by the external magnetic field and the phase of the small junction. Since the phase contribution by the external magnetic field can be easily calculated, equation 44 is then only a function of the phase of the small junction. We can get the CPR of the small junction by reading the SQUID diffraction pattern at its 1st peak, where the phase of the larger junction is fixed around $\frac{\pi}{2}$.This is an elegant, yet powerful technique to probe the CPR of the Josephson junction via direct electric transport, compared with the conventional SQUID pick-up loop technique [33,34]

We have done numerical simulations to testify the validity of the above approximation. Supposing that the CPR of a Josephson junction is unconventional and containing a pair density

wave component, which corresponds to a $\sin(2\phi)$ term in the CPR. We can express its CPR and the supercurrent of the junction in the following form:

$$CPR(\phi) = I_0 * (\sin(\phi) + \alpha * \sin(2\phi)) \tag{45}$$

$$I_s(\phi) = max\left\{\int_{-\frac{L}{2}}^{\frac{L}{2}} (J_{c1}(x) * CPR_1(\phi, 2\phi) + J_{c2}(x) * CPR_2(\phi, 2\phi)) * dx\right\} \tag{46}$$

α is used to describe the percentage of the supercurrent carried by the $\sin(2\phi)$ component, and $\phi = \frac{2\pi}{\Phi_0} B_{ext} t_{eff} x + \phi_0$, where B_{ext} is the external magnetic field, and ϕ_0 is an arbitrary phase across the junction, which will be set to maximized the total critical current across the junction in order to lower the energy of the system, J_{c1} and CPR_1 are the critical current density and CPR of either individual junction of the SQUID. We can see from the above plot that near the top of the 1st peak of critical current at zero field, other than the single junction modulation envelope, there is a fast period modulation inside the single junction envelope which corresponds to the SQUID loop modulation. The number of SQUID modulations inside the single junction envelope is equal to the area ratio of the SQUID to the single junction. In this case, we set the SQUID loop area ratio over the large single junction area ratio to be 20:1, which would create 20 SQUID oscillations within each one single junction period. We set the current asymmetric ratio to be 10:1. If we zoom in to the flat region at the top, we can see that fast modulation deviates from the conventional $\sin(\phi)$ current phase relation, which was highlighted in the red box of the Fig. 2.12 a). 3 different values of α were chosen to simulate the case of 0%, 50%, and 100% of $\sin(2\phi)$ component in the CPR. We can clearly see that for the period of $\alpha = 1$ is half of that of for the case $\alpha = 0.5$. This extra harmonic in the CPR, deviated from conventional sinusoidal CPR, corresponds to the $\sin(2\phi)$ component.

Similar numerical simulation and analysis process were also carried out for the TIJJ asymmetric SQUID, and we will discuss and compare it with the measured asymmetric SQUID CPR data in Chapter 5.

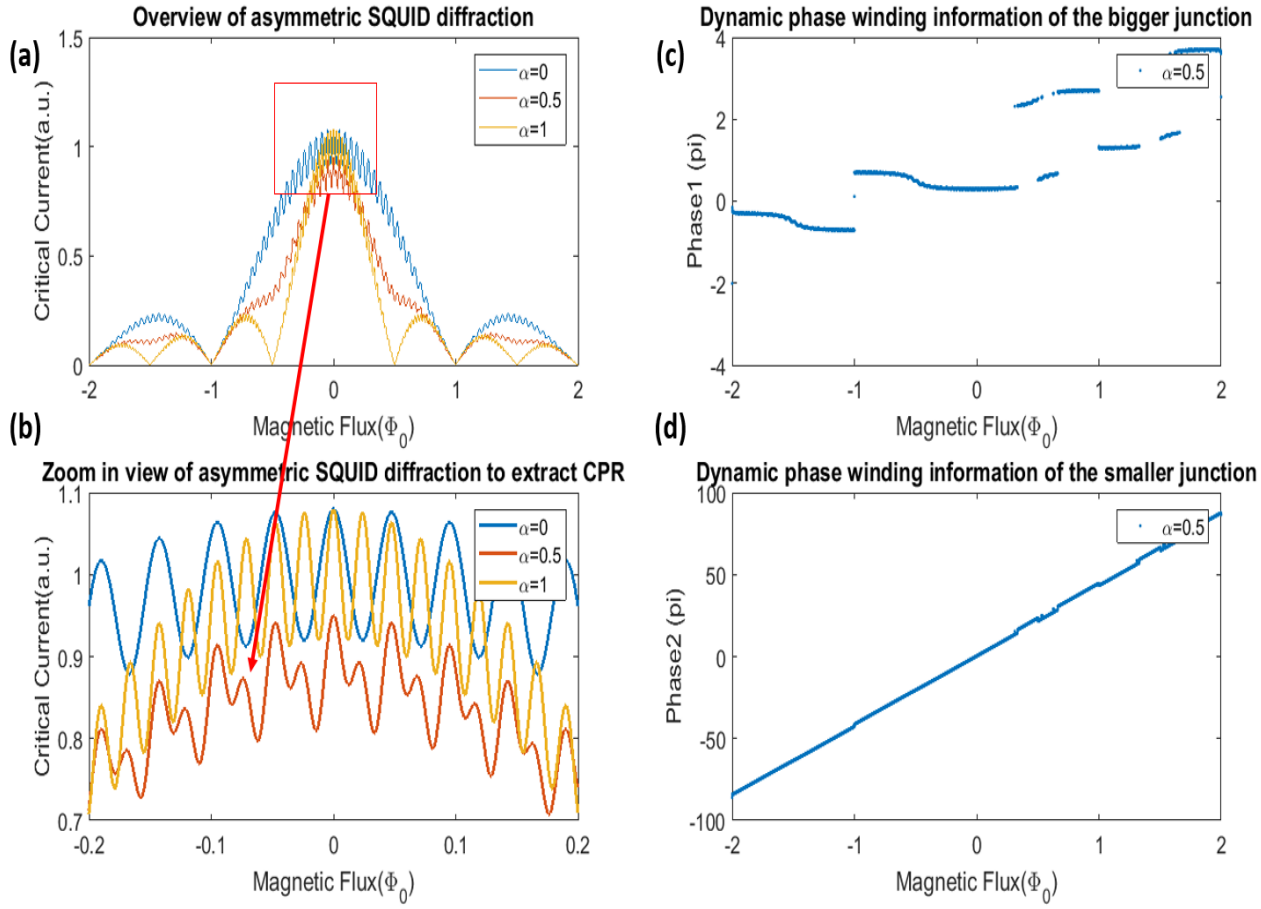

Figure 2.12: Matlab simulation of asymmetric SQUID diffraction pattern with two different percentage of $sin(2\phi)$ component in the critical current. a) Overview of SQUID diffraction pattern with single junction envelop. b) Zoom in view of the red boxed region to extract the CPR of the smaller junction at the top of the peak at zero field. c) Near zero field when the critical current of the larger junction is near maximum, the phase of the larger junction is fixed around $\frac{\pi}{2}$. d) The phase of the smaller junction in the asymmetric SQUID keeps winding as the external magnetic field is changing, and the phase of the junction now is effectively determined by the phase of the smaller junction.

2.3 Introduction to Topological Insulators

A topological insulator is a new group of quantum materials with non-trivial topological order that have an insulating bulk and a conducting surface, or a conducting edge. Tremendous effort and progress have been achieved on the topic of topological insulators in the field of condensed matter physics. This great success can be attributed to breakthroughs in the theory of topological order as well as widely accessible materials candidates, which makes the theory testable and experimental implementation feasible [35]. The most important future applications include building a fault-tolerant topological quantum computer.

The concept of topological insulators can be understood by comparing the integer quantum hall system and quantum spin hall system, which are categorized by their topological order, to the conventional Landau order parameter symmetry breaking classification standard.

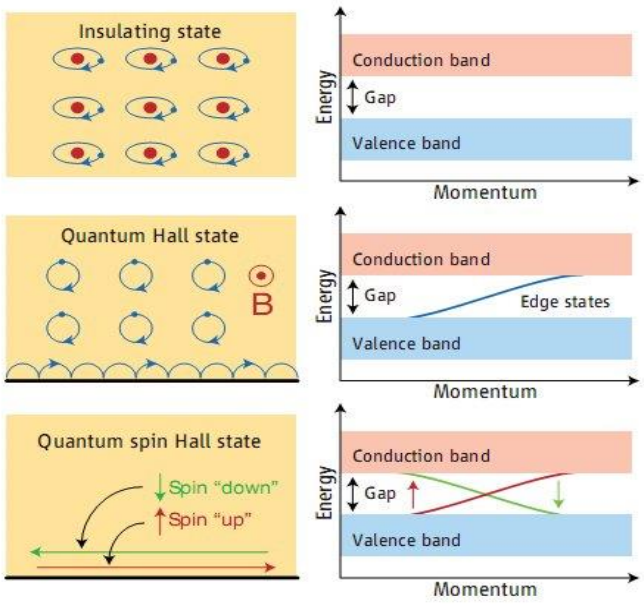

Figure 2.13: The left column shows a simple picture of different types of insulating states, with the corresponding band structure on the right column. [36]

In Figure 2.13 shown above, the top-most picture is the case for a conventional band insulator with localized electrons orbiting around the atoms, due to a wide band gap separating the valence band and conduction band. The middle pictures show a 2D quantum hall state in a strong external magnetic field, which is quite similar to the band insulator with localized electrons doing cyclotron motion around the magnetic flux lines, which are equivalent to the atoms. Thus, it has a bulk insulating gap but allows conduction of electrons along the edge of the sample. The bottom figures represent the quantum spin hall state in zero magnetic field, in which electrons can conduct along the edge of the sample boundary with spin-momentum locking, meaning that spin-up electrons only move in one direction, and spin-down electrons can only move in the opposite direction. The spin-momentum locking properties arise from the strong spin-orbit coupling interaction in the materials. A quantum spin hall insulator is a 2D topological insulator with an insulating bulk, and a conducting edge

There are many types of topological insulators, such as CdTe or HgTe with a 2D topological insulator quantum well, and the 3D topological insulators $Bi_{1-x}Sb_x$, Bi_2Se_3, Bi_2Te_3, and Sb_2Te_3. Among them, Bi_2Se_3 has the simplest Dirac cone surface structure revealed by ARPES and the largest bulk insulating gap, yet demonstrates all the key properties of topological states [7]. Thus, for all the experiments that are involved in this thesis, we will only be focusing on the 3D topological insulator Bi_2Se_3, which has an insulating bulk and conducting 2-dimensional surface states. These surface states arise from band inversion due to the strong spin-orbit coupling, as shown in the following schematic diagram.

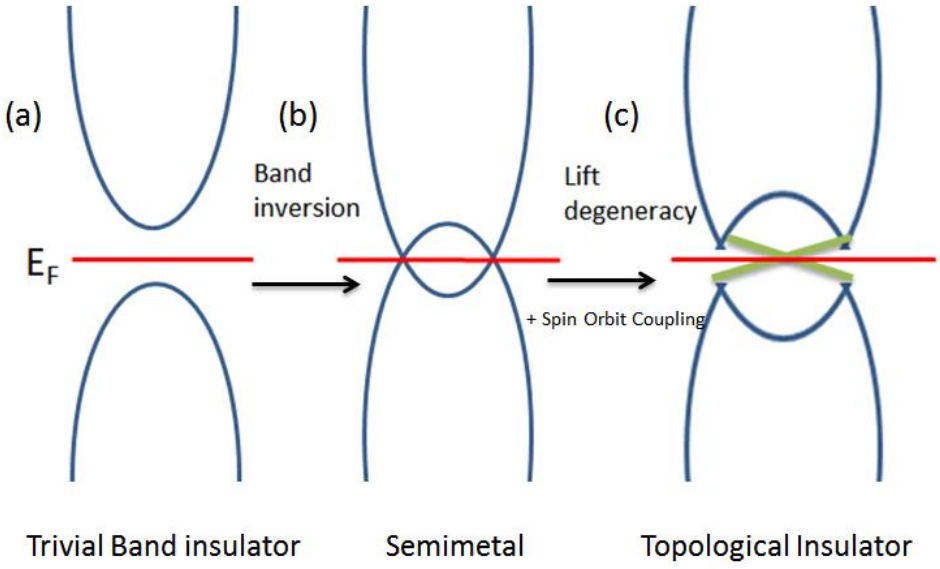

Figure 2.14: Band structure schematic of how to turn a band insulator into a topological insulator with strong spin orbit coupling interaction. a) Trivial insulator band structure. b) Band inversion process, part of the initial valence band become the new conduction band, and part of the previous conduction band become the valence band, leading to degeneracy. c) Due to the strong spin-orbit coupling, degeneracy is lifted, opening a gap.

The surface state of a topological insulator is topologically protected by particle number conversation and time reversal symmetry [36,37]. When surface states are topological protected, this means that the topological surface state is very robust and cannot easily be removed without breaking time reversal symmetry, unless it is doped with magnetic impurities [38,39,40,41]. Furthermore, due to the spin-momentum locking caused by strong spin-orbit coupling, the material strongly suppresses spin flipped backscattering, which enables applications for high speed spintronic devices [42].

Even though Bi_2Se_3 is called a 3D topological insulator, it is really a 2D layered material with a unit cell composed of 3 layers of Se and 2 layers of Bi in a repeated stacking structure. Thus, one-unit cell of Bi_2Se_3 is called a quintuple layer with a lattice constant of 1nm in c-axis direction.

In the a-b plane, it forms a hexagonal packing structure. Figure 2.15 shows a schematic crystallographic structure of Bi chalcogenides based 3D topological insulators.

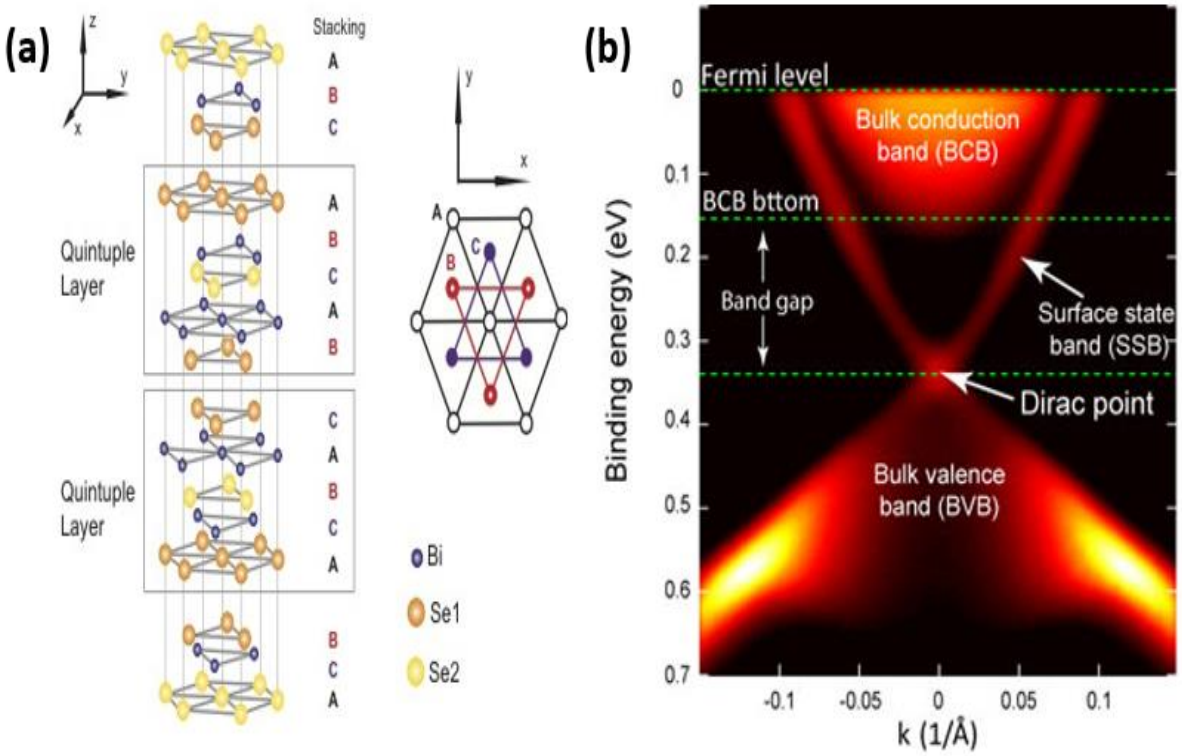

Figure 2.15: a) Schematic crystallographic structure of Bi_2Se_3[43] b) ARPES spectrum of 3D TI Bi_2Se_3[44]

Figure 2.15b shows an ARPES spectrum for the band structure of Bi_2Se_3. As we can see, that there is wide band gap separating the top conduction band and the bottom valence band, with two crossed single channels forming a Dirac cone right at the middle of the band gap. Although the concept of the edge states of a topological insulator is straightforward to understand, for most TI materials the fermi energy is not inside the band gap. Instead, it is in the bulk conduction band, which introduces non-negligible bulk contribution of charge carriers. This is mostly caused by defects, iso-valent substitution, and charge carrier doping. Field effect gating is often done to push

the fermi level back into the band gap, which eliminates bulk conduction to enhance the surface state contribution.

The details about material quality on the influence of TIJJ will be discussed again later in Chapter 4. Now we will transition to the next topic, and discuss how the Majorana fermions emerge when we put a s-wave superconductor together with a 3D TI Bi_2Se_3 to form a hybrid S-TI-S Josephson junction.

According to the ground-breaking proposal by Fu and Kane [18], one can combine a conventional s-wave superconductor and a 3D TI to form a hybrid TIJJ to simulate 2D spinless p+ip superconductivity, and one may find Majorana bound states (MBS) in the core of the Josephson vortices inside the TIJJ. The idea here is that when a non-superconducting 3D TI is sandwiched by two s-wave superconducting leads in close proximity in the lateral direction to form a 2D line junction along the x-direction, supercurrent will flow through the 3D TI across the junction along y direction. Fig 2.16 (a) shows a schematic cross-section view of such a lateral Josephson junction. When the supercurrent density is homogenous across the junction, one can solve the excitation spectrum of the proximitized superconducting 1D line junction as shown:

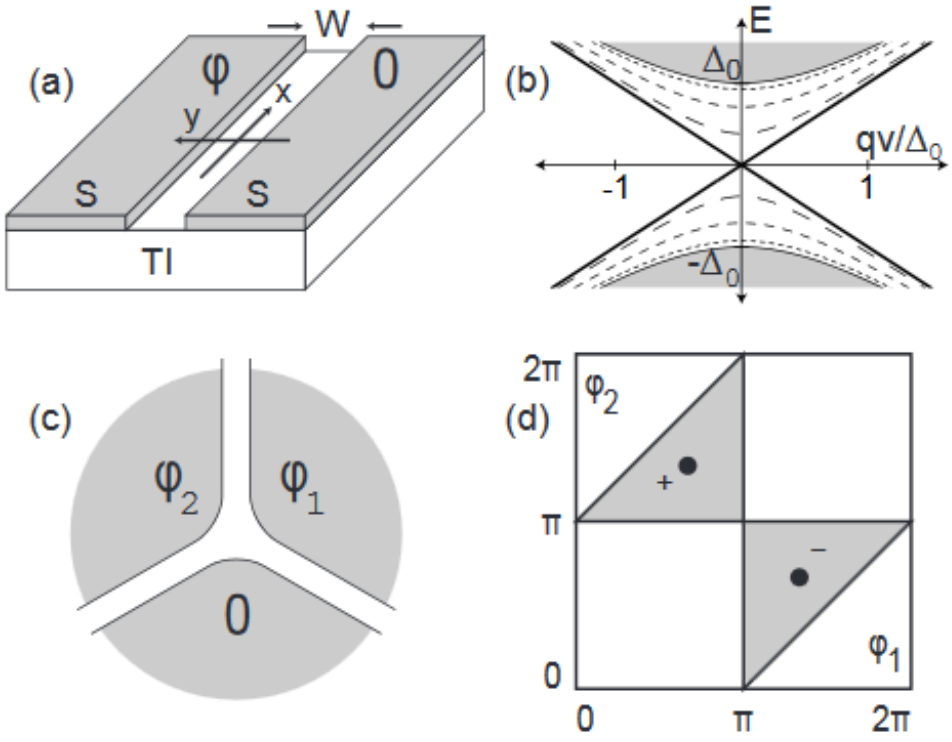

Figure 2.16: a) A schematic picture for a lateral S-TI-S Josephson junction system where S stands for s-wave superconductor, which is Nb for our system. TI stands for 3D topological insulator, which is Bi_2Se_3 in our case. b) Energy dispersion spectrum for the S-TI-S junction where $\mu = 0$. The solid line crossing the origin shows the Andreev bound states for $\phi = \pi$. c) A tri-junction between 3 superconducting hexagon islands d) Phase diagram for the tri-junction, where there is a Majorana fermion in the shaded phase space.

Considering the two pieces of superconductor are separated by a width of W with the 3D TI sandwiched in the middle, one can solve the BdG equations for the ABS in the TI surface state with $\Delta(x, y) = \Delta_0 e^{i\phi}$ for $y > \frac{W}{2}$, and Δ_0 for $y > \frac{W}{2}$, with ϕ being the order parameter phase difference across the junction. Thus, the energy excitation spectrum can be written in the following form:

$$E_q = \pm \sqrt{(\pm v|q| - \mu)^2 + \Delta_0^2 \cos^2(\frac{\phi}{2})} \tag{45}$$

Here q is the momentum in x direction, μ is the chemical potential, and Δ_0 is the order parameter for the s-wave superconductor. We can clearly see that the TI surface state is fully gapped in the energy dispersion relationship. For simplicity, we will let $\mu = 0$ lie exactly at the Dirac point. We can see that when $\phi = \pi$, which can be tuned by the external magnetic field, the spectrum is gapless. A zero-energy state emerges, which is referred to as the non-degenerate Majorana zero-energy mode. According to Fu and Kane's calculation for the BdG equations, we find the Hamiltonian for the low-energy Majorana Josephson energy to be [19]:

$$E_{eff} = -\Delta \cos\left(\frac{\phi}{2}\right)\left(n_{ij} - \frac{1}{2}\right) \tag{46}$$

In the above equation, $\phi = \phi_R - \phi_L$ is the Josephson gauge invariant phase difference across the junction, Δ is the superconducting order parameter proportional to the magnitude of the superconducting energy gap, and $n_{ij} = 0\ or\ 1$ is the number operator of the hybridized Majorana fermion pair encoding the parity states. To get the magnitude of the Majorana's contribution to the Josephson, we can simply take the derivative the Josephson energy respective to the phase:

$$I_{MF} = I_e = \frac{2e\Delta}{\hbar}\frac{\partial E}{\partial \phi} = \frac{2e\Delta}{\hbar}\frac{\partial \cos\left(\frac{\phi}{2}\right)}{\partial \phi}\left(n_{ij} - 1\right) \tag{47}$$

$$= \frac{\Delta}{\Phi_0}\sin\left(\frac{\phi}{2}\right)(n_{ij} - 1)$$

If we evaluate $n_{ij} = 0\ or\ 1$, we would find the expression for the Majorana supercurrent takes the following form:

$$I_{MF} = \pm\frac{\Delta}{\Phi_0}\sin\left(\frac{\phi}{2}\right) \tag{48}$$

The total supercurrent flowing across the junction would then be, $I_{total} = I_{2e}\sin(\phi) + I_e \sin\left(\frac{\phi}{2}\right)$. The first term, I_{2e}, is the conventional Josephson supercurrent, which is 2π periodic due to the contribution of Cooper pairs tunneling across the junction. We would mainly focus on the second term, I_e or I_{MF}, as first shown by Kitaev to be coming from the fused Majorana fermion pair $\gamma_{1,2}$ .The change of 2e to e doubles the Josephson period from 2π to 4π.

From the above discussion, we can see that this fractional or 4π periodic Josephson effect is one of the key features of Majorana fermions in topological Josephson junction systems. Looking for this $\sin\left(\frac{\phi}{2}\right)$ component in the Josephson supercurrent is quite crucial for identifying the existence of Majorana fermions. Thus, phase-sensitive Josephson interferometry is a powerful method to measure the current phase relationship of Josephson junctions, allowing observation of the $\sin\left(\frac{\phi}{2}\right)$ component and determination of the MF parity, provided that it is carried out in a dynamic way that avoids suppression from parity transitions induced by the quasi-particle poisoning effect.

The primary goal of this thesis is to test for a $\sin\left(\frac{\phi}{2}\right)$ component in the CPR of Nb-Bi_2Se_3-Nb Josephson junctions via 1) single junction diffraction pattern, and 2) direct electric transport measurement of CPR using an asymmetric Nb-Bi_2Se_3-Nb SQUID. The results and discussion will be presented in Chapter 4 and 5.

Chapter 3. Device Fabrication and Experimental Techniques.

In this chapter, I will mainly talk about the technical details regarding device fabrication, measurement setup, and data analysis. First, we will discuss nano-fabrication techniques, and then we will describe the cryogenic setup and the working principle of a dilution refrigerator. At the end of the section, I will talk about measurement electronics, circuits, and data analysis tools.

3.1 Device Fabrication

There are two primary choices of materials when considering making S-TI-S Josephson junctions. The first requires exfoliating thin flakes of Bi_2Se_3 single crystal using the scotch tape method, which is adopted from the graphene exfoliation technique. This process is time consuming, since one needs to hunt for these flakes under AFM and SEM. Another problem with exfoliating is that the thickness and size of the flakes are not controllable. After exfoliation, the flake is fixed onto a silicon-oxide buffered silicon substrate by Van der Waals force, which is weak and may allow the flakes to wash off from the substrate during processing. In short, the yield is low. For instructional purposes, I will describe how such exfoliation technique works. It is widely used in device-fabrication for 2D materials such as graphene, and transition metal di-chalcogenides, and Bi-based topological insulators.

First, Scotch tape is used to cleave the crystals into flakes, which are scrubbed onto a silicon-oxide buffered substrate. This might introduce tape residue on the surface of the exfoliate flakes, which can be cleaned off with solvents. Next, the exfoliated flakes are found and photographed under an optical microscope. After this, alignment marks are placed onto the substrate using a combination of electron beam lithography, Au metallization, and lift-off, which gives the exfoliated flakes a traceable coordinate according to their relative distance to the

alignment marks. Once alignment marks have been placed, electron beam lithography is used again to define device electrodes. Electrical connections are made to the sample through wire bonding using an Al wedge bonder. However, the wedge bonder is likely to punch through the 200nm SiO2 layer, causing shorting of the bottom gates and device electrodes.

With careful execution of each step and well-tuned processing parameters, one can achieve a high-quality S-TI-S Josephson junction. Many papers have been published on topological insulator Josephson junctions using exfoliated flakes. [48-58]

3.1.1 Thin film device fabrication

To avoid many of the failure modes mentioned above, we choose to work with epitaxial Bi_2Se_3 thin films grown on c-plane sapphire substrate. The high quality Bi_2Se_3 thin films were grown by Prof. Seongshik Oh at Rutgers University using MBE. In the next section, we will explain how our TIJJ is made with MBE grown Bi_2Se_3 thin films.

For thin film processing, we started with a 10*10mm c-plane sapphire substrate, where Bi_2Se_3 films are grown on and the typical thickness is 40nm. We started the first step by putting down alignment marks. The purpose of alignment marks is to put down some relative reference coordinates from the alignment marks to the device on the film. Next, we will go through the detailed steps of the fabrication process.

First, we clean the sample surface with acetone and IPA (isopropyl alcohol) to get rid of any contamination due to grease or dust. Then, the wafer is placed on a spinner with 2 drops of e-beam resist polymer, PMMA 950 A4 in this case, and spun at 3000 rpm for 1 minute. Then, it is placed on a hotplate at 180C for 3 minutes. We then repeat the spinning and baking process one more time, except this time we bake it for 5 minutes. The last layer we put down is a thin conducting

layer, which is called Aqua Save. This is necessary because we are processing a c-sapphire substrate, which would cause serious charging issues and prevent us from adjusting the focus of the SEM. Usually, Aqua Save is not needed if we were processing samples grown on Si substrates. The detailed steps are as follows:

1. Squirt Acetone and IPA to clean the grease and dust off the sample
2. Spin on the first layer of PMMA 950 A4 at 3000 rpm for 1 minute
3. Bake the 1st layer of PMMA for 3 minutes
4. Spin on the 2nd layer of PMMA 950 A4 at 3000 rpm for 1 minute
5. Bake the 2nd layer of PMMA for 3 minutes
6. Spin on 1 layer of Aqua Save at 3000 rpm for 1 minute
7. Bake the Aqua Save at 90C for 1 minute
8. Conduct the e-beam exposure
9. Wash off the Aqua Save layer with DI (deionized) water
10. Develop the exposed PMMA 950 A4 region with a mixed solution of MIBK and IPA at a volume ratio of MIBK:IPA=1:3
11. Evaporate 40nm of Au uniformly across the film
12. Lift off the Au by soaking it in Acetone at 65C for 1 hour
13. Inspect the pattern under an optical microscope

Step 1-13 is a complete cycle for finishing one subsection of the device fabrication process. Here is a schematic flow chart for putting down the Nb leads.

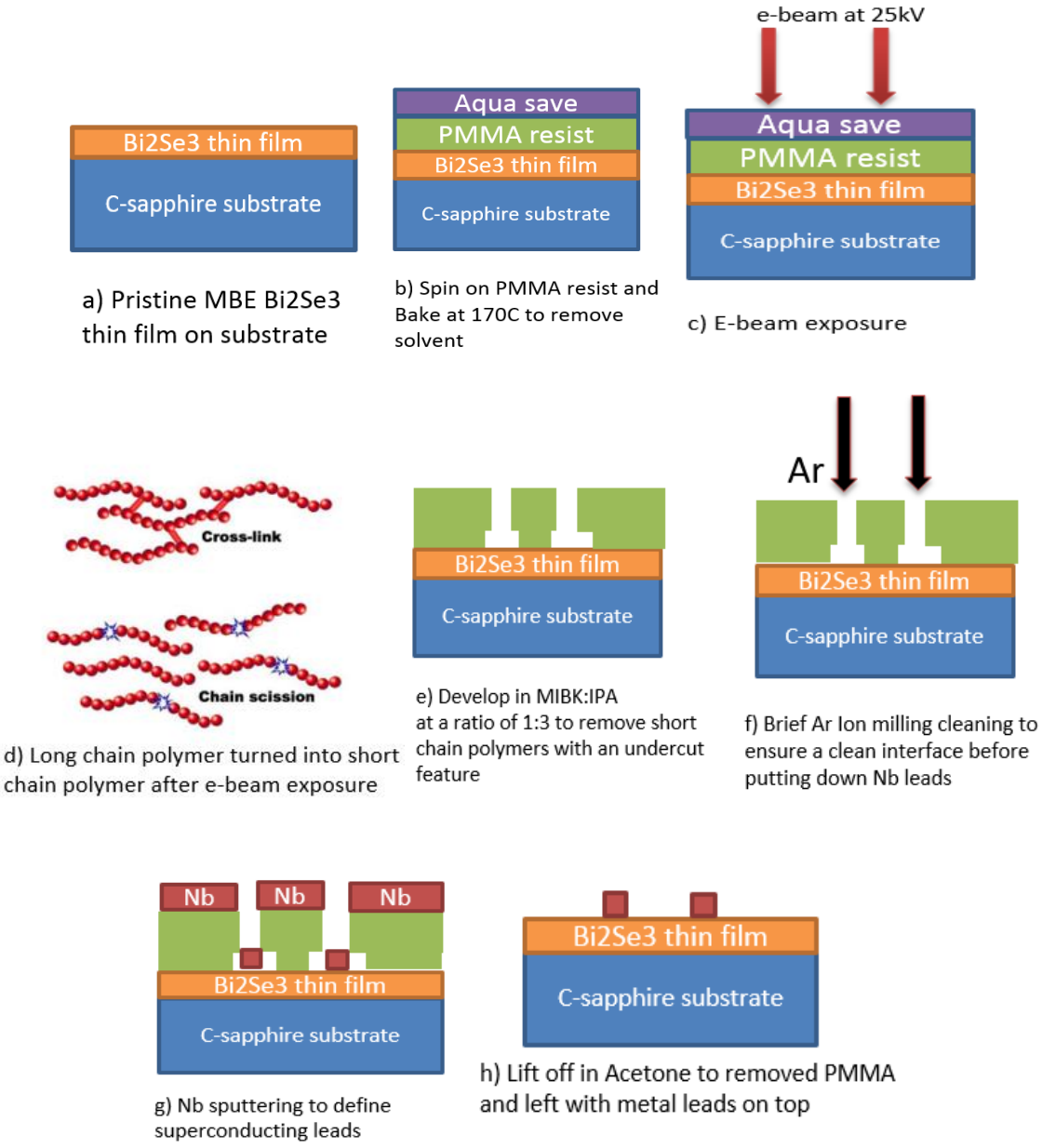

Figure 3.1: An annotated schematic flow chart showing different steps of completing one processing cycle. We then repeated this cycle to finish other major cycles.

As we can see from Fig. 3.1, we started with pristine, unprocessed Bi_2Se_3 MBE grown thin films, and spinn PMMA and Aqua save on top as a protective mask for the film. As before, we spin and bake PMMA then expose it to electron beam lithography, though before deposition we ion mill to

isolate these devices, and use magnetron sputtering of Nb for the superconducting leads. Then, the top gate electrodes are defined.

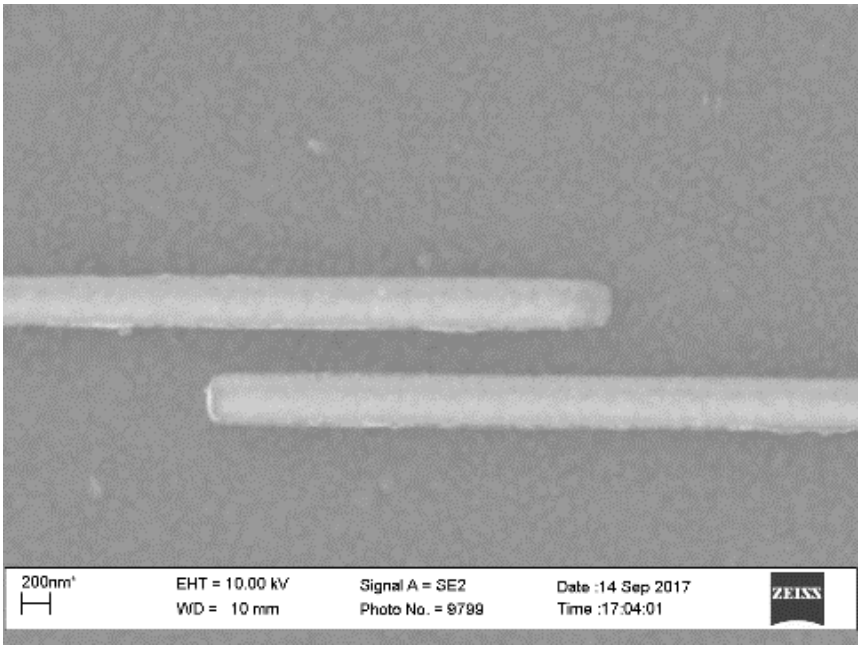

Figure 3.2: A top down view SEM picture of a Josephson junction

With careful excution of each step, Figure 3.2 shows a SEM picture of a finished Josephson junction device having 2 long, thin Nb leads to minimize junction self-screening effects. Using such nano fabrication techniques, we have made several different design of S-TI-S Josephson junctions to study exotic physics due to superconducting proximity effect. Inspired by Kane and Fu's trijunction model. we have fabricated hexagonal Nb island arrays on top of Bi_2Se_3 thin films for imaging Josephson vortices at the center of the trijunction point shown in Fig. 3.3, where MBS are located. This is an ongoing collaboration project with Tessmer group at Michigan State University.

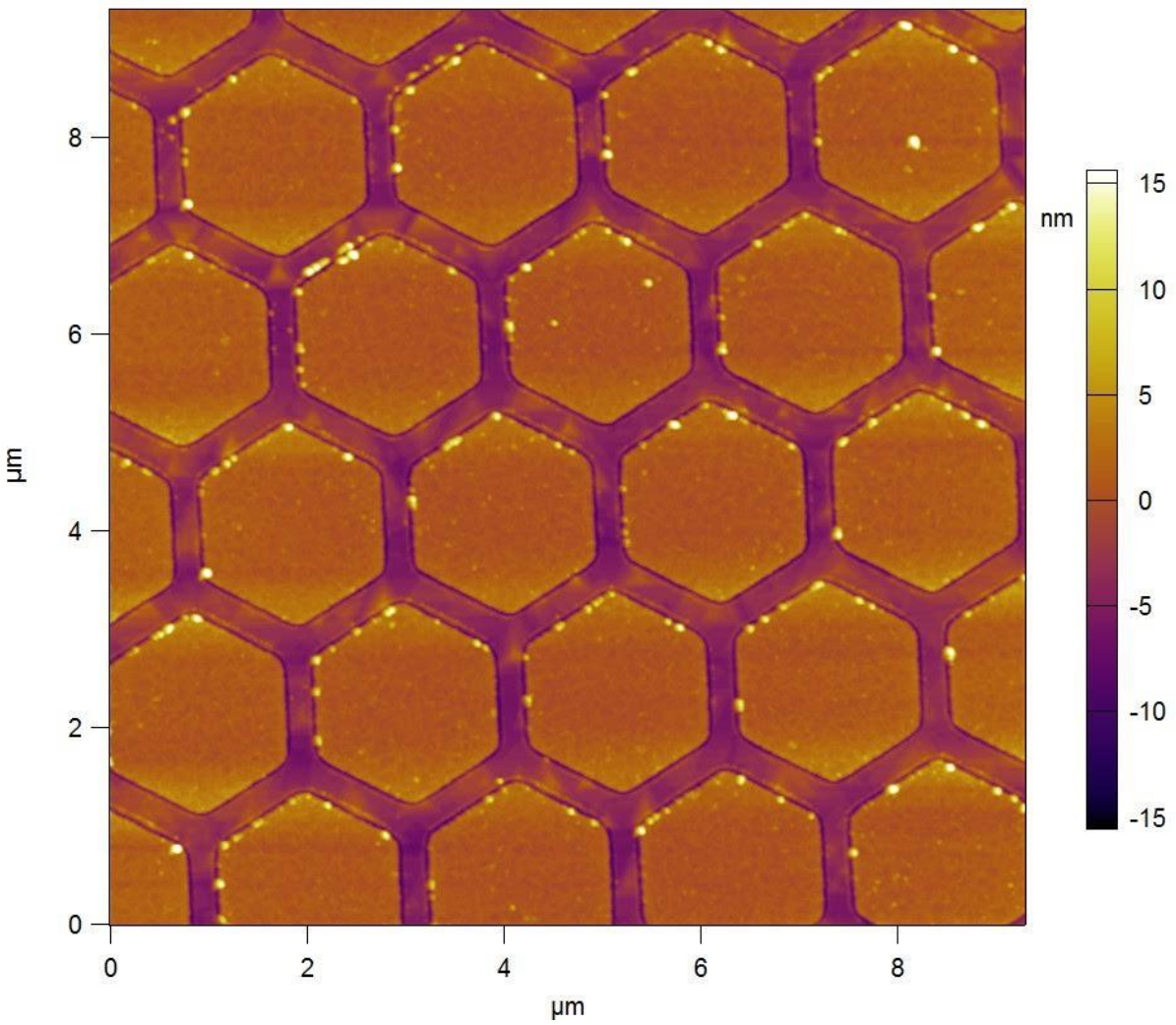

Figure 3.3: A top down view AFM image of a Nb Hexagon island arrays on top of Bi_2Se_3 for vortex imaging experiment collaboration with Tesser group from Michigan State University

3.2 Cryogenics and Measurement setup

All the S-TI-S Josephson junction data was taken using an Oxford Triton-200 Cryogen Free Dilution Refrigerator. In order to achieve supercurrent in the TI Josephson system, all measurements were conducted well below the T_c of Nb (~9K) in dilution refrigerators. Next, I will describe the working principle of a cryogen-free dilution refrigerator.

To cool the fridge from room temperature down to 20mK, the first thing we do is to pump out all the air in the OVC (outer vacuum chamber) to 3E-3 mbar with an oil free turbo-molecular pump station. After a careful leak check of the all vacuum joints, we can start cooling down the fridge. Figure 3.5 shows a schematic diagram of the circulation route for the mixture gas. This system consists of a closed circuit which connects a large tank, where the gaseous mixture of He3 and He4 is stored, to a small enclosed pot called the mixing chamber, where the mixture of He3 and He4 is condensed in mixed liquid form. This is labeled as DU (dilution unit) on the diagram.

First, a small amount of He3 and He4 mixture is drawn out of the tank and injected into the PC (precool circuit). The precool circuit is now pressurized and cools down the fridge from room temperature to 10K using a pulse tube and a compressor.

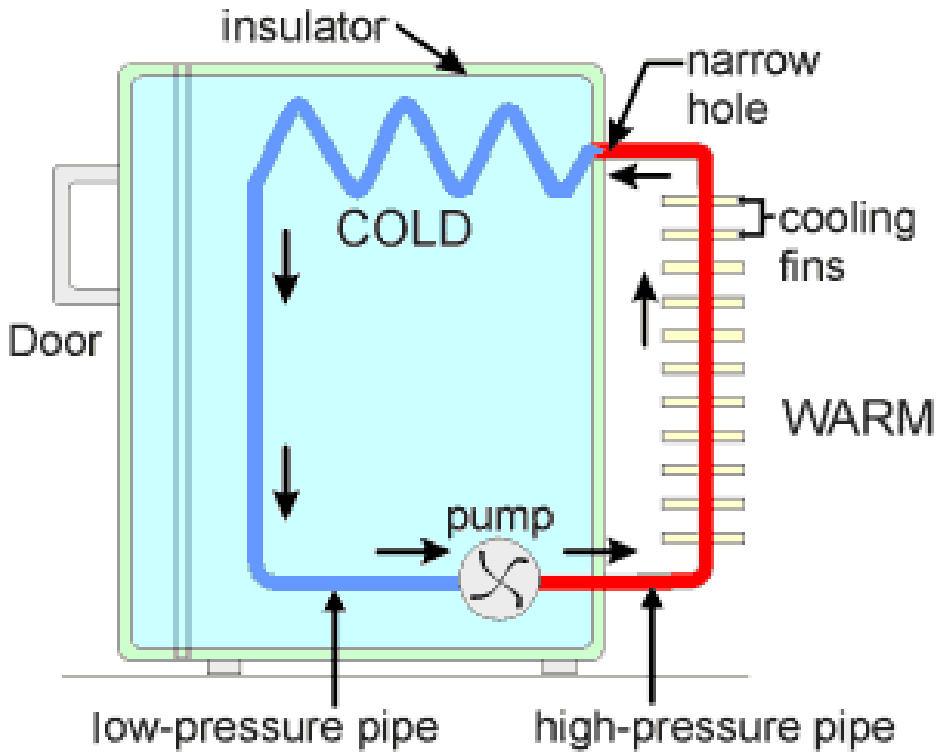

Figure 3.4: Schematic gas flow diagram for a refrigerator [45]

The working principle of this step is just like household refrigerators, where a fixed amount of gas flowing from a small diameter capillary tube to a wider diameter tube is pressurized by an external compressor. This causes a sudden drop in the gas pressure, and converts hot gas into a cooler liquid form. This liquid then flows through an absorber coil to extract heat from the metal walls, which evaporates the gas before it is fed back into the compressor, completing the cycle. This continuous closed cycle of volume expansion, condensation and evaporation is what cools down the fridge down to 10K from room temperature.

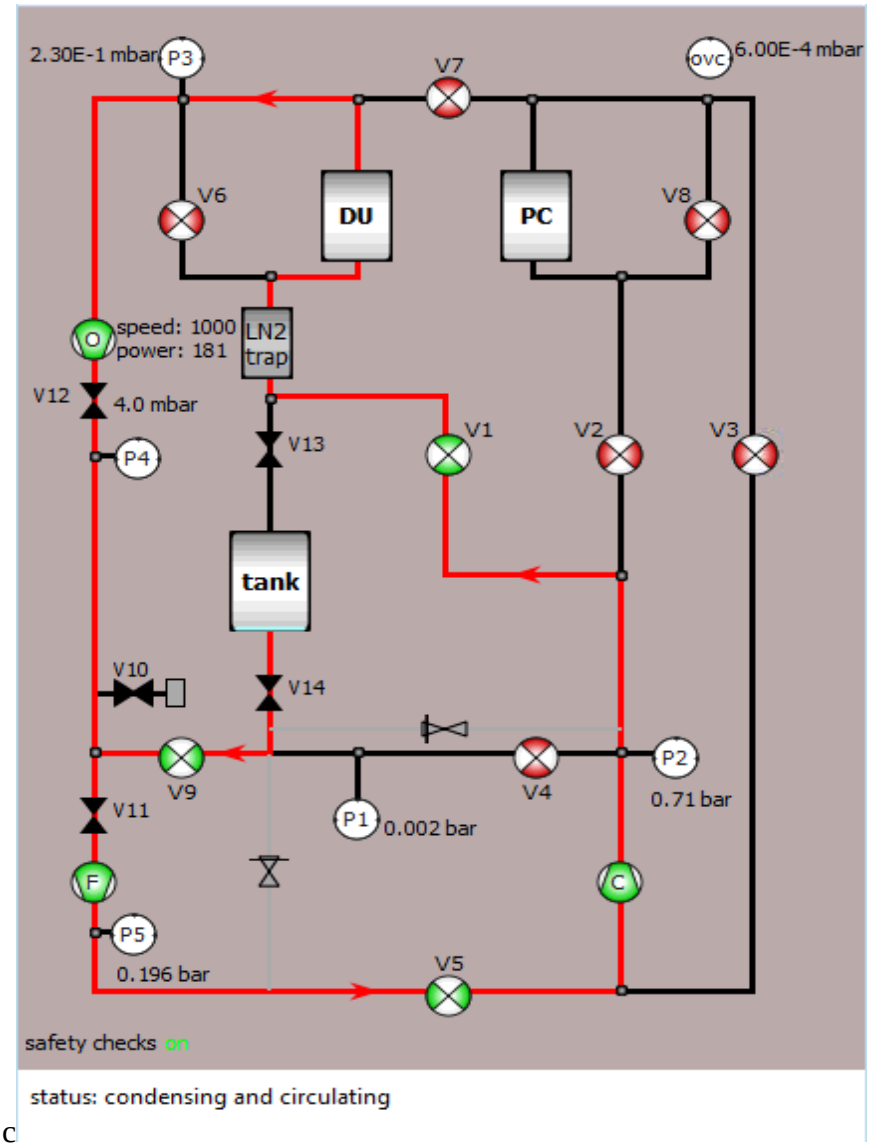

Figure 3.5: Computer screen shot of cryogen-free dilution refrigerator gas circulation diagram

In the next cooling stage, all the gas mixture in the precool circuit is collected back into the tank, and it condenses in liquid vapor form into the dilution unit (DU). This step will bring the fridge from 10K down to 20mK. This is achieved by pumping on the He3 and He4 mixture in liquid vapor from. The liquid mixture has 2 layers: a top layer composed of a He3 rich phase due to small density of He3, and a bottom layer containing mixed He3 and H4.

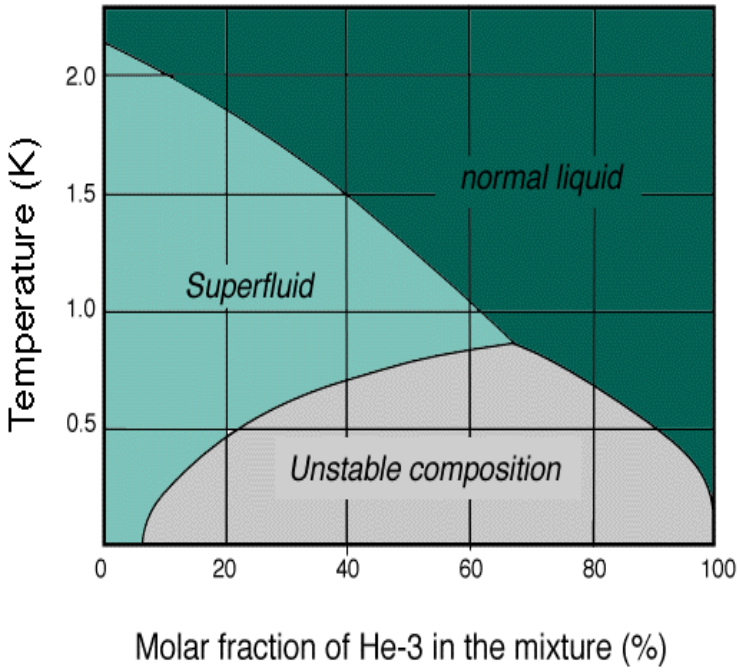

Figure 3.6: Phase diagram of He3 and He4 liquid mixture [46]

At equilibrium, 6% of He3 would be dissolved in the He4 due to the intermolecular van der Waals force between He3 and He4 atoms. Figure 3.7 shows the principle of operation behind our DR (dilution refrigerator). When we pump mixture from the He4 rich phase, mostly He3 would be removed from the mixture, reducing the He3 percentage due to its lower boiling point compared to He4. In order to remain at equilibrium, more He3 would be drawn to from the He3 rich phase to the He4 rich region due to osmosis pressure. Energy is required to make this process happen, since entropy would increase when moving He3 from He3 rich phase to the He4 rich phase. This energy is provided by the mixing chamber wall and whatever we are trying to cool down in the form of heat. Meanwhile, the evaporated He3 would be pumped back to join the He3 rich liquid vapor and replenish the lost He3 across the phase boundary. By doing this, it forms a constantly circulating flow of He3.

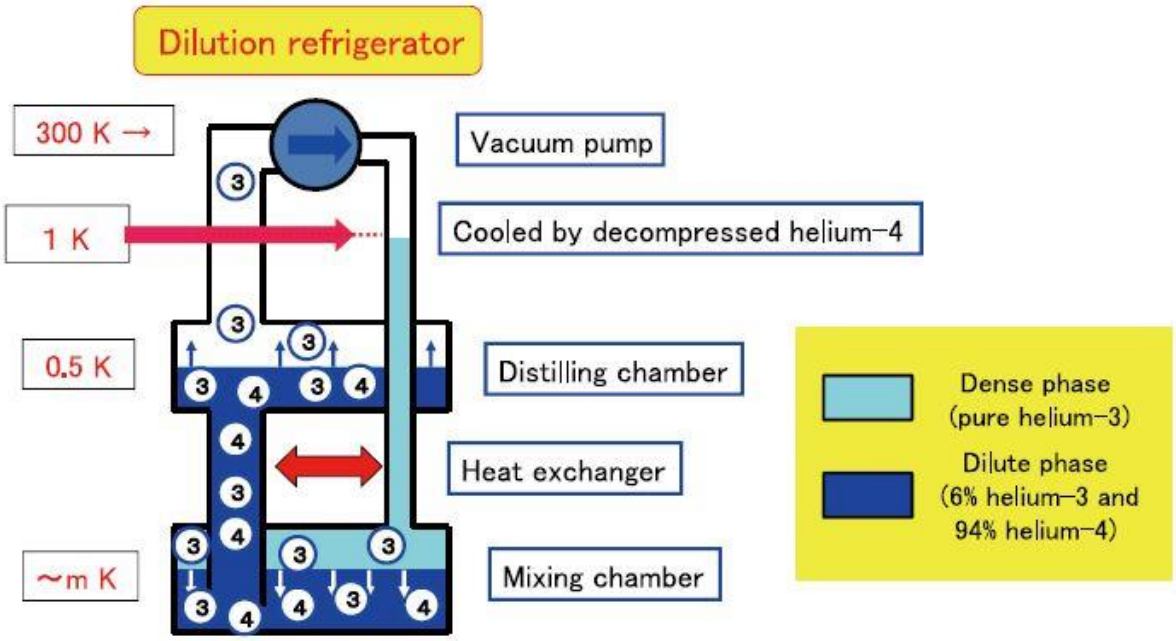

Figure 3.7: He3 and He4 mixture circulation diagram in dilution cooling stage [47]

The advantage of a cryogen free dry dilution refrigerator system is that the sample is in vacuum with no need to purchase liquid He4 to cool the system, which allows for indefinitely long hold times at base temperature (20mK).

In Figure 3.8, we will see the interior of the fridge. We can see that it is composed of stainless steel tubes and copper plates coated with gold on the surface. The gas handling and cooling of the fridge is fully automated, and our samples are mounted to custom cold fingers.

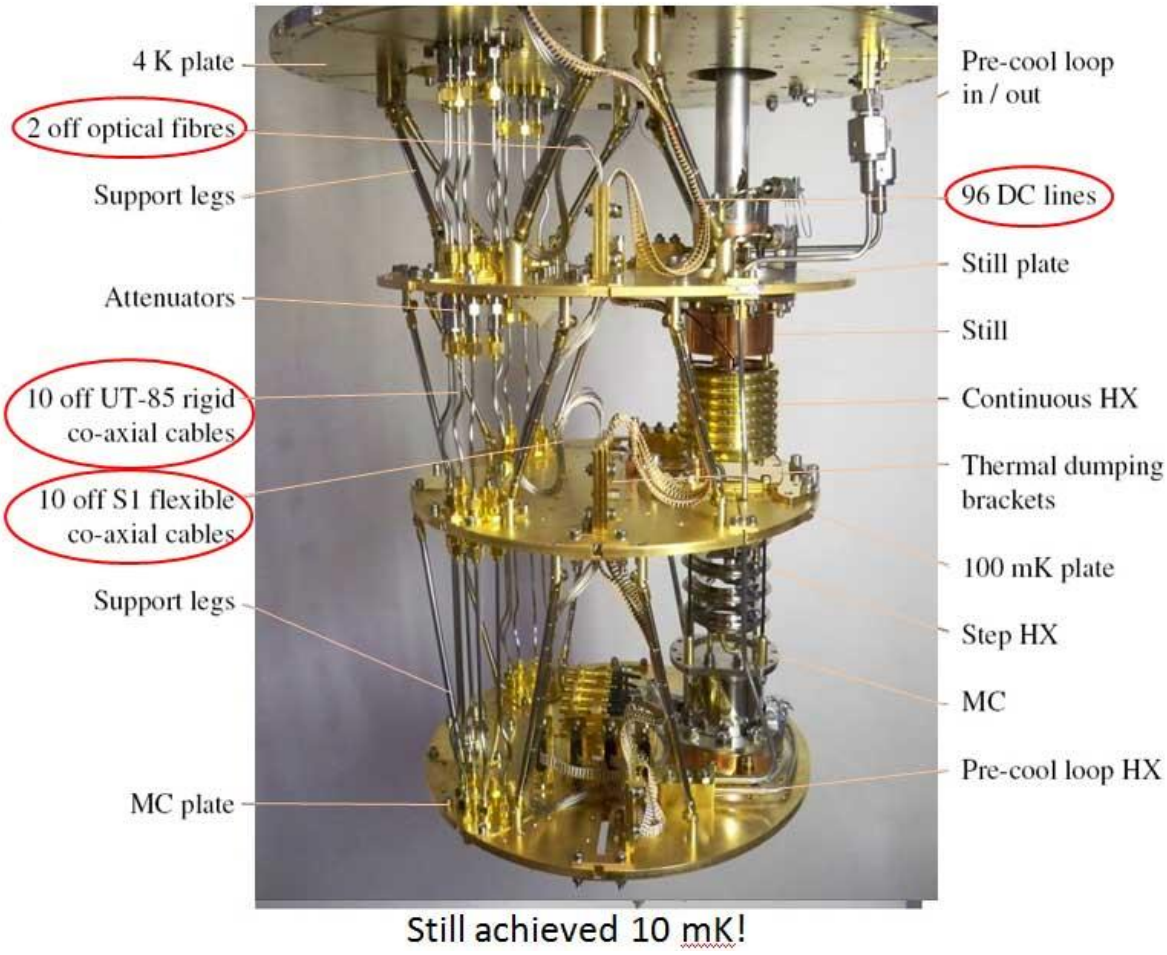

Figure 3.8: Inside look of a dilution refrigerator with different cooling stages and gas circulation pipes from Oxford website [48]

Our cryogen-free dilution refrigerator, has 4 D-sub 25 connectors, adding up to total of 96 direct-current (DC) electrical leads for conducting electrical quantum transport measurements. It has a large mixing chamber plate, which can accommodate multiple samples for each cool down. Samples are glued to 24-pin PCB chip carrier with silver paste, and the devices were wire bonded using an Al wire wedge bonder. The fridge also has co-axial cables, which enables measurement involves radio-frequency (RF) or microwave signals.

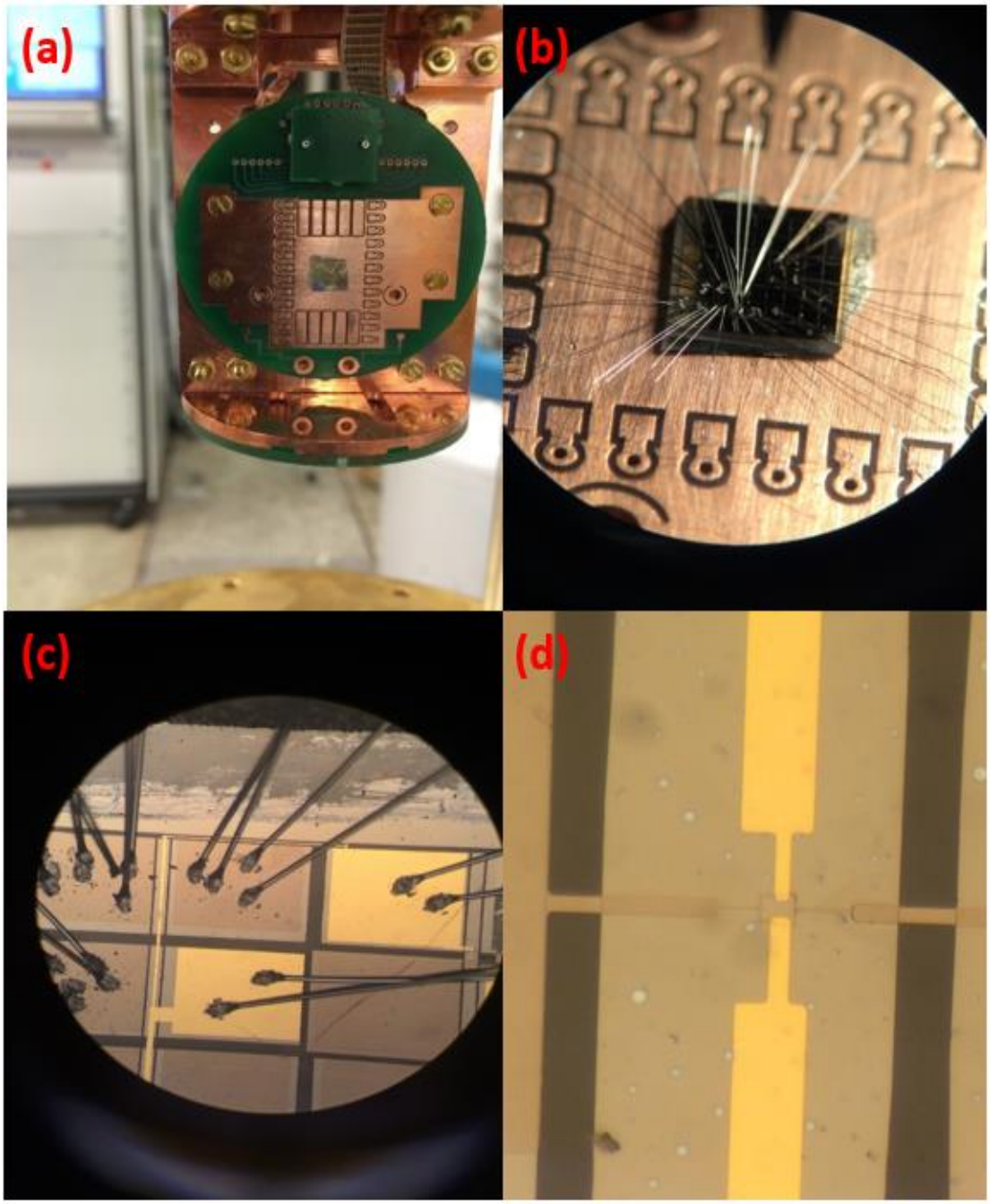

Figure 3.9: a) Custom-designed 24-pin PCB chip carrier mounted onto the cold finger of our cryogen-free dilution refrigerator, with one sample mounted vertically and another sample mounted parallel to the horizontal direction. b) Close-up of device chip glued onto the copper plate of the chip carrier with Al wire bonded onto the devices. c) Microscope image of Al wires bonded to the contact pads of an asymmetric SQUID TIJJ device d) Zoomed-in view of the asymmetric SQUID in c) with two superconducting Nb SQUID arms in the horizontal direction, and two Au leads as the top gate electrodes separated from the SQUID layer with 40nm of Al_2O_3 dielectric layer.

Because we use Nb as the contact pads, we can connect the I+, and V+ leads to the same pads, as they would not experience contact resistance when Nb is superconducting at 20mK. Thus, all the devices are equivalently measured in a 4-terminal measurement configuration. Each current or voltage lead is intentionally doubly bonded to avoid accidental broken bonds during the sample loading and cooling process. All the current and voltage leads are connected through an RC filter board, which is well thermally sunk to the cold finger to minimize electrical and thermal noise. We have two cryogen-free dilution refrigerators. One dilution fridge is nicknamed “Mr. Freeze”, and it can cool a sample from room temperature to 24mK within 24 hours.

Customized superconducting NbTi wires were wound into Helmholtz coils to generate a uniform external magnetic field. A μ-metal shield is used to enclose the sample, screening out the earth’s magnetic field and other sources of external background field noise. The other dilution fridge is nicknamed “Magneto”, which has a 3-axis vector magnet. Due to the large mass of the magnet, it takes 48 hours to reach 20mK.

3.3 Data Acquisition and Data Analysis

We used a 4-terminal measurement setup to measure I, V, dI, and dV, each individually, and then we plot IV curves or dV /dI vs V curves. A schematic circuit diagram is showing in figure 3.10 to help illustrate the setup.

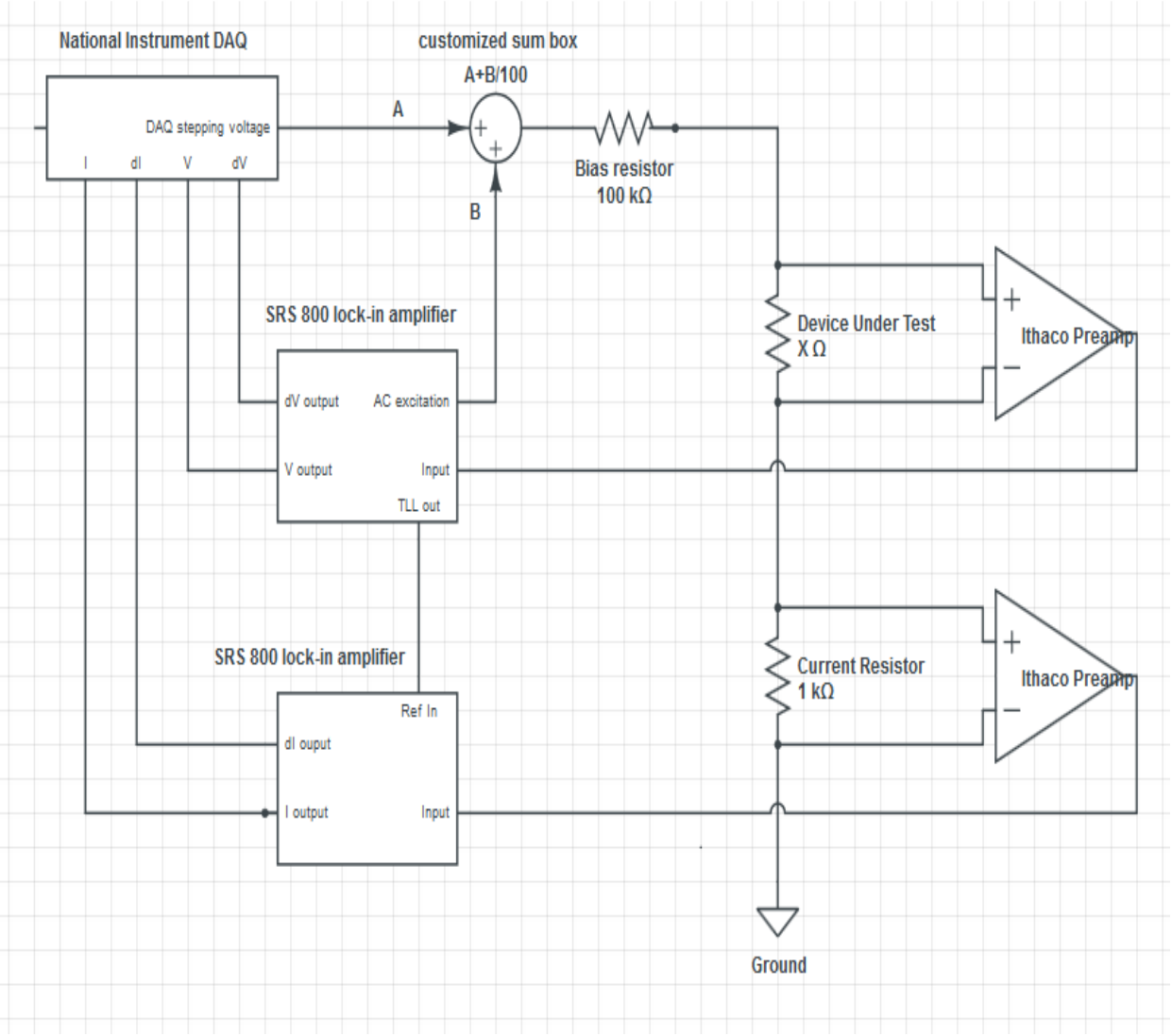

Figure 3.10: Schematic circuit diagram for measuring Nb-Bi_2Se_3-Nb Josephson Junctions. This figure shows the setup used in the measurement of single junction experiment and asymmetric SQUID CPR measurement [46].

We will now explain the measurement setup in the order from left to right, top to bottom, and then back to the top left. First, a stepping voltage and a small AC voltage excitation are added together via a A+B/100 sum box, with A being the DC stepping voltage coming from the National Instrument DAQ, and B is an AC excitation voltage supplied by the lock-in amplifier.

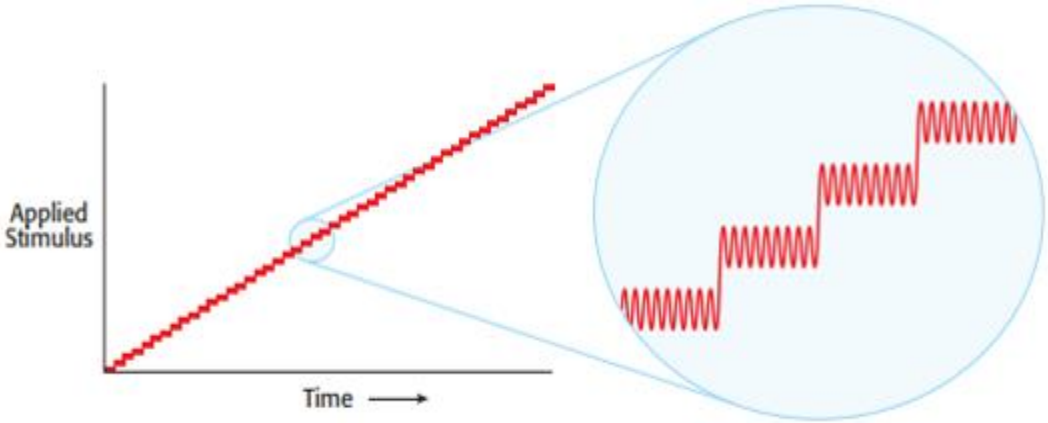

Figure 3.11: The Schematic waveform of a composite voltage input signal composed of a DC stepping voltage with a small sine wave AC excitation [47]

A 100kΩ or 1MΩ bias resistor, which will set the sweeping range of the bias current depending on the magnitude of critical current for each device, is connected in series with the circuit converting the voltage signal into current, working effectively as a current supply. Next, two Ithaco brand voltage amplifiers are used to measure the DC voltage and bias current flowing across the JJ individually. The outputs of the two preamps are connected to a BNC tee adapter on the lock-in amplifier for monitoring the dV and dI signal of the junction. The bias current is acquired indirectly by measuring the voltage across a 1k resistor, which is in series with the device and should therefore have equal current to the device. All output I, dI, V, dV come out of the lock-ins and then feed back into the DAQ. A custom-wound Helmholtz coil was used as the magnet for providing external magnetic field to Mr. Freeze, and magneto has a 3-axis vector magnet made

by Oxford Instruments. A low noise SRS voltage-controlled current source was used as the current supply to drive the magnet to the desired magnetic field. Noise filtering was done passively through the use of low-pass RC filters tuned to 1 kHz on the current input lines and through the integrated low-pass filters tuned at 300 Hz on the preamplifier stages. During the data acquisition, averaging was also used to reduce noise in the recorded signal. Measurements in this experiment were carried out using LabView routines to control the data acquisition, the output control signals and the signal averaging/data output.

All data acquisition and management, as well as output control, was done through programming in LabVIEW, using National Instrument DAQ communication libraries written by previous student in DVH lab. Plotting and further analysis of data sets was done using OriginLab and Python.

Chapter 4. Single Junction Experiment Results and Discussion

In this chapter, we report our results and analysis on transport properties of Nb-Bi_2Se_3-Nb lateral Josephson junctions. We observed even-odd node-lifting effects in many of our single TIJJ devices, which we interpret as strong evidence for a 4π-periodic $\sin\left(\frac{\phi}{2}\right)$ component in the Josephson current-phase relation (CPR). We carried out further experiments and analysis of our results to test that such even-odd node-lifting effect is solely due to the intrinsic TI proximity effect of S-TI-S lateral Josephson junction. This analysis includes the choice of high quality TI thin films, fabricating and measuring TIJJ effect of geometry, inspecting our devices under SEM, and simulating our Josephson junctions' diffraction patterns to determine the possibility of node-lifting effects originating from critical current disorder and flux focusing effects.

4.1 Introduction

A topological insulator is a new class of material that is categorized by its topological order instead of conventional Landau order parameter symmetry breaking classification standards. Among the rich materials family of topological insulators, Bi_2Se_3 is a strong 3D topological insulator with a wide bulk insulating gap and a conducting edge state, and it has received the most attention in both theoretical modeling and experimental testing. The topologically protected surface state arises from strong spin-orbit coupling, and it is protected by time-reversal-symmetry. It has attracted much research interest in the field of condensed matter physics not only due to its exotic materials properties, but also because it is a potential candidate for hosting Majorana bound states (MBS) which are expected obey non-Abelian statistics leading to possible an application in building a fault-tolerant topological quantum computer [19]. Fu and Kane had come up with the groundbreaking proposal [18] of putting two conventional s-wave

superconducting electrodes into contact with a topological insulator, forming an in-plane lateral topological insulator Josephson junction. In this system, a low-energy ABS would emerge as quasi-particle excitation states, leading to an unconventional CPR.

One of the key characteristics of MBS in a topological Josephson junction system is that the MBS enable Majorana fermions to fuse and carry supercurrent across the junction through tunneling of quasi-particle electrons [69]. This doubles the Josephson period from 2π to 4π, which is drastically different from conventional s-wave superconducting Josephson junctions where supercurrent is solely carried by Cooper pairs with charge unit of 2e. Indeed, many groups have studied the Josephson effect in TIJJ systems, and their results have implicitly hinted at the existence of a 4π periodic Josephson effect. However, few of them have discussed this 4π periodic Josephson effect in detail. Most of these previous works focused on the I-V characteristics of critical current in response to temperature [49], electric field gating [50,51], an external magnetic field [52], or using different superconductors [53,54]. Some used different forms of topological insulators, such as thin films or exfoliated flakes from a bulk single crystal, as the Josephson junction's weak link barrier [55,56,57,58,59,60]. Next, we present our results focusing on 4π periodic Josephson effect of lateral Nb-Bi_2Se_3-Nb single Josephson junctions by employing a phase-sensitive Josephson interferometry technique.

4.2 Choice of Materials

Although the theoretical concept of a topological insulator is straightforward to understand, experimentally it is challenging to have a perfect topological insulator with an insulting bulk due to material defect issues. Selenium (Se) vacancies [61] and Se, Bi anti-site defects [62] are often to blame for introducing bulk conduction channels. Figure 4.1 is a schematic picture that depicts

such defects. Se has relatively high vapor pressure, making it thermally volatile. This tends to create Se vacancies in the lattice. With Se being the anion atom in the compound, Se vacancy usually pushes the Fermi level up to the conduction band, introducing bulk conduction channels in the topological insulator. Sb was often used to compensate such n-doping effects to bring the Fermi level down towards the band gap [63].

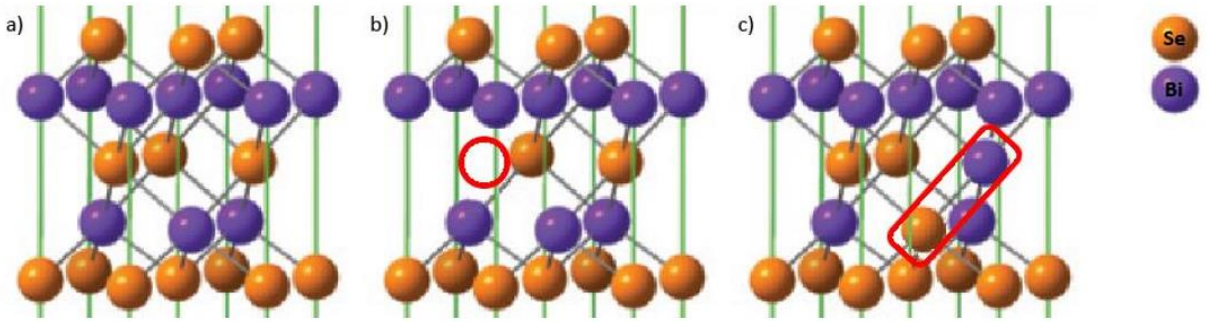

Figure 4.1: a) a defect-free stoichiometric Bi_2Se_3 unit cell b) a Bi_2Se_3 unit cell with a Se vacancy c) a Bi_2Se_3 unit cell with a Bi-Se anti-site defect. [64]

The 2nd type of defect, Bi-Se anti-site defects, were often caused by a small energy difference for switching Bi-Se positions in the lattice, due to the small electronegativity of Se [65]. Although this type of defect is charge neutral, it can still introduce bulk carriers of both signs. Isovalence substitution, or anion or cation charge carrier doping, are often done to reduce the bulk contribution. Indeed, these methods have helped bring down the bulk conduction, however it is done at the cost of degrading the surface state mobility [66,67]. Thus, the real solution to this materials quality challenge is to both reduce bulk contribution and improve surface state mobility. Low bulk carrier density and high surface state mobility are the two most important metrics to evaluate the quality of a topological insulator crystal. The most recent record for highest mobility and lowest carrier density Bi_2Se_3 thin films grown by MBE were reported by the Oh group at Rutgers with an In_2Se_3 buffered layer on top of c-plane sapphire substrates [68].

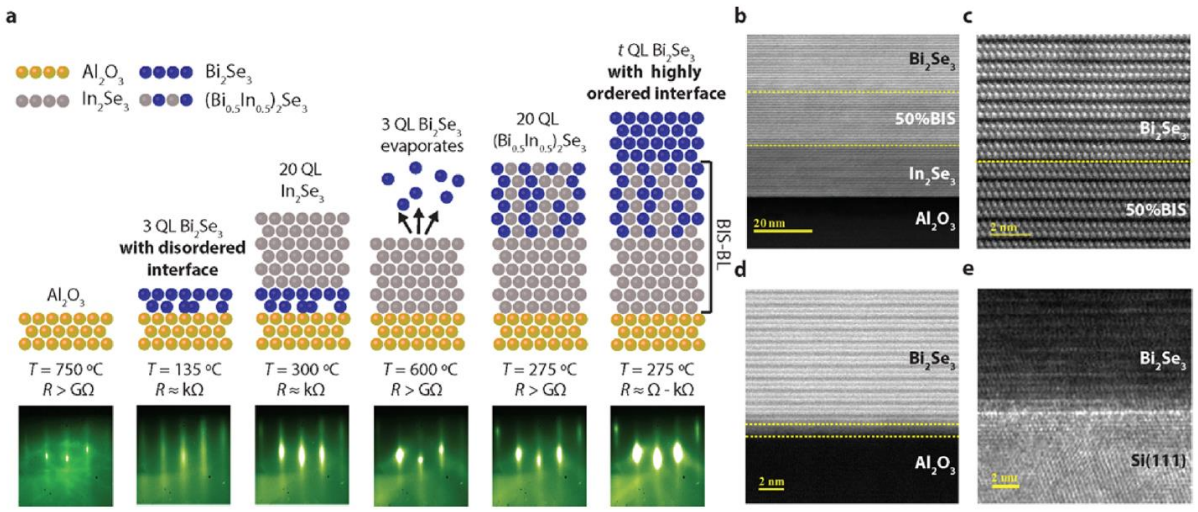

Figure 4.2: a) shows the order of the growth from substrate to buffer layer to the final Bi_2Se_3 thin films with corresponding RHEED images and sheet resistance under each stage. b), c) are the cross-sectional TEM images for the BIS-BL Bi_2Se_3 thin films with a crystalline sharp defect-free interface at the boundary. d) and e) are the cross-sectional TEM images for Bi_2Se_3 thin film grown directly on top of a c-plane sapphire substrate and a Si substrate with no buffered layer on a substrate with a blurred interface between the Bi_2Se_3 thin film and the substrate.

The idea here is that the In_2Se3-$Bi_{1-x}In_xSe_3$ buffered layer on top of c-plane sapphire acts as a well lattice-matched virtual substrate for the final growth of Bi_2Se_3, which yields a highly crystalline defect-free interface at the boundary. In contrast with the case of the Bi_2Se_3 that was directly grown on top of c-plane sapphire and silicon substrate with no buffered layer, where the interface is blurred under TEM due to disorder. These interfacial disorder defects were believed to be the reason for the bulk carrier contribution in the Bi_2Se_3 thin films. This postulate was then supported by ARPES (Angle resolved photo-emission spectroscopy) data, which maps out the energy band structure of Bi_2Se_3 respective to different growth modes. Transport measurements were also carried out to calibrate the 2D carrier density and mobility, showing consistent results.

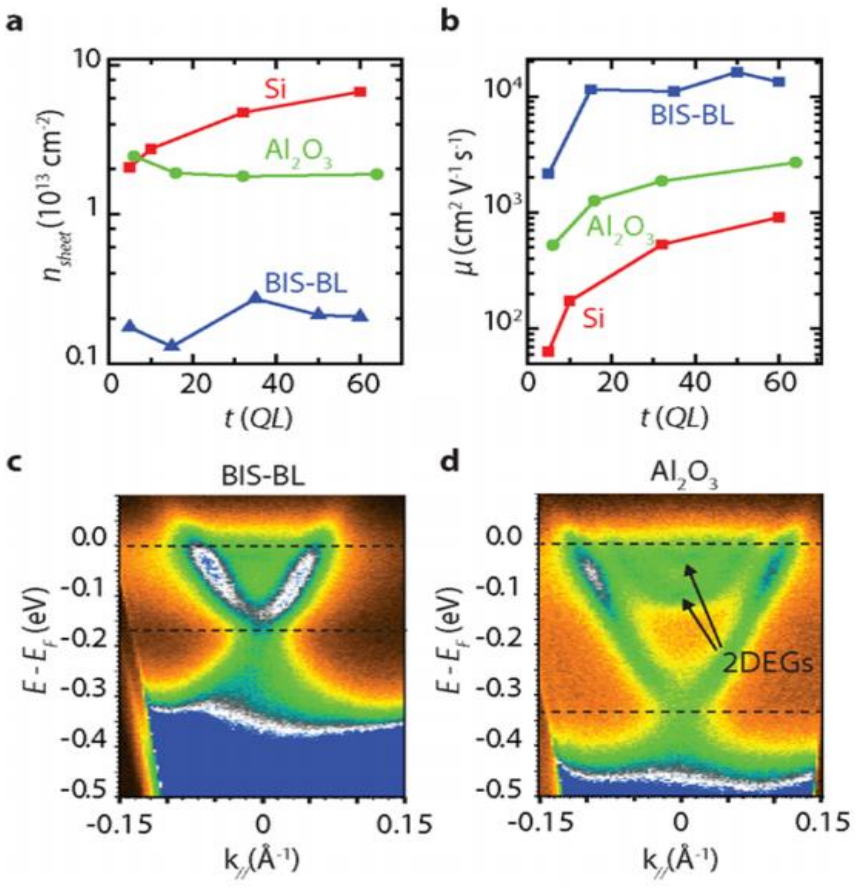

Figure 4.3: Comparison of (a) sheet carrier density and (b) Hall mobility of Bi_2Se_3 films grown on BIS-BL ($Bi_{1-x}In_xSe_3$ -Buffered Layer), Al_2O_3(0001), and Si (111) for various film thickness. ARPES of Bi_2Se_3 grown on (c) BIS-BL and (d) Al_2O_3(0001) [67]

From the above figure, we can clearly see that with a BIS-BL buffered layer, the Fermi level of Bi_2Se_3 was shifted into the gap, which significantly decreases the carrier density due to the contribution of the bulk conduction band. Furthermore, the mobility of the BIS-BL film was about 4 times higher than the non-buffered films, due to less back-scattering with bulk carrier electrons.

4.3 Device Fabrication

A series of in-plane lateral Josephson junctions were fabricated by e-beam lithography. Niobium superconducting leads were deposited by magnetron sputtering following by a 1-2 sec Ar ion-milling cleaning process to ensure a clean interface between the Nb and TI surface. All three types of TI films we were studying are around 40nm in thickness. The separation between the two superconducting leads ranges from 90nm to 400nm. The length of the leads ranges from 2um to 3um with a constant width of 300nm for the width of the leads, and all these junctions are in the small junction limit.

One typical design for Josephson junction is a head to head style with wide lead width and narrow separation. Such junction has well defined junction width and length geometry, easing device fabrication and diffraction pattern simulations. However, it is easy to run into the long junction limit once the width is too big and the critical current density is large, meaning that supercurrent screening effects would make the critical current density distribution along the junction edge complicated. Indeed, it was reported by the Goldhaber-Gordon group that such wide junction leads lead to flux-focusing effects [69]. What is more, we are likely to encounter fabrication artifacts due to local heating effects from e-beam exposure. These lead to overdose effects in the central part of the junction and an under-dose on the two-outer edges of the junction, as we can see from Figure 4.4. The junction width is 2um with a 100nm gap separation, and the junction has a curvy edge instead of a straight, parallel geometry.

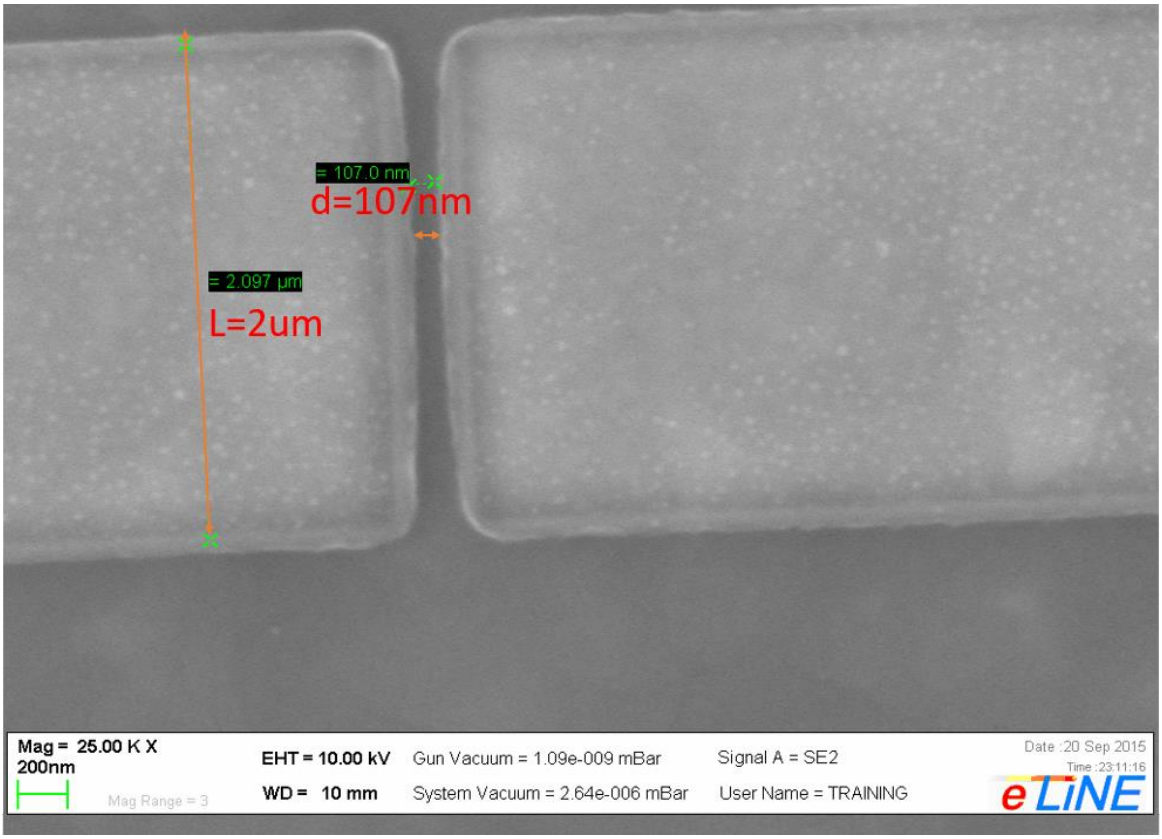

Figure 4.4: SEM picture of 2µm wide junction with 100nm gap separation showing rounded corners at the edge of the leads due to fabrication artifacts

To avoid distortion in critical current distribution along the edge of the junction due to both flux focusing effects and geometric disorder, we design our junction to be a long, thin bar type, which is shown in the following figure. The benefit of such a design is that we can have a large aspect ratio of the junction length vs junction gap separation. This would be beneficial for our future work in generating multiple vortices in the junction and creation, detection, and braiding operations involving multiple MFs in the junction without getting into the long junction regime. Another benefit we gain from this type of design is that our TIJJ has well defined, straight, parallel edges along the junction edge, as we can see from Figure 4.5, which would help create uniform the critical current density across the junction.

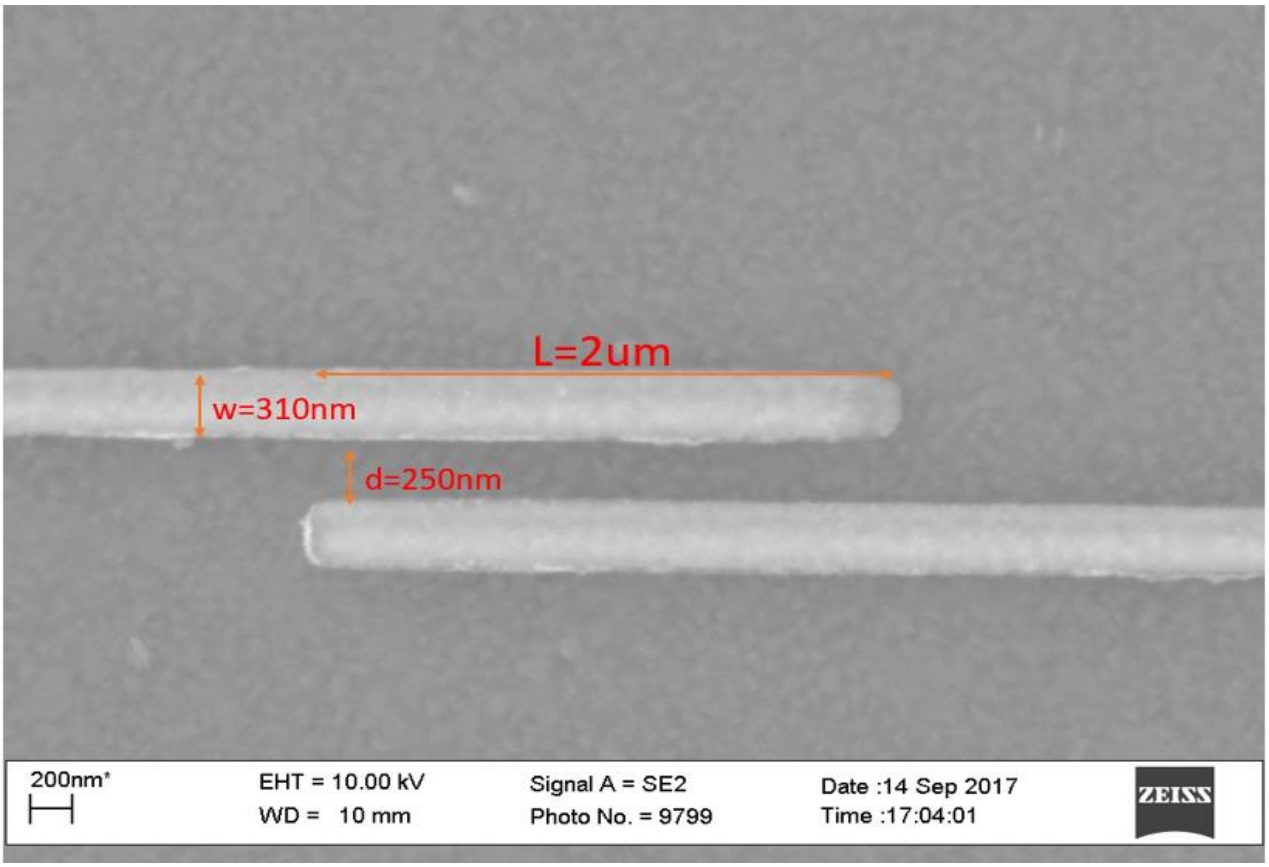

Figure 4.5: SEM picture of 2µm long junction with long thin bar design style showing well defined junction edges

4.4 Effect of Junction Geometry

In this section, we present our measured TIJJ IV characteristic and critical current vs external magnetic field data. We have made a series of junctions with the same length but different gap separations to see how the critical current decays as a function of junction lead separation, and we present the data as follows.

Gap(nm)	I_c (μA)	R_n(Ohm)	I_cR_n(μV)
130	33.14	6	198.84
180	14.65	8	117.2
230	8.38	11.5	96.37
280	5.75	14	80.5
330	3.8	16	60.8
380	2.49	20	49.8
430	0.68	22	14.96

Table 4.1 Critical current dependence of gap separation between the two Nb superconducting leads with fixed width of 3μm

Fig.4.6. shows the geometric dependence of our TIJJ characteristics. We can see that the junction normal state resistance increases linearly as a function of increasing gap separation, and it follows a linearly trace extended to zero. We also have calculated the I_cR_n product dependence on the geometry, which is usually proportional to the strength of the proximity induced superconducting energy gap.

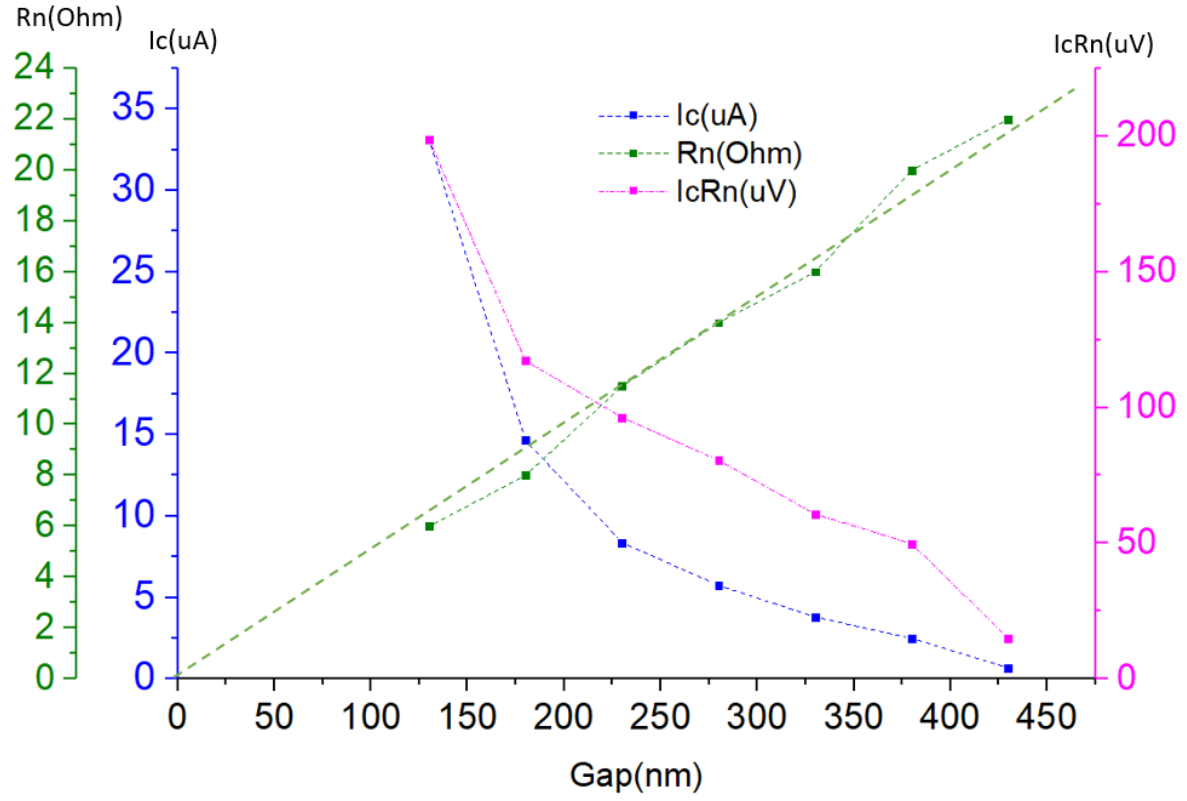

Figure 4.6: Color encoded 3-y axis plot of Nb-Bi_2Se_3-Nb later Josephson junction geometric effect study. The colored dots are the data points with dashed lines with help guide the view of the trend.

The normal metal coherence length is a characteristic length for SNS JJ, which is related to the transparency of the Josephson junction barrier. We used an exponential decay function, $I(x) = I_0 e^{-\frac{x}{\xi_N}}$ [70], to extrapolate the normal metal coherence length and Fermi velocity using $\xi_N \sim \frac{\hbar V_{NF}}{k_B T}$ [70]. As we can see from the Fig. 4.7, the critical current decays exponentially as the gap of the junction increases, and curve was automatically fitted with a two linearly combined exponential decay functions by using OriginLab. Two different values of normal metal coherence length were obtained, with one being $\xi_N^1 = 22.18 \pm 13.54\ nm$ and another one being $\xi_N^2 = 112.72 \pm 17.22\ nm$, hinting that the supercurrent was composed of two types of superfluid. This observation is consistent with previous published literature [58,59], where the critical current

decay differently as a function of temperature at different gate voltage. The story behind is that the supercurrent is carried by two different surface states in Bi_2Se_3, where one is the trivial surface state due to a 2-dimensional electron gas(2DEG) due to conduction band bending downward crossing with the chemical potential, and the other one is the topological protected surface state. Another conclusion we can draw from the above critical current vs gap separation test is that the critical current of our junction at the range of 250nm to 400nm decays very slow, this tells us that a small uncertainty in the gap separation would cause a small change in the magnitude of total supercurrent of the junction, indicating that critical current disorder effect is negligible at this distance regime.

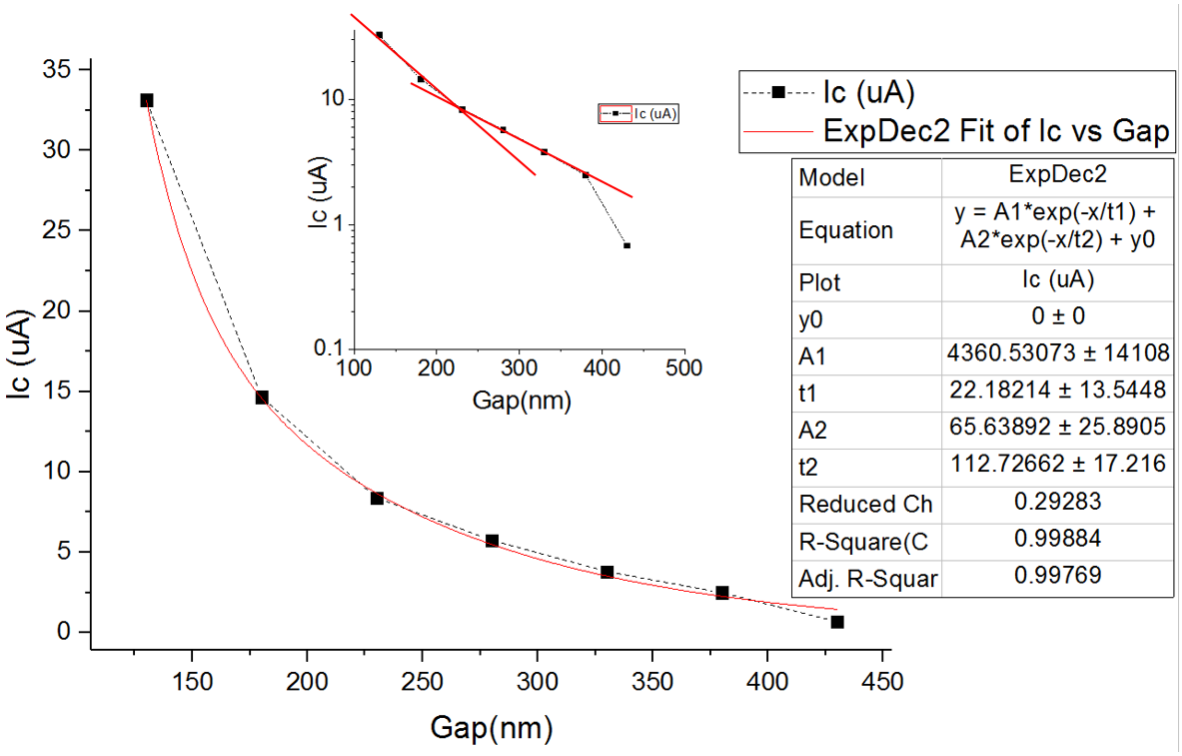

Figure 4.7: Critical current dependence of gap separation curve fitted with an exponential decay function in red trace, with the semi-log plot inset on the top center

So far, we have discussed the important role of Bi_2Se_3 materials quality in detail, and we used high quality Bi_2Se_3 films to ensure that all our transport results are dominated by the surface state contribution. From the SEM pictures in Fig. 4.3, and Fig. 4.4, we can see that our long and thin bar type junction has well defined junction edge, indicating there is a minimal amount of geometric disorder in our junctions. The amount of uncertainty in the edge is around +/-2nm, which is negligible compared to our typical Josephson junction gap separation distance, 250nm. In the next section, we will analyze our single junction critical current vs magnetic field modulation data, and we extract a magnetic penetration length of 85nm. This indicates that all our junctions are within the short junction limit, which means flux focusing effect is negligible and the critical current density is uniform along the edge of the junction. From now on, we can assume that all the junction diffraction physics we are studying are due to the intrinsic superconducting proximity effect in the topological insulator, instead of flux focusing effects or disorder in critical current density.

4.5 Single Junction Results and Analysis

Next, we will look at the single TIJJ diffraction data. The I-V characteristic of one of our Nb-Bi_2Se_3-Nb JJs are shown in the Fig. 4.8 at different sample temperature. The value of critical current (I_c) was defined as when there is a finite voltage drop across the junction with a switch in the I-V curve. The I_c vs temperature dependence was extrapolated according to this definition.

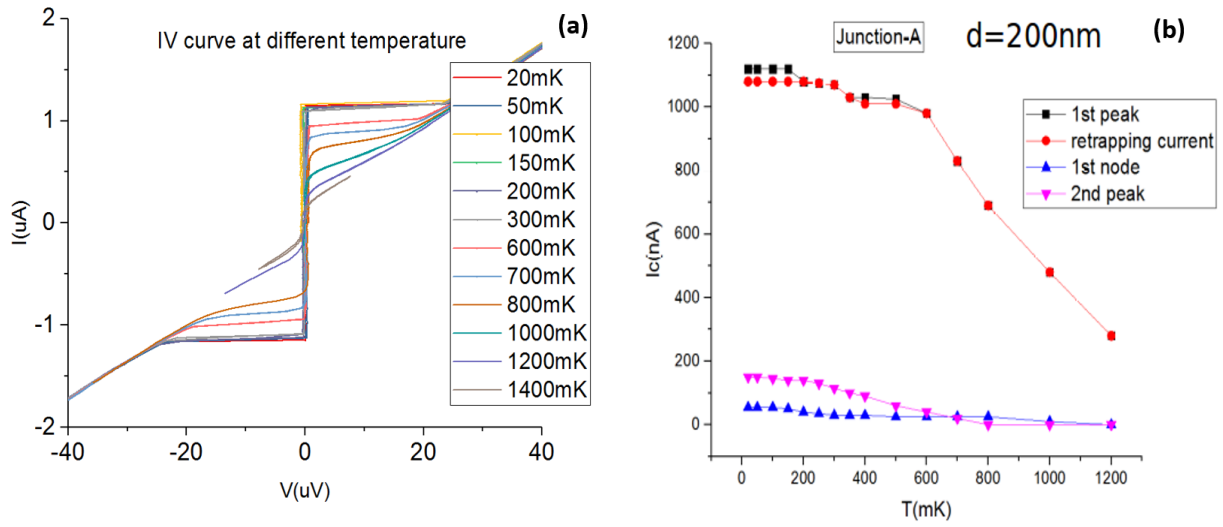

Figure 4.8: a) left figure shows the IV characteristic for one of our TIJJ at different temperatures b) critical current vs temperature plot where critical current was extrapolated from IV curve.

The single junction critical current vs magnetic field diffraction pattern is shown in Fig. 4.8. In Fig 4.8 a), the black curve is our actual measured diffraction data, and red curve in Fig 4.8 b) is our simulated diffraction pattern with only the conventional $\sin(\phi)$ component. As highlighted in the red square box of Fig. 4.8 a), there are three main striking features in our measured data. First, we noticed is that our single TIJJ is 4π periodic, with the 1st node and 3rd node lifted, and 2nd node and 4th nodes pinned down to zero. Such even-odd node lifting effect is also symmetric about the y-axis in the negative field direction. To our knowledge, similar node-lifting effect was shown or implicitly hinted in previous published literature [58,59], but many of them explained this effect with disorder [48], flux focusing effect [69] or simply ignored, and none of them showed such consistent even-odd effect symmetric about the peak to the 4th nodes.

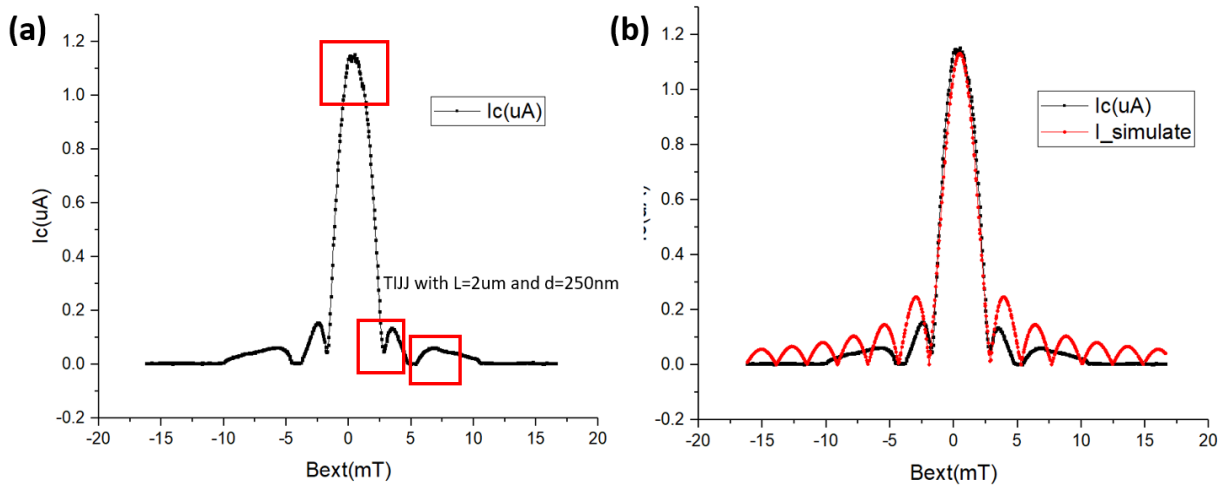

Figure 4.9: a) measured TIJJ diffraction with entry feature and even-odd node-lifting feature. b) Simulated Fraunhofer diffraction pattern for conventional JJ with all nodes pin down to zero.

From the measured Josephson period in magnetic field, we also calculated the effective area of the Josephson junction, and we found out that out junction has a magnetic penetration length of $\lambda = 85nm$ indicating that we are well within the short junction limit, where flux focusing effect can be ignored. This is calculated by using $\Phi_0 = B_{ext} * A$, where Φ_0 is one flux quantum and B_{ext} is the applied magnetic field, and $A = L * (d + 2\lambda)$ is the effective junction area. The correspondence of each of the dimension is depicted in Fig. 4.7 a). If we are in the long junction limit as shown in Fig. 4.7 b), the superconducting leads have such a large critical current density that it generates a self-screening field to push all the external field into the gap of the junction, making the effective junction area smaller, and this would make the critical current density distribution along the edge of the junction leads complicated leading to irregular critical current vs magnetic field modulation patterns.

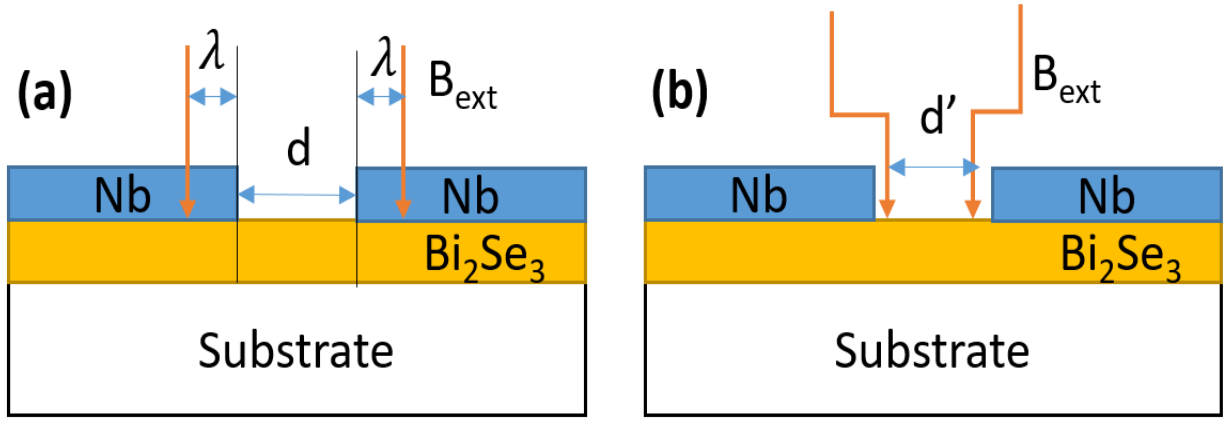

Figure 4.10: a) Superconducting JJ in the short junction limit with external field penetrating into the superconducting leads b) Superconducting JJ in the long junction limit where the supercurrent density is so big that all the external magnetic field are screened in the superconducting leads and squeezed into a narrow junction between the leads.

Secondly, other than the even-odd node lifting effect, we also noticed there is a small glitch feature on the shoulder of the diffraction pattern as highlighted in the top red box of Fig. 4.8 a). To ensure this abrupt vortex entry feature was not a measurement artifact, we took trace and retrace of the single TIJJ diffraction pattern starting from zero and going to the positive maximum, and then reversing the field direction from positive maximum all the way to the negative maximum, and then reversing the field ramping direction again from negative maximum back to the starting point at zero field. The diffraction pattern was shifted slightly in the horizontal direction to help observe this vortex entry feature. This can be explained by employing the model of MBS localized at the core of the Josephson vortex, and the Josephson vortex can enter and leave the junction seamlessly as the phase is winded by the external magnetic field, which is supported by reproducible feature at the same location in the trace and retrace plot in Fig. 4.10. We can see from figure 4.1.11 that all the characteristic features are reproducible and showed up at the same

position. reproducibility of each key feature on the diffraction curve including the even-odd node-lifting effect.

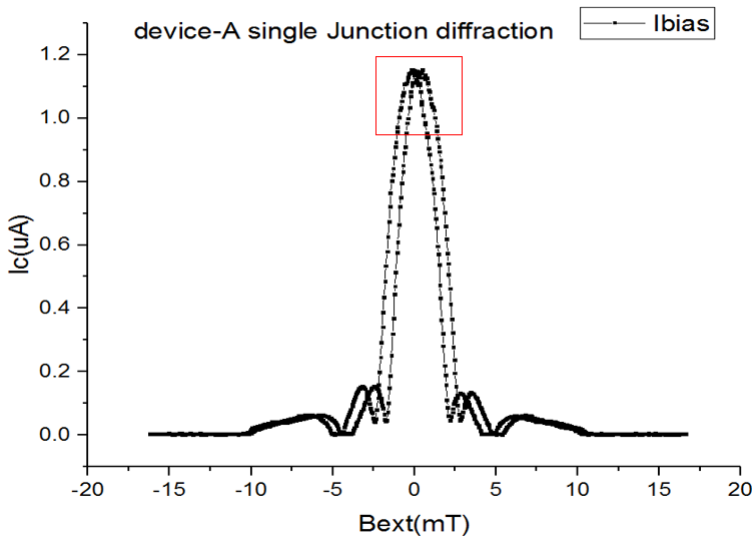

Figure 4.11: Trace and retrace of diffraction pattern for one of our TIJJ

Now, we will attempt to explain how the origin of these characteristic features leads to 4π periodic Josephson effect in our TIJJ diffraction pattern. It is well-known that disorder in the critical current distribution causes incomplete cancellation of supercurrent, and can lead to lifting of the nodes and deviation from an ideal Fraunhofer diffraction pattern. Although it is hard to rule out this effect, we do not think this is the origin for the lifting of nodes in our junctions for the reason listed here:

(1) These features are consistent for many of our single TIJJ samples, ruling out anomalous device-specific origins. The feature of node-lifting is so robust that we saw it in many different forms of Bi_2Se_3 samples, including MBE thin films grown both with and without In_2Se_3 buffered layers as well as exfoliated flakes from Bi_2Se_3 bulk crystals.

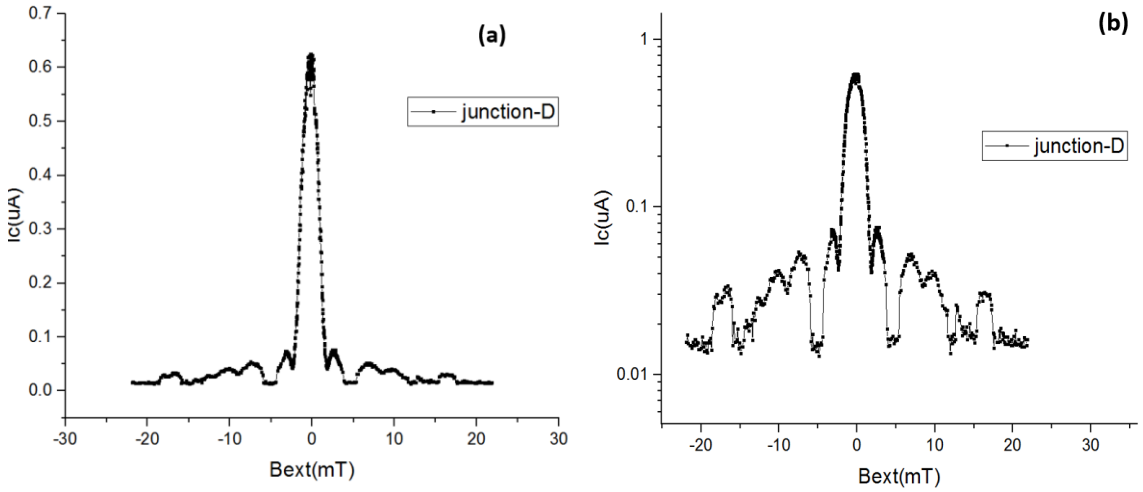

Figure 4.12: a) left shows another TIJJ with BIS buffer layer showing in linear scale b) semi-log scale plot of the same device to show the even-odd node-lifting effect in the diffraction pattern.

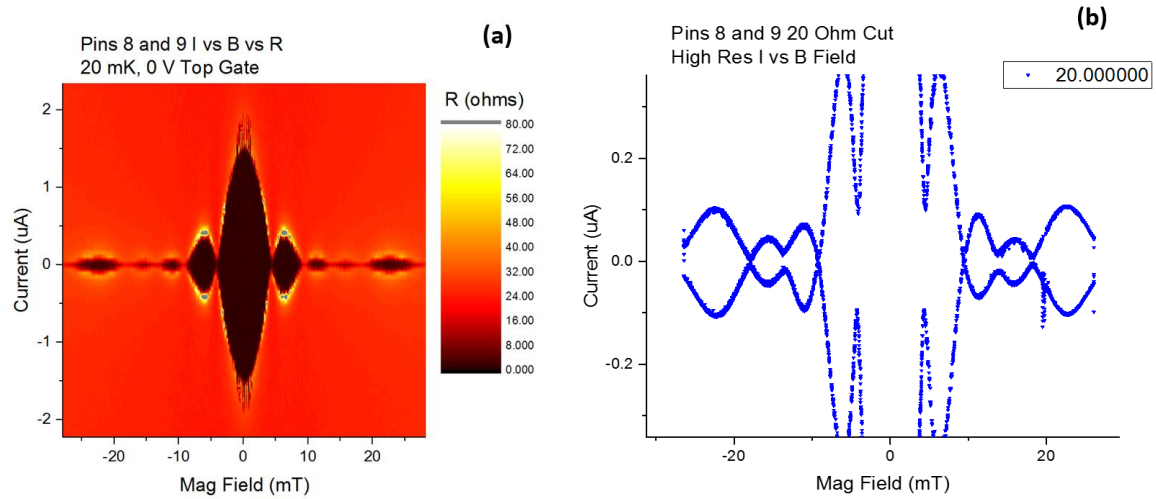

Figure 4.13: a) left shows contour plot diffraction pattern for another TIJJ with no BIS buffered layer with differential resistance of the device being the color scale b) extrapolated Ic vs B plot for the left figure with no contour color shows an obvious even-odd node-lifting effect.

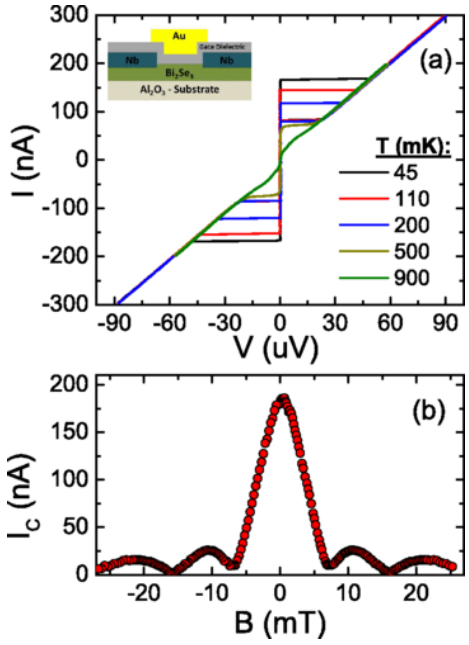

Figure 4.14: (a) The IV characteristics of the TIJJ at different temperatures. Inset: a schematic representation of the junction cross-section. (b) The critical current vs magnetic field modulation with the first node lifted in both positive and negative field, and 2nd nodes pinned down to zero. [59]

(2) Inhomogeneity usually lifts all nodes and we see the first node is lifted but the second node is not, and third node is lifted, but the fourth node is not, and it is symmetric about the y-axis for the negative field direction. We then tried to add asin $\left(\frac{\phi}{2}\right)$ term to the CPR and simulate the single junction diffraction pattern, as we can see from the following plot. We can see that 5% of the sin $\left(\frac{\phi}{2}\right)$ component easily lifts all the odd nodes, and pins all the even nodes to zero, which is in good agreement with our experimental data.

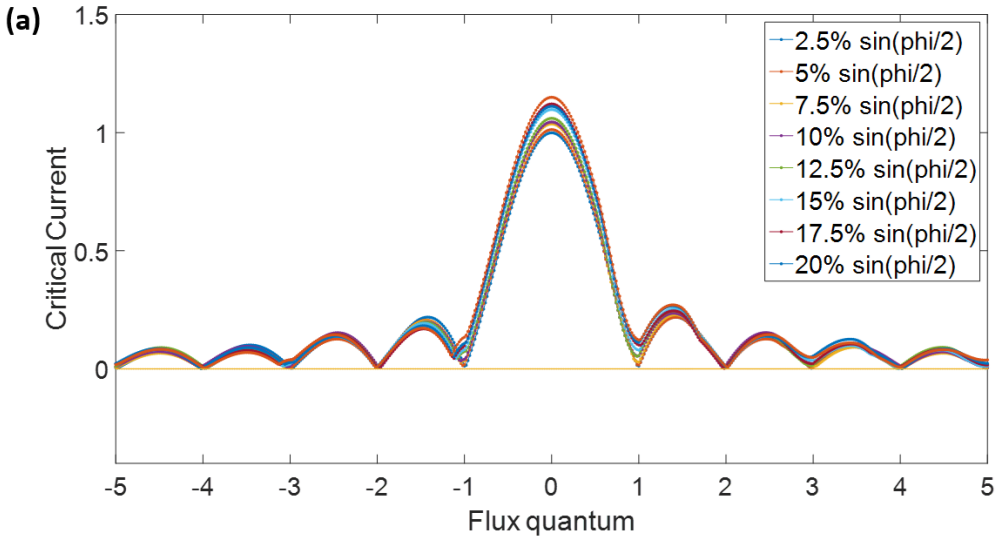

Figure 4.15: a) Matlab simulation of single TIJJ showing correction of node-lifting vs percentage of supercurrent carried by the $sin\left(\frac{\phi}{2}\right)$ *component.*

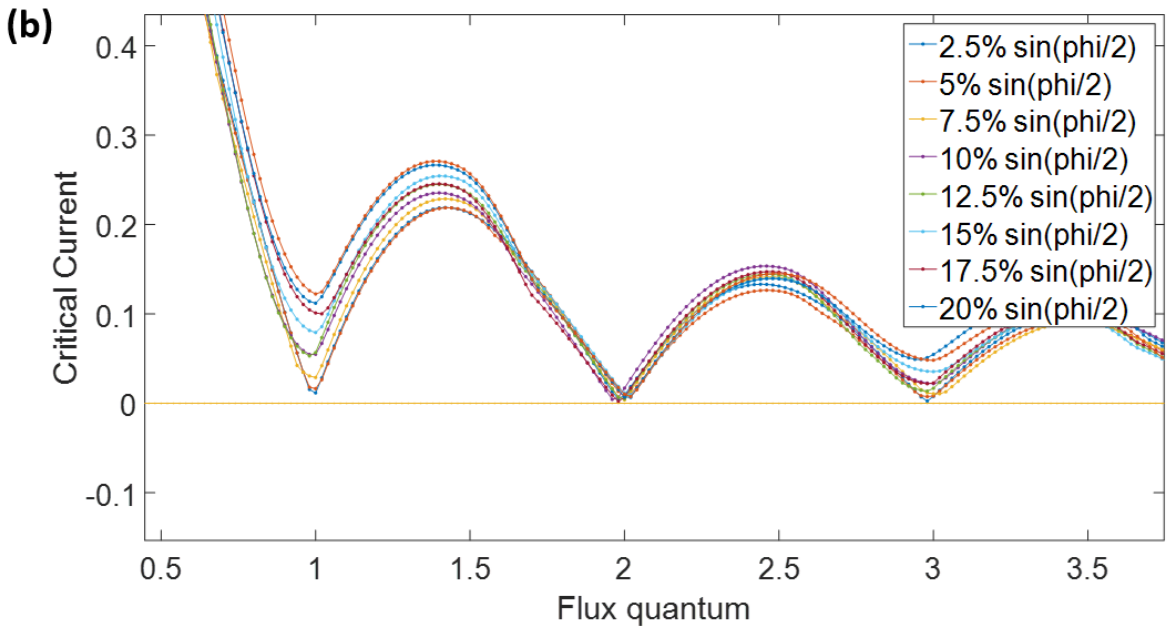

Figure 4.15 b) zoom in view at the nodes of the diffraction pattern for different percentage of supercurrent carried by the $sin\left(\frac{\phi}{2}\right)$ *component.*

(3) The node-lifting for our junctions is very large, typically ~5-15% of the maximum critical current, which would require unreasonably large amounts of disorder or systematic asymmetries in the junction properties. A numerical simulation was carried out in Matlab, and we introduce the disorder in the total critical current as a random fluctuation times a critical current scaling factor. We noticed that it takes up to 50%-60% of disorder to have a noticeable lifting of nodes in the single junction diffraction pattern. From SEM picture of our single junctions, we knew that our junction has relative straight parallel edges with no significant fabrication artifacts, thus the even-odd node-lifting effect is unlikely to be caused by the disorder.

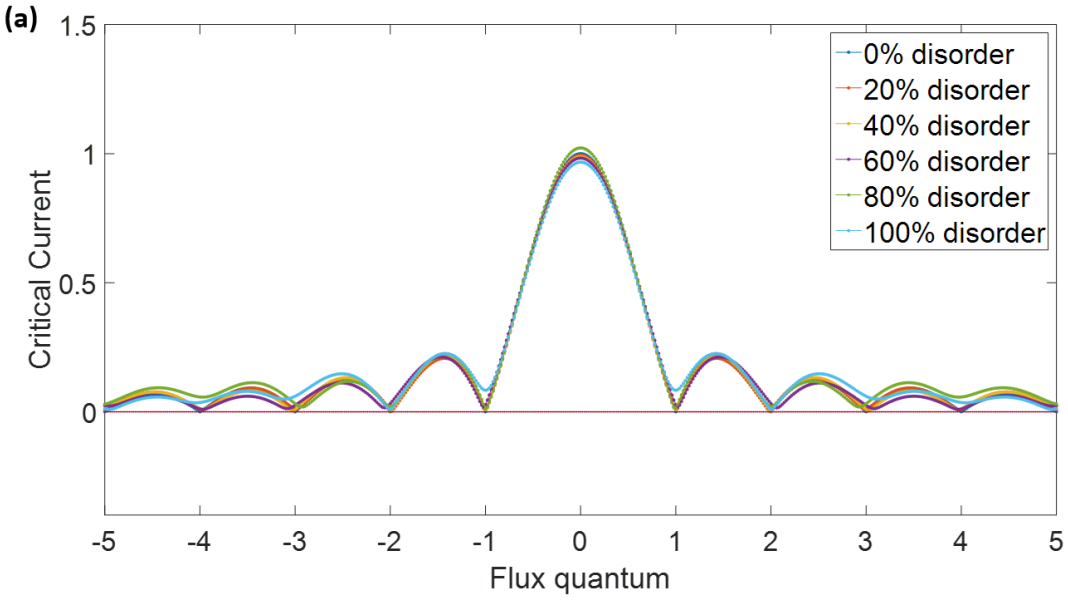

Figure 4.16 a) Matlab simulation for single junction diffraction pattern with different amounts of critical current disorder

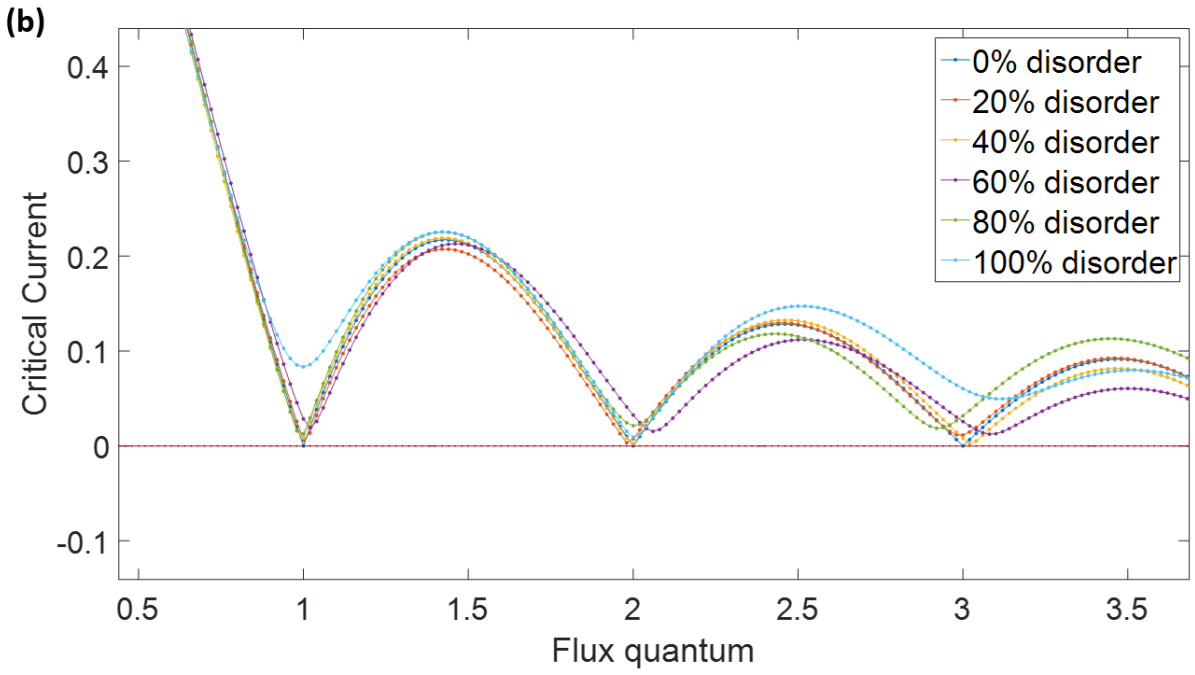

Figure 4.16: b) Zoomed-in view of the nodes for inspecting node-lifting effects vs magnitude of critical current disorder.

After carrying out systematic tests to rule out the origin of an even-odd node-lifting effect due to critical current disorder and flux focusing effects, we adopted Fu and Potter's MBS model [70] to explain our diffraction data. If a Majorana zero energy bound state is present in the junction in the core of the vortices, it enables a single quasi-particle electron to tunnel through the Josephson barrier to carry the supercurrent. The transition of the supercurrent charge carrier from 2e to 1e doubles the Josephson period from 2π to 4π. Similar anomalous Josephson effects were also predicted to appear in cuprates' pair-density wave Josephson junctions, in which a 4e charge carrier condensate state is present, introducing a $\sin(2\phi)$ component into the CPR in addition to the conventional $\sin(\phi)$ component. Fig. 4.17 is a schematic picture describing the physical scenario of how supercurrent is carried by ABS.

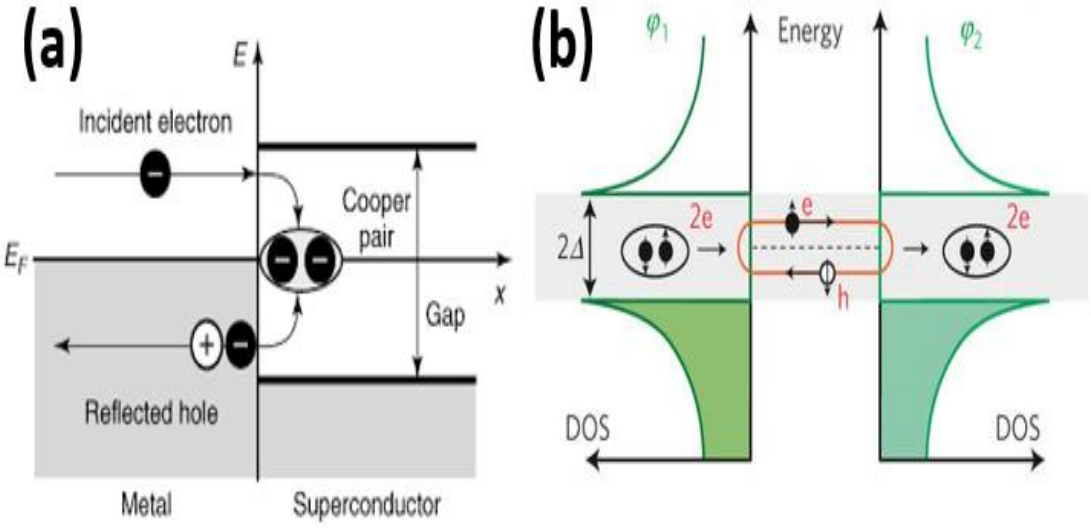

Figure 4.17: a) A schematic picture describing the Andreev reflection process at a superconductor-normal metal (SN) junction [71], b) A schematic picture describing Josephson supercurrent carried by ABS in a SNS Josephson junction[72].

When we try passing current from a piece of normal metal into an s-wave superconductor, due to the fact that conduction band and valence band are gapped out in the superconductor and all electrons are paired up as Cooper pairs residing at the Fermi level, there is no available density of states for the incident electrons. In order to pass the current, the incident electron grabs another electron from the Fermi sea in the normal metal, and pairs up as a Cooper pair propagating through the superconductor, together with a reflection of a hole into the normal metal in the opposite direction of the incident electron to conserve the total charge and momentum. This process is called Andreev reflection. If we placed another superconductor on both sides of the normal metal, we would have Andreev reflection processes from both sides of the normal metal. The difference here is that when a hole reflected back to the left side, it would reflect another electron out to the right side, which forms a dynamic equilibium process. The reflected electron-hole pair resides above

and the below the fermi level, respectively, and such process is called an Andreev bound states, which can carry a lossless supercurrent.

Fig. 4.18 shows a schematic picture of Fu and Potter's MBS picture for a lateral S-TI-S Josephson junction [59]. A lateral S-wave superconductor at the top (blue layer labeled as SC) is in contact with the the bottom layer of topological insulator (grey layer labeled as TI).

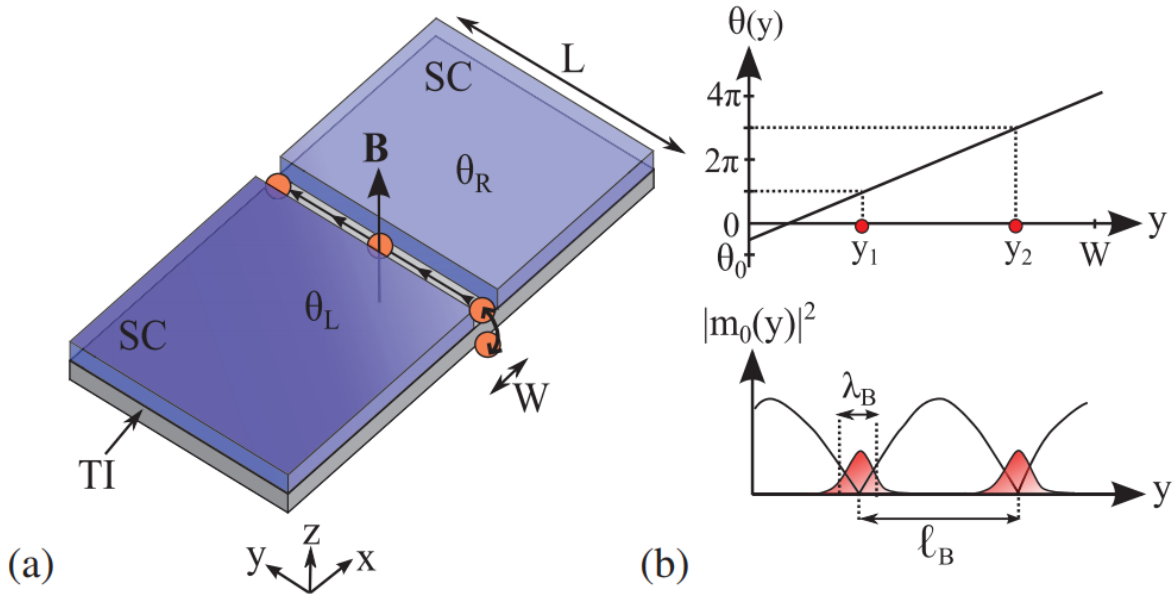

Figure 4.18: (a) S-TI-S Josephson junction device geometry. (b) Phase diagram of localized Josephson vortices generated in the junction when the phase along the junction is of odd-multiples of π[59].

As the global phase between the two sides of the junction ($\theta_0 = \theta_R - \theta_L$) is adjusted by the external magnetic field, Josephson vortices are formed and localized at the junction when the total phase across the junction is equal to odd multiples of π. We would have an electron-hole pair residing right at the zero-energy level. Such a zero-energy ABS, also referred to as a MBS, can host Majorana fermions at the center of the Josephson vortices, which are predicted to exhibit non-Abelian statistics. The superconducting order parameter is zero at the center of the vortex, thus it

can allow a quasi-particle single electron to carry current through it. It is worth to mention that it is well known that in nanowire systems Majorana fermions are predicted to reside the two ends of the nanowire, though it is still a open question for whether there exist Majorana fermions in a 3D TI JJ system.

We then use the following equation to simulate the current-phase relation of our S-TI-S Josephson junction, where Is is the total supercurrent carried in the junction, ϕ is the phase of the junction, I_{2e} is the magnitude of the conventional 2π periodic Josephson supercurrent, I_{MF} is the magnitude of the supercurrent carried by the MBS, and $\alpha(\phi)$ is a localized delta function about the localized Josephson vortices that we used a Gaussian distribution function to describe, which is related to the effective percentage of critical current contribution by the $sin\left(\frac{\phi}{2}\right)$ component.

$$I_s(\phi) = I_{2e}\sin(\phi) + \alpha(\phi) * I_{MF} * \sin\left(\frac{\phi}{2}\right) \tag{49}$$

$$\alpha(\phi) = \begin{cases} \frac{1}{\sqrt{2\pi\sigma^2}} e^{-\frac{(\phi-(2n+1)*\pi)^2}{2\sigma^2}} & when\ \phi \approx (2n+1)*\pi \quad n\ is\ an\ integer \\ 0 & otherwise \end{cases} \tag{50}$$

Numerical simulation was carried out using the above model, and results are displayed in Fig. 4.19. A periodic Gaussian function was used to describe the Josephson vortex shown in Fig. 4.19 a). The standard deviation of the Gaussian distribution function σ describes the tunable width of the Josephson vortex, where the Josephson vortex is generated when ϕ equals to odd-multiples of π.

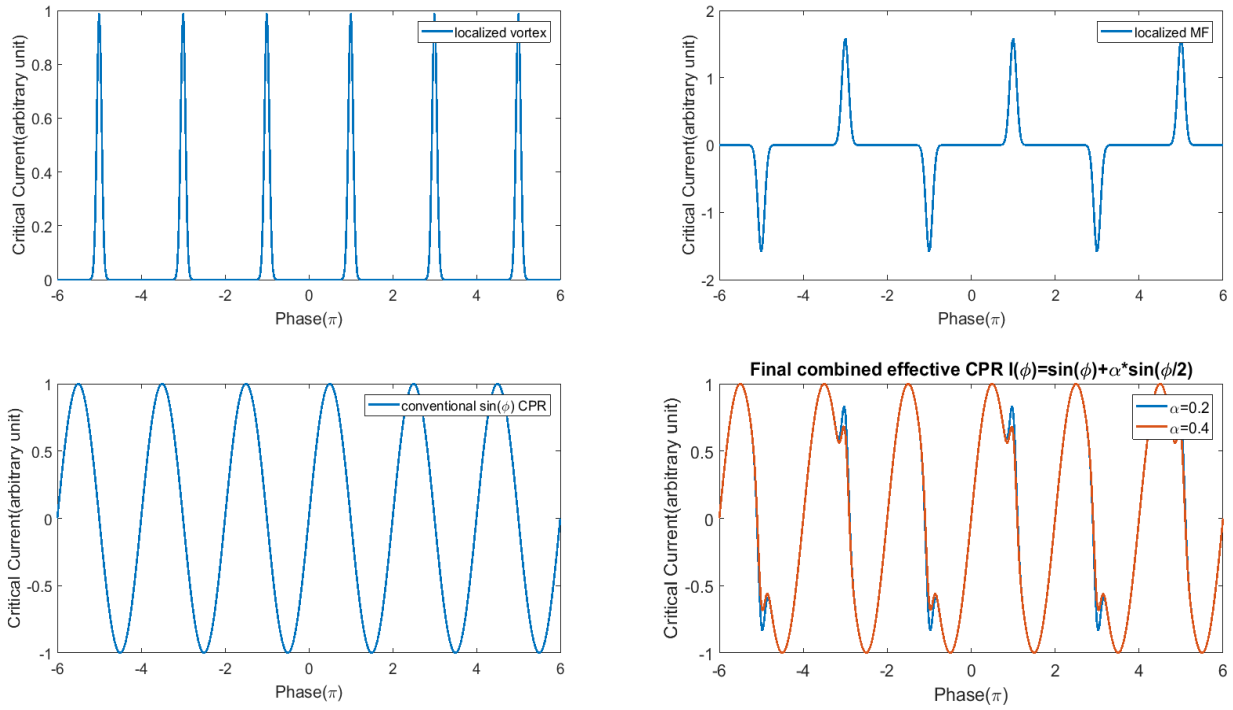

Figure 4.19: a) Periodic Gaussian distribution with normalized peak of 1 at odd-multiples of π and zero elsewhere, b) Effective CPR of sin $\left(\frac{\phi}{2}\right)$ component multiplied by the localized gasussian function, c) conventional sinusoidal 2π periodic CPR, d) Effective combined CPR of both b) and c) with different percentage of sin $\left(\frac{\phi}{2}\right)$ contribution to the total critical current.

Due to the 4π periodic nature of the MBS, we then multiply the Gaussian function by $\sin\left(\frac{\phi}{2}\right)$, which would then yield $\alpha(\phi) * \sin\left(\frac{\phi}{2}\right)$ shown in Fig. 4.18 b). Fig. 4.18 c) shows the 2π periodic Josephson junction CPR, and we combined the conventional 2π component with the 4π component in equation 49, from we would get the total effective CPR which is shown in Fig. 4.18 d) . As we can see from Fig. 4.18 d), the blue line describes the lower percentage of the $\sin\left(\frac{\phi}{2}\right)$ component with $\alpha = 0.2$ and the red curve represent a higher percentage of $\sin\left(\frac{\phi}{2}\right)$ component with $\alpha = 0.4$, which can correlate with the quality of the topological insulator and its mobility and carrier density. The smaller the bulk carrier density and higher the surface state mobilitiy, the

higher value of α we should see. The combined effective CPR has a pronounced spike feature which is 4π periodic for $\alpha = 0.4$, and the spike feature is smeared out and almost not noticeable in the blue curve for $\alpha = 0.2$. In general, the total supercurrent flowing across the junction is a complex function that depends on the CPR with the following function form, shown in Fig 4.19, due to a wide range of physical effects including inhomogeneity in the critical current, order parameter symmetry, trapped vortices, magnetic domains, and localized MBS locating at the core of the Josephson vortex is of most relevance to this experiment.

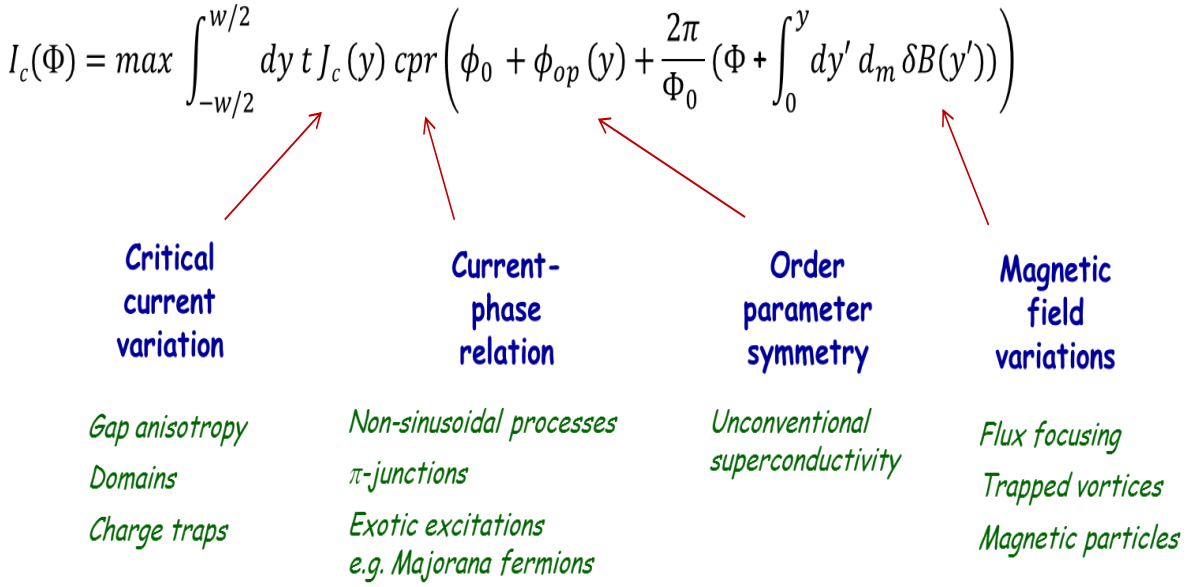

Figure 4.20: General expression for the critical current of a Josephson junction and CPR

We then integrated the CPR with the critical current density along the junction, and we get the simulated critical current versus external magnetic field diffraction pattern as in Fig. 4.21. As we can see from Fig. 4.21, it has a Fraunhofer-like pattern. Furthermore, it has an even-odd node lifting effect, which we interpret as the 4π periodic Josephson effect. It also has a shoulder glitch feature highlighted in the red box, corresponding to the entry of the first Josephson vortex, which is related with the first pair of MBS in the junction. This was confirmed by the phase dynamics in

the junction with an abrupt change of phase in the junction when a vortex enters the junction, which was shown in Fig. 4.21 b) highlighted with the yellow arrows.

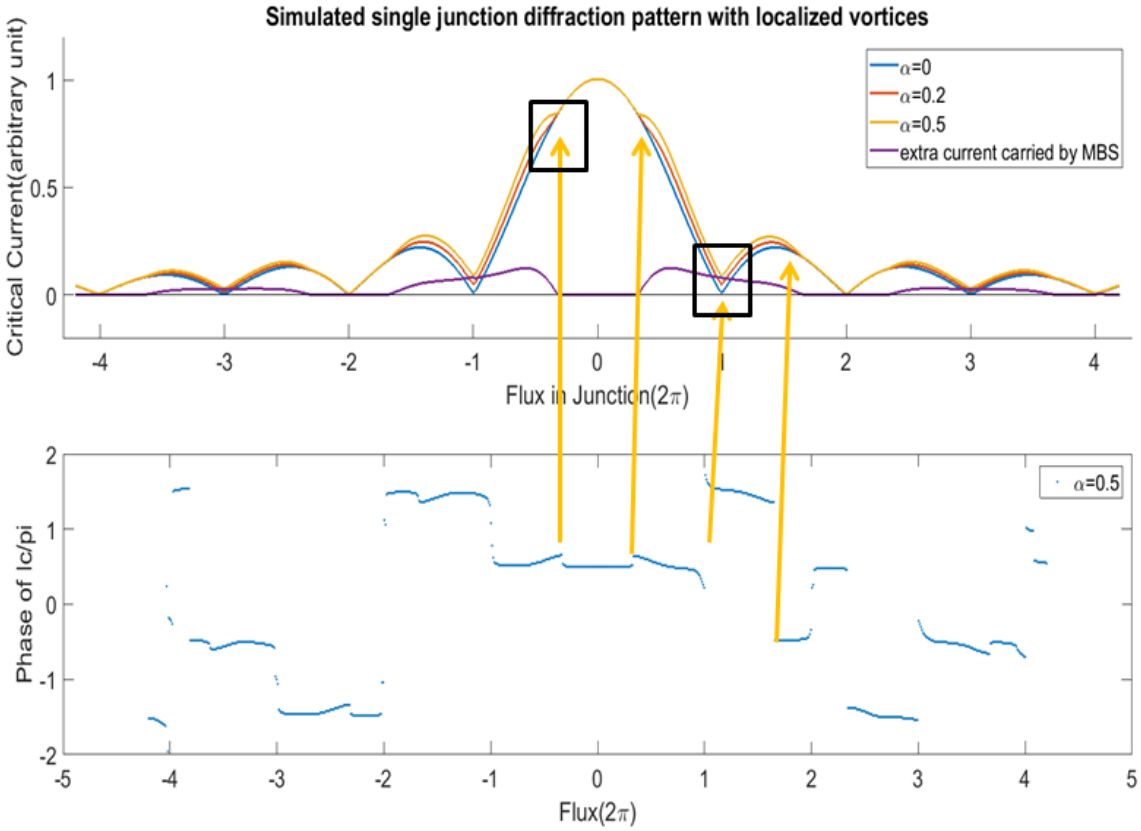

Fig. 4.21 a) Simulated single junction critical current versus magnetic field diffraction pattern using the postulated effective MBS CPR described in equation 49 with $\alpha = 0$, 0.2 and 0.5. b) Phase winding of the junction as a function of external magnetic field.

The purple trace in Fig. 4.21 a) was obtained by subtracting the conventional diffraction pattern from the case of $\alpha = 0.5$. This is consistent with our model that localized Josephson vortex enters the junction at every odd multiple of $\phi = (2n + 1) * \pi$, corresponding with the appearance of one pair of MBS. The extra current would be carried by the 1st pair of MBS at $\phi = \pi$, and the current would vanish to zero when the 2nd pair of MBS enters the junction at $\phi = 3\pi$, and reappears at $\phi = 5\pi$.

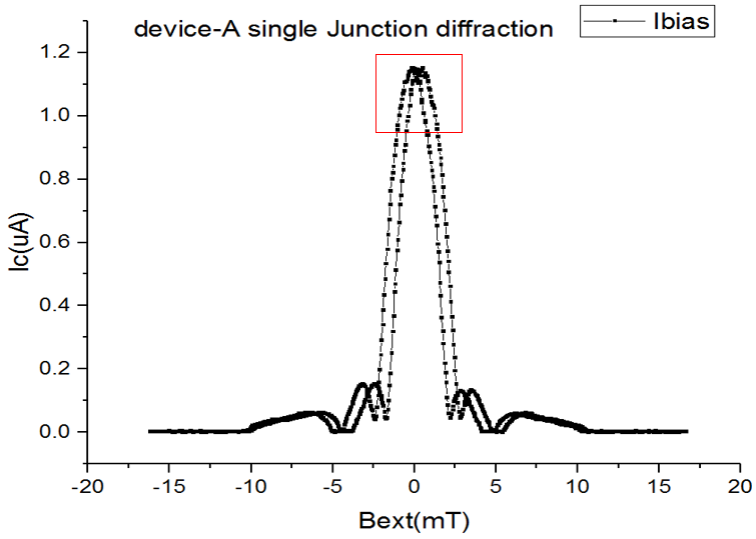

Figure 4.22: trace and retrace of single junction diffraction pattern with even-odd node-lifting effect, and vortex entry feature highlighted in the red box.

As we can see from the comparison of Fig. 4.21 a), and Fig. 4.22 , our measured single junction data is in good agreement with the simulated single junction diffraction pattern with a combined effective CPR composed of a localized 4π periodic component.

4.6 Conclusion

We have made a series of TIJJ with long and thin bar geometries, and we have found the magnetic penetration length for our TIJJ to be $\lambda = 85nm$. The normal metal coherence length of high quality Bi_2Se_3 thin films with buffered BIS layer is $\xi_N^1 = 22.18 \pm 13.54\, nm$ and $\xi_N^2 = 112.72 \pm 17.22\, nm$, indicating the supercurrent is carried by two types of superfluid with different decay length scale. Strong evidence of 4π periodic Josephson effect was observed in our TIJJ via even-odd node-lifting effects in our single junction diffraction pattern, together with an abrupt vortex entry feature, which we interpret as the entry of the first pair of MFs. We have tested the origin of an even-odd node lifting effect due to critical current density distortion or flux focusing effects from the geometric TIJJ testing results and numerical simulation. We extended Fu and Potter's localized MBS model to simulate the TIJJ diffraction pattern and our measured results are in good agreement with theory. In short, we would like to conclude that we have observed 4π periodic Josephson effect in our TIJJ.

Chapter 5. Asymmetric SQUID Experiment Results and Discussion

In this chapter, we will present our study of direct CPR measurements of Nb-Bi_2Se_3-Nb TIJJs using an asymmetric SQUID configuration. We will first explain the working mechanism of the asymmetric SQUID, and then we will present measured experimental CPR data from a TI asymmetric SQUID. We will compare this data to numerically simulated asymmetric SQUID data with a $\sin\left(\frac{\phi}{2}\right)$ component in the CPR. Prior to these experiments, skewness in TIJJ CPR has been indirectly extracted from SQUID diffraction pattern by C. Kurter et al [73], and a skewed CPR in a TIJJ has only been directly observed using a scanning SQUID microscope pick-up loop technique [71]. In contrast, we use a direct electrical transport measurement technique to observe the skewness in the CPR of our TIJJ. The presence of skewness in this system is indicative of the high-transparency surface states of the 3D topological insulator Bi_2Se_3. We also observe this skewness decrease as we increase the sample temperature, until it disappears entirely. This is due to quasiparticle scattering effects from thermal electrons in bulk channels, which reduce the transparency of the Josephson weak link barrier and effectively reduce the skewness.

5.1 Introduction

The current-phase relation (CPR) of a Josephson junction (JJ) describes how the supercurrent changes as a function of the phase difference of the superconducting order parameter across the junction. The CPR of a JJ plays an essential role in understanding how the superconducting order parameter propagates through the weak link barrier, especially in the case of TIJJ and its exotic topological order phases. A conventional Josephson Junction has a sinusoidal CPR, $I_s(\phi) = \mathrm{Ic} * \sin(\phi)$. TIJJs are predicted to host MBS, which enable a supercurrent carried by a quasiparticle single electron instead of Cooper pairs, thus doubling the Josephson period from

2π to 4π[9]. Probing the CPR of a TIJJ would be crucial for identifying this 4π periodic Josephson effect, which is one of the key characteristics of MBS. Previous scanning SQUID microscopy (SSM) measurements of Al-Bi_2Se_3-Al [74] and Nb-HgTe-Nb Josephson junctions [75] showed a forward skewness in the CPR, which was attributed to the high transmittance of topological surface states. However, they did not observe direct evidence of a 4π periodic Josephson effect. High frequency RF techniques have also been used to study the CPR of HgTe [76] and InAs [77] nanowire Josephson junction systems, where a 4π periodic Josephson effect was observed through measuring voltage-doubled Shapiro steps, however whether such 4π periodic Josephson effect originates from MBS is not yet confirmed.

In the previous single junction results section, Chapter 4, we presented a comprehensive study of TIJJ single junctions, and deduced a 4π periodic Josephson effect via an even-odd node-lifting effect in the magnetic diffraction pattern. Adapting the technique of the Goswami group [31], who used an asymmetric SQUID configuration to study the CPR of a high-quality graphene Josephson junction, here we have used an asymmetric SQUID technique to study the CPR of TIJJ to further testify the existence of $\sin\left(\frac{\phi}{2}\right)$ component in the CPR of TIJJ. Recall that we have explained the working principle of the asymmetric SQUID technique with both an analytical approximation and a numerical simulation in Chapter 2.3, using the PDW example. From equation 43 and 44 in Chapter 2, we demonstrated that we can directly extract the CPR of the smaller junction by looking at the top of the SQUID diffraction pattern near zero field. The phase of the bigger junction is fixed around $\frac{\pi}{2}$ and thus contributes nearly constant supercurrent, and the change of the phase in the SQUID pattern would be equal to the phase change in the smaller junction, $I_s(\Phi_{ext}) \approx I_{c1} + I_{c2}(\Phi_{ext}, \phi_2)$.

We then conducted a similar numerical simulation for a TIJJ asymmetric SQUID. We postulate an extra $\sin\left(\frac{\phi}{2}\right)$ component in the CPR, which well explains our TIJJ single junction data. Here, we applied the predicted CPR from Chapter 4, equation 49 and 50, and we simulate the diffraction pattern for the asymmetric SQUID. In Fig 5.1. a), we present an overview of the simulated asymmetric SQUID diffraction pattern composed of both a single junction decay envelope and the SQUID modulation. If we zoom in on the red boxed region in Fig. 5.1 a), we obtain the extracted CPR from the simulated asymmetric SQUID diffraction pattern, which is what we would expect to see from our experimental measured asymmetric SQUID data. There are three main features worth pointing out. First, we noticed that a smaller side peak feature, corresponding to the localized 4π periodic ABS that carries the extra current, is most visible near the zero-field region in the extracted CPR, where the single junction decay envelope has minimal effect. However, such a feature is hardly noticeable due to the single junction decay envelop smearing it out, highlighted by red and green arrows in Fig.5.1 b). This implied that we should make the SQUID loop large compared to the single junction, to keep us from losing the 4π periodic ABS feature in the CPR to single junction effects. For c) and d), we can see that while the phase of the bigger junction is fixed around $\phi_1 \approx \frac{\pi}{2}$, the phase of the smaller junction ϕ_2 keeps winding as the external magnetic field keeps changing. This means that we are effectively measuring the CPR of the smaller junction when we are measuring the asymmetric SQUID diffraction pattern.

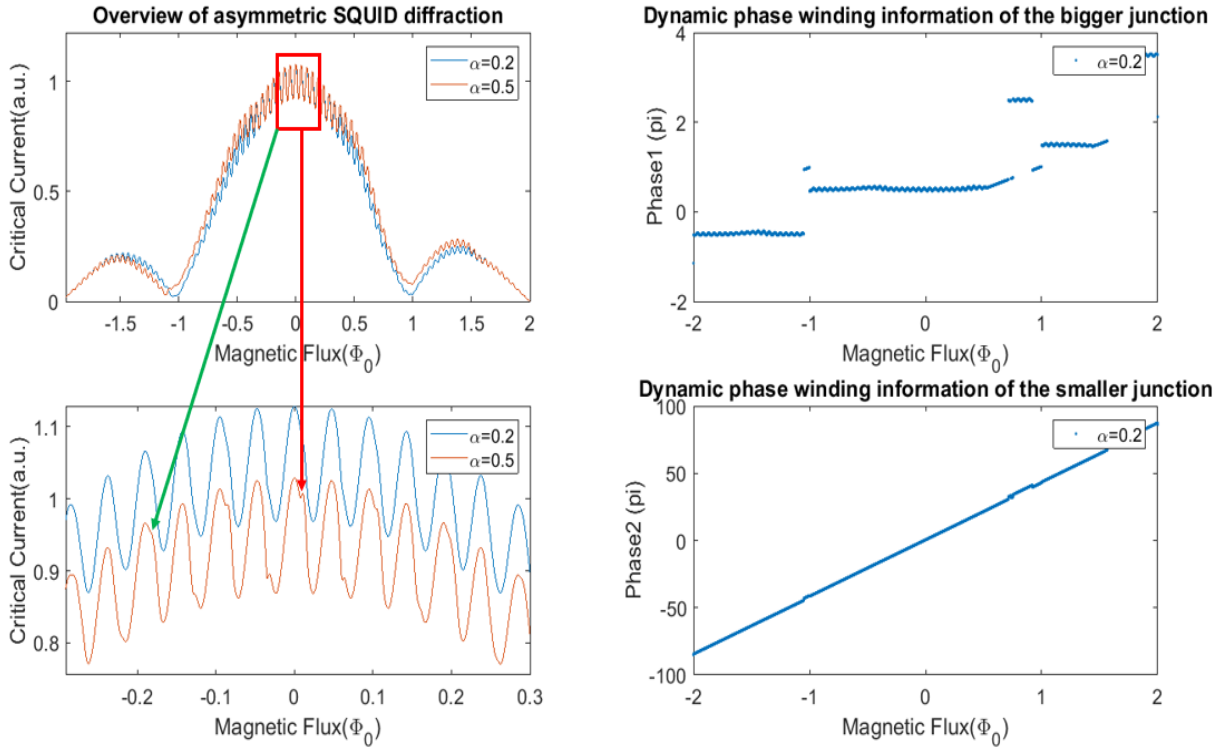

Figure 5.1: Matlab simulation of asymmetric SQUID diffraction pattern with two different percentage of $sin\left(\frac{\phi}{2}\right)$ *component in the CPR. a) Overview of SQUID diffraction pattern with single junction envelop. b) Zoom in view of the red boxed region to extract the CPR of the smaller junction at the top of the peak at zero field. c) Near zero field when the critical current of the larger junction is near maximum, the phase of the larger junction is fixed around* $\frac{\pi}{2}$*. d) The phase of the smaller junction in the asymmetric SQUID keeps winding as the external magnetic field is changing, and the phase of the junction now is effectively determined by the phase of the smaller junction.*

To further test the validity of extracting the CPR by using the asymmetric SQUID technique, we compared our extracted CPR data from the simulated asymmetric SQUID diffraction pattern, shown in Fig. 5.1 a), to the postulated CPR containing a 4π periodic $\sin\left(\frac{\phi}{2}\right)$ component from Chapter 4, equation 49, shown in Fig. 5.1 b). First, there is a small deviation in the CPR from conventional sinusoidal CPR that is 4π periodic for both figures, as highlighted by the black box and black arrows in both figures. Such consistency is amplified when a larger α value with a sharp spike feature is present in the CPR, where α represents the percentage of the

$\sin\left(\frac{\phi}{2}\right)$ component in the total CPR. Secondly, the extracted CPR from the asymmetric SQUID has a parabolic background due to the single junction decay effect. Thus, we can see that when we used the postulated 4π periodic CPR due to the localized ABS to simulate the asymmetric SQUID diffraction pattern, we can retrieve the CPR information by zooming in the region near zero field where the phase and critical current magnitude of the larger junction are fixed.

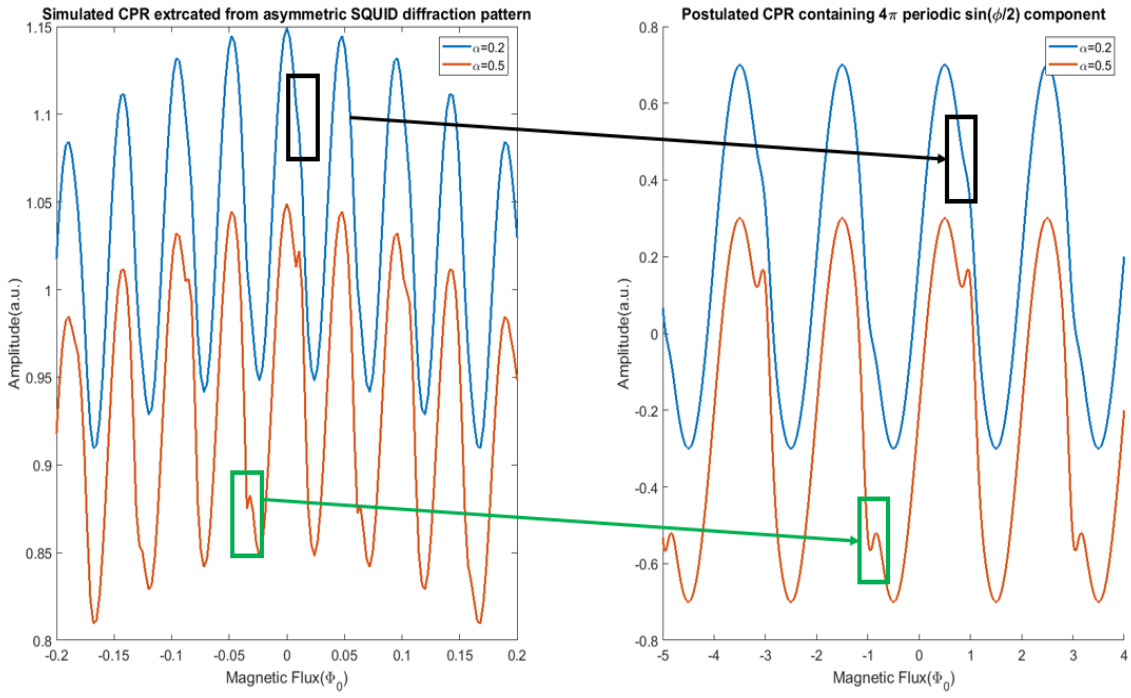

Figure 5.2: a) Simulated CPR extracted from the top of the asymmetric SQUID diffraction pattern near zero field with two different value of $\alpha(\phi)$ b) Postulated CPR from Chapter 4 equation 49 with two different value of $\alpha(\phi)$.

In the next section, we will present our direct measurements of CPR data using the asymmetric SQUID technique that we have just explained.

5.2 Asymmetric SQUID Results and Analysis

Our TIJJ asymmetric SQUIDs were made using the similar e-beam lithography techniques described in Chapter 4. The difference here is that the device geometry is an asymmetric SQUID shape rather than single junction devices. Fig. 5.4 shows a typical SEM picture of our asymmetric SQUID devices, where the two arms of the SQUID have different junction lengths leading to the two arms contributing different magnitude of supercurrent. All our electrical measurements are conducted in our cryogen-free dilution refrigerator in a 4-terminal configuration with current and voltage probes depicted in Fig 5.4. An external magnetic field is applied in the out of plane direction, threading flux through the SQUID loop.

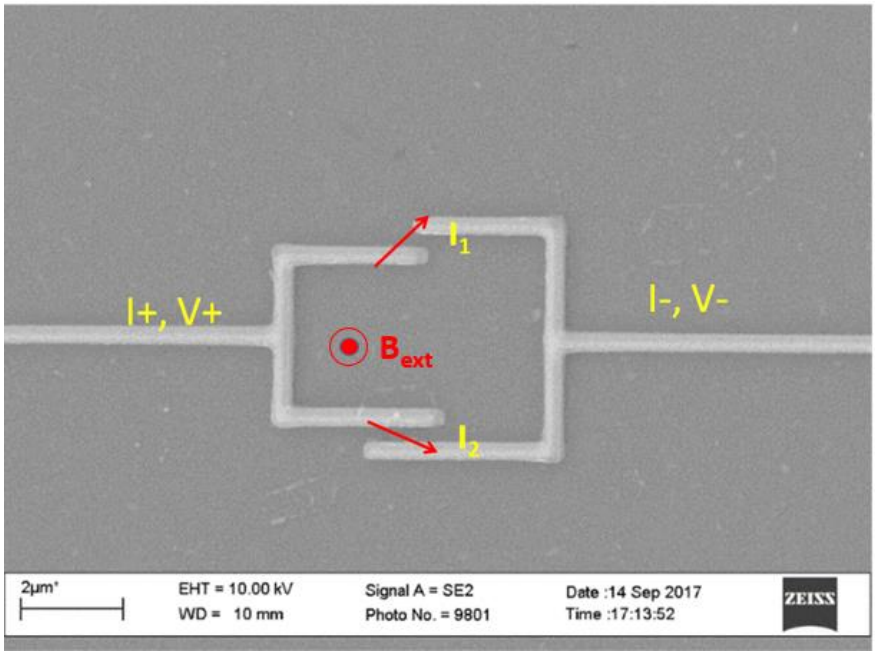

Figure 5.3: SEM picture of our asymmetric SQUID devices.

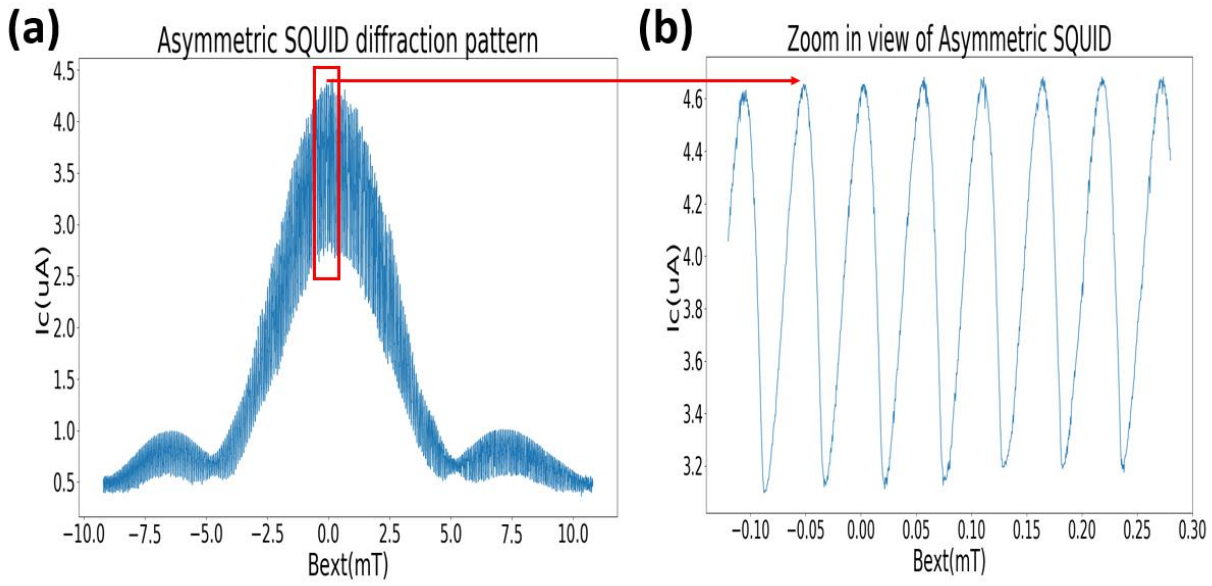

Figure 5.4: a) Measured asymmetric SQUID I_c vs magnetic field modulation pattern b) high-resolution scan zoom-in at the top of the SQUID diffraction pattern near zero field.

Fig 5.4. a) shows our measured asymmetric SQUID diffraction data composed of a fast SQUID modulation bounded within a Fraunhofer-like single junction envelope, over many SQUID periods. The SQUID modulation period depends on to the ratio of the SQUID loop area to the area of the larger single junction, which sets the single junction decay envelope. In order to extract the CPR information, we zoom in at the top of the SQUID modulation near zero field, where the critical current is nearly constant, and we will directly obtain the CPR for the smaller junction as shown in Fig. 5.5 b.

Fig. 5.5.a) shows the measured CPR for our asymmetric SQUID at different sample temperatures. In Fig. 5.5. b), we subtract the vertical offset, and then in Fig. 5.5 c) the magnitude of the critical current is normalized to 1 for all the CPR curves. Comparing Fig. 5.5 c) with our simulated asymmetric SQUID CPR in Fig. 5.1. and Fig. 5.2, we didn't see a sharp 4π periodic spike feature in the measured CPR. We added a repeating red vertical line intersecting with the zero-critical current point of each CPR, where the spacing between each vertical line equals to a

2π period of each CPR. The vertical scale is intentionally offset for better demonstration purposes. We subtracted the processed CPR in Fig. 5.5 c) with a conventional 2π periodic CPR $\sin(\phi)$, which would give us the extra unconventional component in the CPR shown in Fig 5.5 d). The remaining CPR does not show any 4π periodicity in Fig. 5.5 d).

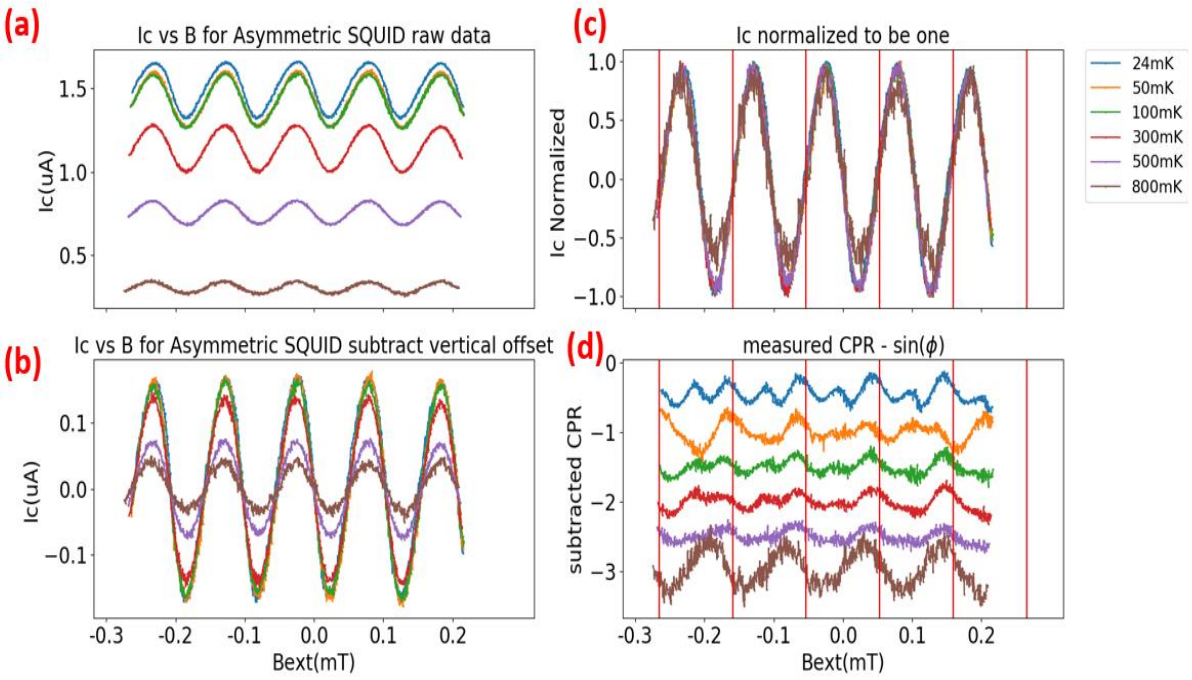

Figure 5.5: a) waterfall plot of CPR at different sample temperature with color encoded legend b) the vertical offset was subtracted to show the SQUID modulation amplitude at different sample temperature c) CPR was normalized to be 1 to calculate the skewness d) A 2π periodic CPR $sin(\phi)$ was subtracted from the measured CPR which would give us the unconventional CPR component

Skewness was observed in our TIJJ CPR, and we explored the temperature dependence of the skewness. The skewness in our CPRs is parametrized by a variable $S = (\frac{2\phi_{max}}{\pi} - 1)$[32], where ϕ_{max} is the horizontal value of the maximum of the CPR curve as depicted in Fig. 5.6. The CPR would be a purely sinusoidal curve if S=0, and it would have a have a sharp transition from the positive maximum to the negative maximum at a phase of π when S=1.

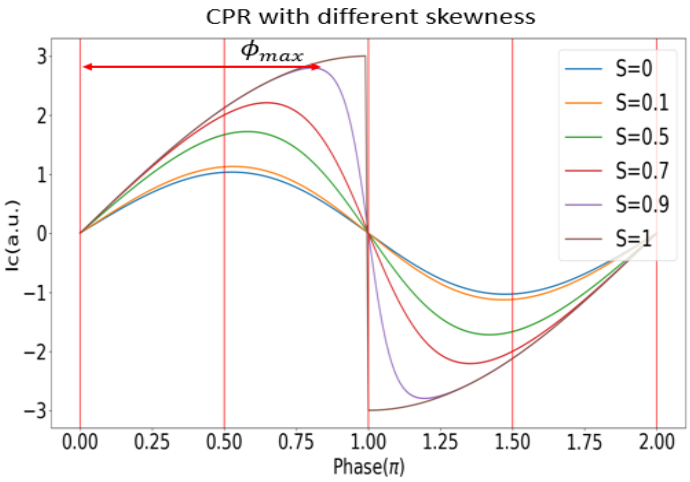

Figure 5.6: Evolution of CPR at different skewness with red vertical lines marking every $\phi = \frac{\pi}{2}$

A skewed CPR has been previously reported in break junctions, point contact junctions, and graphene Josephson junctions being in the ballistic transport limit $L_j < l_{mfp}$, where L_j is the junction separation length and l_{mfp} is the mean free path in the material. For this reason, forward skewness is usually not expected in the diffusive regime, where the junction gap size is larger than the mean free path $L_j > l_{mfp}$. Our TIJJ asymmetric SQUID has junction gap size ranging from 300nm to 400nm, which is in the diffusive Josephson junction regime. We think the skewness is related to the high transmittance ABS due to the symmetry protected topological surface states, which is known for robust against scattering defects. The origin of the surface states arises from strong spin-orbit coupling, which leads to spin-momentum locking suppressing any spin-flip back scattering with electrons in bulk channels. This is consistent with the conclusion from the Moler group previous report [75], where they observe skewness that persists for l ranging from 200nm to 600nm, and their estimated mean free path $l_{mfp} \approx 200nm$. We explored the temperature dependence of the skewness vs the sample temperature, and we found out that skewness decreases as we increase the sample temperature as shown in Fig. 5.7 b). The decrease of skewness in our

TIJJ can be understood as an increase amount of thermal-electrons scattering with spin-momentum locked surface state electrons reducing the transparency of the Josephson barrier. At lower temperature, the transport is dominated by high transparency surface state carriers, which has a fixed number of channels for given junction geometry. At higher temperature, the number of thermal excited quasiparticle electrons increases, and critical current of the small junction keeps decreasing due to weaker superconducting proximity effect. It is worth mentioning that a negative skewness is usually related with large junction inductance β_L, which is usually caused by large critical current in the junction. Here, we believed that the small negative skewness can be caused by noise rounding and inaccuracy in determining the location of ϕ_{max} when the junction is approaching sinusoidal CPR at higher sample temperatures.

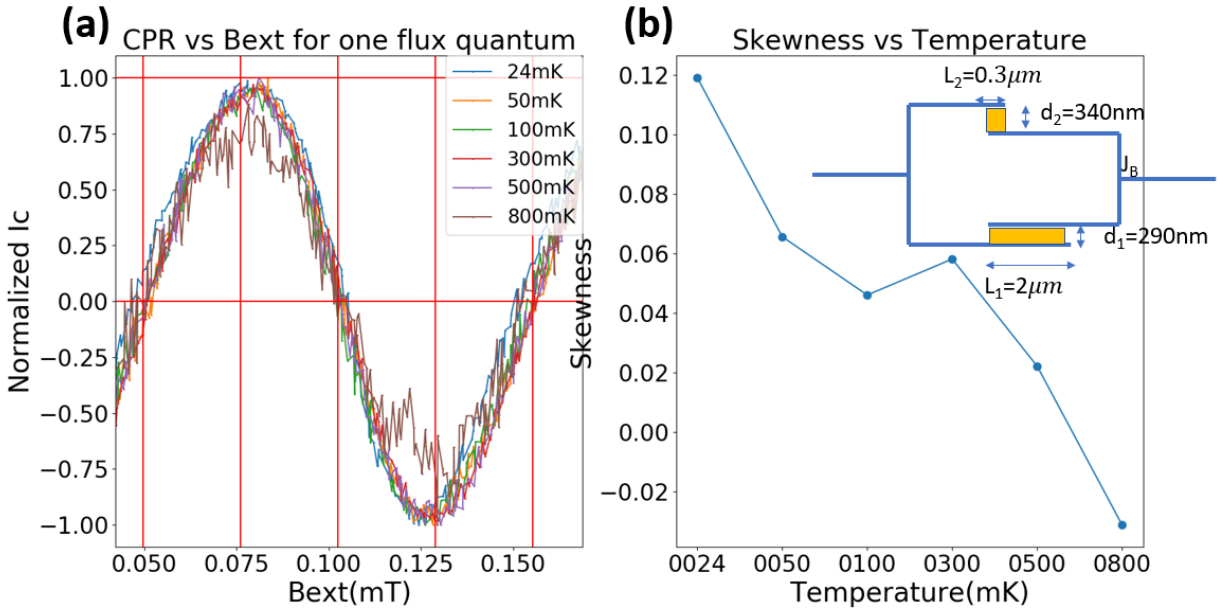

Figure 5.7: a) Zoom in view of one full period for the CPR of asymmetric SQUID at different temperatures. b) Calculated skewness dependence as a function of temperature with the asymmetric SQUID geometry in the inset.

We have measured the CPR of several other asymmetric SQUID junctions, and we processed the CPR data using the same steps. Here are the results showing in Fig. 5.7, Fig. 5.8,

and Fig. 5.9 with the junction geometry information attached. The junction carries the smaller critical current is labeled with subscript of L_1 and d_1, where L is the length of the junction, and d is the gap separation between the two superconducting electrodes.

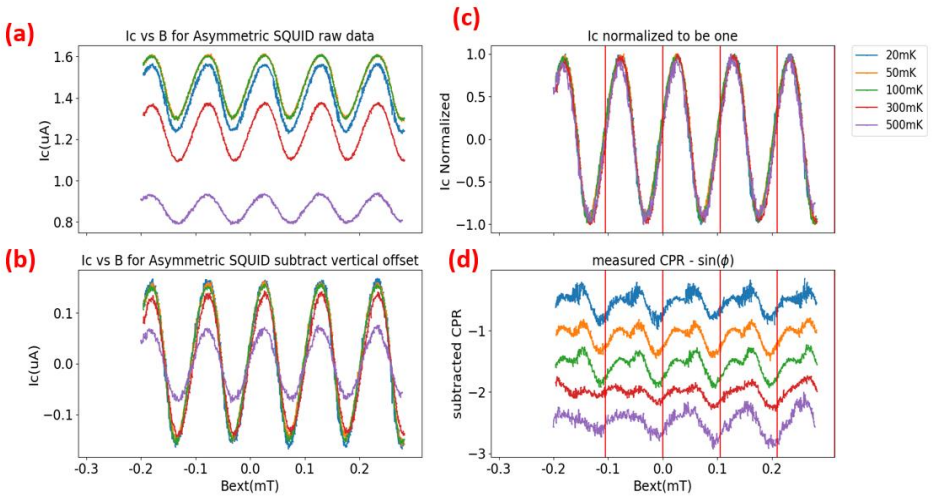

Figure 5.8: a) waterfall plot of CPR at different sample temperature with color encoded legend b) the vertical offset was subtracted to show the SQUID modulation amplitude at different sample temperature c) CPR was normalized to be 1 to calculate the skewness d) A 2π periodic CPR $sin(\phi)$ was subtracted from the measured CPR which would give us the unconventional CPR component

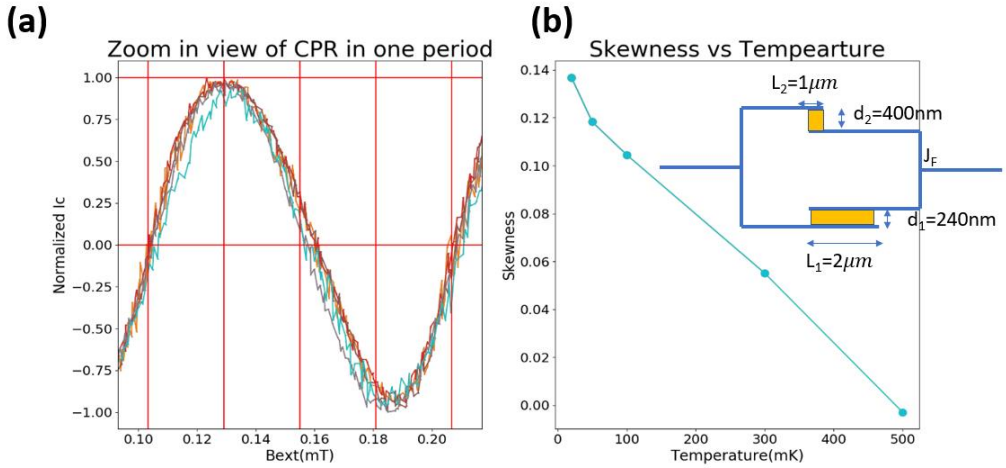

Figure 5.9: a) Zoom in view of one full period for the CPR of asymmetric SQUID at different temperatures. b) Calculated skewness dependence as a function of temperature with the asymmetric SQUID geometry in the inset.

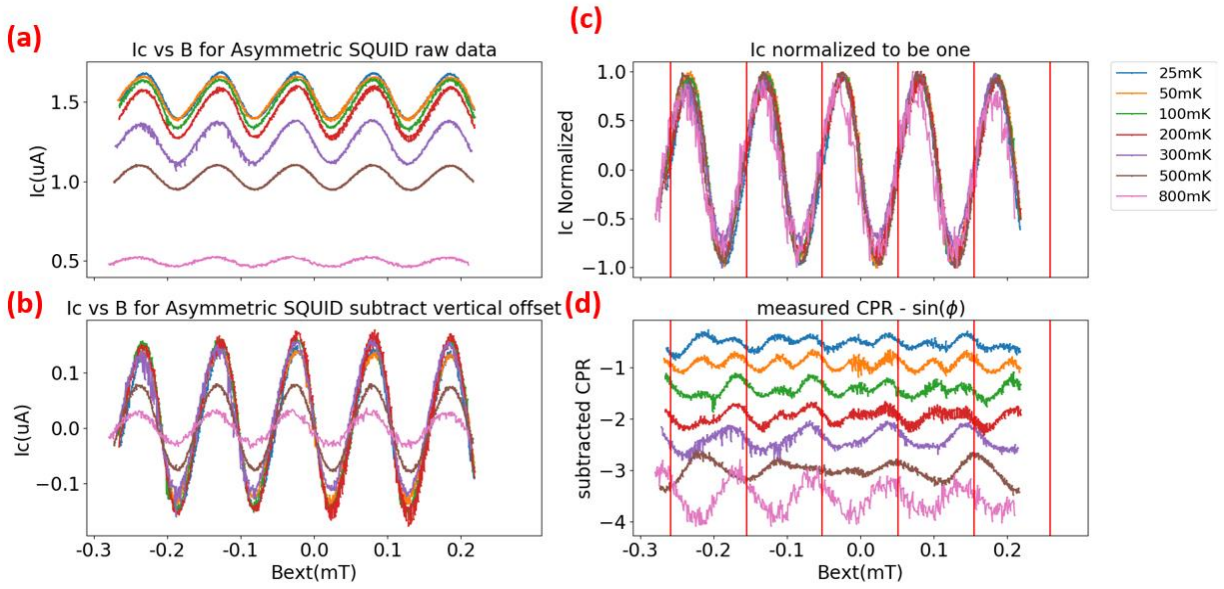

Figure 5.10: a) waterfall plot of CPR at different sample temperature with color encoded legend b) the vertical offset was subtracted to show the SQUID modulation amplitude at different sample temperature c) CPR was normalized to be 1 to calculate the skewness d) A 2π periodic CPR $sin(\phi)$ was subtracted from the measured CPR which would give us the unconventional CPR component

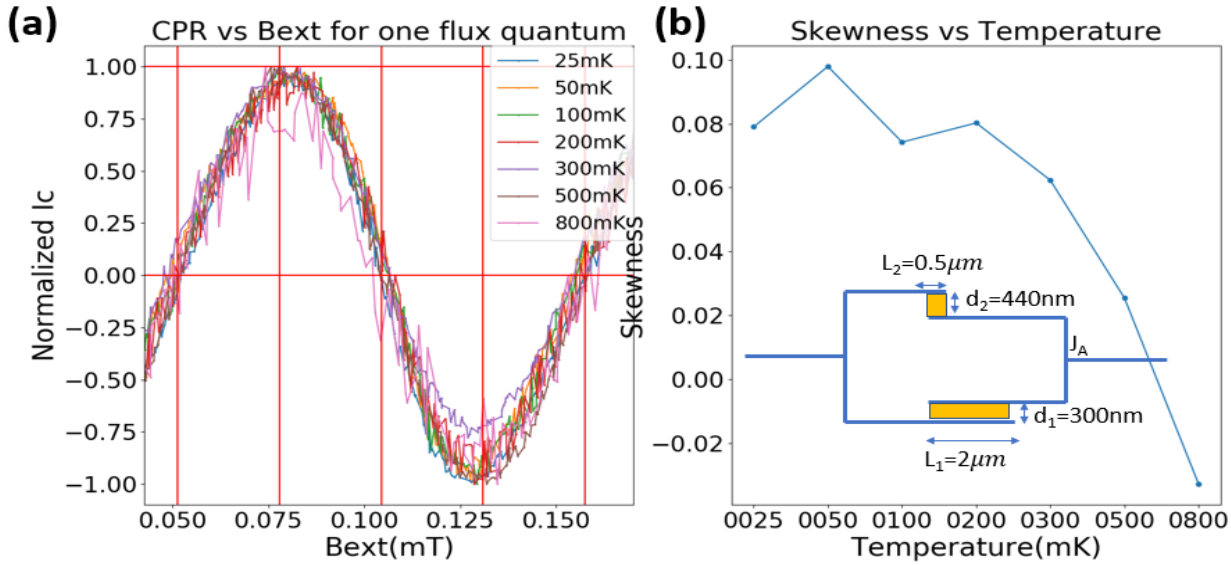

Figure 5.11: a) Zoom in view of one full period for the CPR of asymmetric SQUID at different temperatures. b) Calculated skewness dependence as a function of temperature with the asymmetric SQUID geometry in the inset.

However, we did not observe a $\sin\left(\frac{\phi}{2}\right)$ component in the CPR of our asymmetric SQUIDs. This could be because our measurement frequency is slower than the parity transition frequency of MBS, making us unable to resolve the 4pi periodic component of the CPR. High-frequency CPR measurement techniques such as measuring Shapiro steps would be necessary to explore the existence of $\sin\left(\frac{\phi}{2}\right)$ component in CPR of TIJJ.

We now discuss the mechanism for parity transition which prevents us from observing the unconventional 4π-periodic CPR in our TIJJ asymmetric SQUID. According to theorist Kitaev [19], the gapless ABS energy spectrum for a topological nontrivial Josephson junction 4π periodic if the system can preserve fermion parity. As we can see from Fig. 5.12 a), if one MF starts from the lower branch $(0, -\Delta_j)$ following the black arrow tracking along the blue line adiabatically, it will return to the same energy at $(4\pi, -\Delta_j)$ by staying on a single branch. However, in practice our devices are always connected to external leads and measurement electronics, creating a reservoir of quasiparticle. Therefore, it is not a strictly closed system. Quasiparticle electrons are always present in the environment, causing parity transition scattering. This effect is shown in Fig. 5.12 a) by a quasiparticle in a certain parity state, depicted by a red ball, transitions to another state when scattered by a quasiparticle electron, which changes the period from 4π to 2π. Such parity flip error effects are often referred to as the quasiparticle poisoning effect [78,79,80,81]. If our measurement frequency is slower than the quasiparticle scattering frequency, we would not able to see the MF tracing along the full 4π-periodic CPR. In order to see the full CPR, we would need to increase the frequency of the measurement such that the phase winding speed is much faster than the parity flip frequency, preserving fermion parity before parity switches. This would be the reason that we are able to observe high transmittance surface states in our TIJJ asymmetric SQUID

through observation of skewness, but we are unable to extract the exotic 4π-periodic Josephson effect from our asymmetric SQUID experiment.

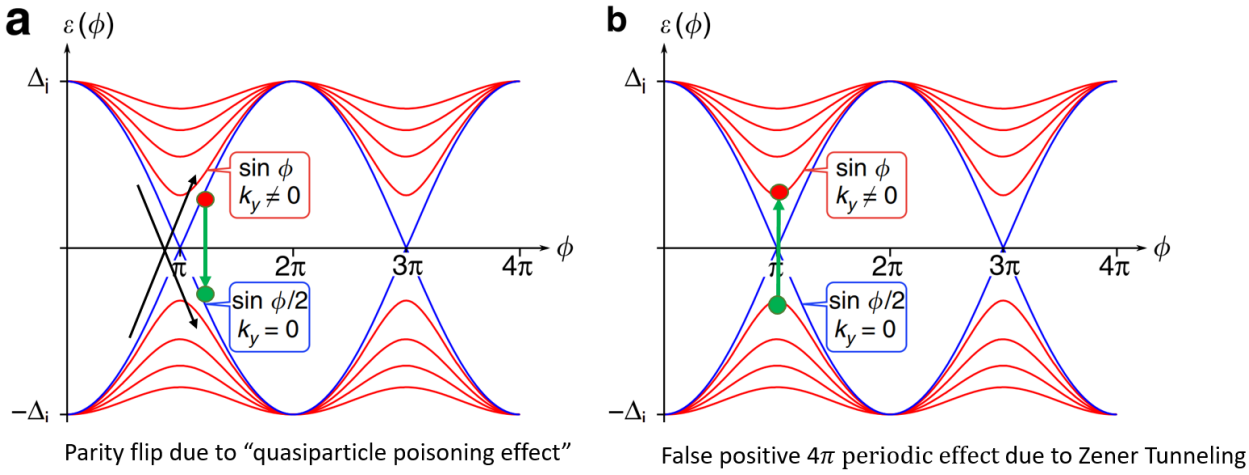

Figure 5.12: Energy dispersion spectrum of ABS as a function of Josephson phase difference and proximity induced gap energy Δ_j in 3D TIJJ system. The blue line depicts the gapless 4π-periodic CPR containing a $\sin\left(\frac{\phi}{2}\right)$ component, and the red line is the conventional gapped 2π-periodic CPR. a) Parity flip error due to quasiparticle poisoning effect" b) False positive 4π periodic Josephson effect due to Zener tunneling. [73]

Indeed, our results are consistent with direct CPR measurement on 3D TIJJ system using SSM pick-loop technique [71], where they only saw skewness in their TIJJ and not the $\sin\left(\frac{\phi}{2}\right)$ component in the CPR. High-frequency radio frequency (RF) techniques were employed to successfully capture the fractional Josephson effect in both HgTe single Josephson junctions and InAs nanowire Josephson junctions. However, we should be careful when interpreting the 4π-periodic Josephson effect as the proof of MFs, since such 4π-periodic Josephson effect can occur in conventional 2π-periodic Josephson system when the measurement speed is so fast that the quasiparticle can gain a large momentum and Zener tunnel through the gapped ABS spectrum shown in Fig. b). This gives a false positive signal for the non-trivial 4π-periodic Josephson effect,

since that quasiparticle does not obey non-Abelian statistics and cannot be used to build a fault-tolerant topological quantum computer.

Another possible explanation for being unable to resolve the $\sin\left(\frac{\phi}{2}\right)$ component in the CPR is that the contribution of $\sin\left(\frac{\phi}{2}\right)$ is too small be to visually observable in the CPR. Recall our simulated CPR data in Fig. a) when $\alpha = 0.2$. In hindsight, a dual-gate tunable asymmetric SQUID would be necessary to improve this experiment. As reported by previous literature, a top gate can shift the Fermi level of the topological non-trivial Josephson weak link barrier, thus tuning the contribution from the trivial surface states vs the topologically protected surface states. If we can deplete the carrier contribution from the trivial surface state, the transport behavior would then be dominated by the topologically protected surface state, which would potentially yield a large signal of the $\sin\left(\frac{\phi}{2}\right)$ component from the extracted CPR data in the asymmetric SQUID. The cleanest experiment to probe the unconventional 4π-periodic CPR remains an open question in the field of condensed matter physics.

5.3 Conclusion

We conducted direct CPR measurement of TIJJ by using an asymmetric SQUID technique. Numerical simulations were carried out to test the validity of this elegant, yet powerful technique. We observed skewness in all our TIJJ asymmetric SQUID junctions, which can be attributed to the high transparency surface states of the high-quality 3D topological insulator Bi_2Se_3. We found that skewness decreases as a function of increasing sample temperature, which is caused by thermal scattering effect between surface state electrons and bulk state electrons, thus effectively reducing the Josephson barrier transparency. A topologically non-trivial 4π-periodic CPR was not observed, which shows a discrepancy from our single junction diffraction data, and this could be possibly due to quasiparticle poisoning effects. A more carefully designed experiment, such as a local CPR measurement free from contact leads and external quasiparticle reservoirs would potentially isolate the measurement system from quasiparticle poisoning effect. A faster measurement technique, for example, a high-frequency RF-technique, or switching current distribution experiment are also promising candidate experiments to probe such exotic 4π-periodic CPR.

Chapter 6 Conclusions and Future Directions

In this thesis, we have carried out a systematic study of Nb-Bi_2Se_3-Nb lateral Josephson junctions, and main effort of this thesis is trying to study the 4π periodic Josephson effect in TIJJ inspired by the Fu and Kane model. Two different experiments techniques were used to study the 4π periodic Josephson effect in TIJJ.

For project 1, we studied the TIJJ single junction diffraction pattern and observing a consistent even-odd node-lifting effect in our junctions, we have tested the origin of such phenomenon caused by critical current disorder with numerical simulations. First, it takes a significant amount of random disorder to have a noticeable amount of node-lifting in the diffraction patter based on our simulation. With the simple design of our long and thin bar type of junctions, we knew our junction have quite straight parallel edges to have a uniform critical current density distribution along the edge of the junction. Secondly, disorder would lift all the nodes and would not have even-odd node lifting effect, whereas a very small contribution of $\sin\left(\frac{\phi}{2}\right)$ component in the critical current would show significant even-odd node-lifting effect. Furthermore, the even-odd node-lifting are consistent for many of our single TIJJ samples, ruling out anomalous device-specific origins. It is so robust that we observed it in many different forms of Bi_2Se_3 samples, including MBE grown thin films involved in this thesis, and exfoliated flakes from Bi_2Se_3 bulk crystals reported by previous literature. Furthermore, we observed a vortex entry feature in our single junction diffraction pattern, which we attributed to the localized zero-energy MBS carrying extra current.

For project 2, we have used a direct electrical transport method to measure the CPR of our TIJJ using asymmetric SQUID technique. We have observed skewness in our TIJJ, which is

attributed to the high transparency surface state in TI. We also noticed that skewness decreases as we increase the sample temperature, which can be explained by thermal electrons interfering with surface state electrons as we increase the sample temperature. However, we did not observe a pronounced featured in our CPR data corresponding with $\sin\left(\frac{\phi}{2}\right)$, and this is not consistent with our single junction diffraction data with even-odd node-lifting effect. This might have to do with quasiparticle poising effect induced parity transition, which hindering us from seeing the whole 4π periodic CPR. To see such exotic 4π periodic CPR, we need to increase our measurement speed such that the MBS can stay on a single branch of the double-valued ABS spectrum. To do so, high-frequency RF-technique would be helpful to investigate this 4π periodic CPR. High speed switching current distribution experiment would be also useful to specifically probing such parity transition effect in TIJJ.

In short, we would like to conclude that we observed 4π periodic Josephson effect in our Nb-Bi_2Se_3-Nb lateral single junctions, supported by even-odd node-lifting effect and abrupt vortex entry feature in our single junction diffraction patterns. To further confirm such 4π periodic Josephson effect, we conducted direct CPR measurement by employing asymmetric SQUID technique, however we didn't detect the $\sin\left(\frac{\phi}{2}\right)$ component in our measured CPR data, which might be caused by quasiparticle scattering induced parity transition.

Citations and References

1 https://en.wikipedia.org/wiki/Dirac_equation

2 https://en.wikipedia.org/wiki/Positron

3 F. Wilczek, “Majorana Returns”, Nature Physics, Volume 5, Issue 9, pp. 614-618 (2009)

4 A. Y. Kitaev, “Fault-tolerant quantum computation by anyons” , Ann. Phys. 303, 2 (2003).

5 J Preskill , “Fault-tolerant quantum computation”, arXiv:quant-ph/9712048 (1997)

6 M. Tinkahm, “Introduction to Superconductivity”, (Dover Books on Physics) (Vol i) (14 June 2004)

7 M. Z. Hasan and C. L. Kane, “Colloquium: Topological insulators”, Rev. Mod. Phys., Vol. 82, No. 4, (2010)

8 J. Alicea, “New directions in the pursuit of Majorana fermions in solid state systems”, Rep. Prog. Phys. 75, 076501 (2012)

9 C.W. Beenakker, “Search for Majorana Fermions in superconductors”, Annu. Rev. Con. Mat. Phys. 4, 113 (2013)

10 N. Read, D. Green, “Paired states of fermions in two dimensions with breaking of parity and time-reversal symmetries and the fractional quantum Hall effect”, Phys. Rev. B 61, 10267

11 A.J. Leggett, “A theoretical description of the new phases of liquid 3He”,
Rev. Mod. Phys. 48, 357

12 J. Jang et al, “Observation of Half-Height Magnetization Steps in Sr2RuO4”, Science 331, 186 (2011)

13 A. P. Mackenzie, A. K. W Haselwimmer, A. W. Tyler , G. G. Lonzarich , Y. Mori , S. Nishizaki , Y. Maeno, "Extremely Strong Dependence of Superconductivity on Disorder in Sr_2RuO_4" .Phys. Rev. Lett. 80, 161 (1998)

14 J. D. Sau, R. M. Lutchyn, S. Tewari, and S. Das Sarma Phys. "Generic New Platform for Topological Quantum Computation Using Semiconductor Heterostructures". Rev. Lett. 104, 040502 (2010).

15 V. Mourik, K. Zuo, S. M. Frolov, S. R. Plissard, E. P. A. M. Bakkers, and L. P. Kouwenhoven, "Signatures of Majorana Fermions in Hybrid Superconductor-Semiconductor Nanowire Devices", Science 336, 1003 (2012)

16 M.T. Deng, S Vaitiekėnas, E.B. Hansen, J. Danon, M. Leijnse, K. Flensberg, J. Nygård, P. Krogstrup, C. Marcus "Majorana bound state in a coupled quantum-dot hybrid-nanowire system" , Science 354 (6319), 1557-1562

17 A.D.K. Finck, D.J. Van Harlingen, P.K. Mohseni, K. Jung, X. Li, "Anomalous modulation of a zero-bias peak in a hybrid nanowire-superconductor device", Phys. Rev. Lett. 110 (12), 126406

18 L. Fu, C.L. Kane, "Superconducting Proximity Effect and Majorana Fermions at the Surface of a Topological Insulator", Phys. Rev. Lett. 100, 096407 (March 2008)

19 A. Y. Kitaev, "Unpaired Majorana fermions in quantum wires", Phys.Usp. 44 (2001) no.10S, 131-136

20 https://en.wikipedia.org/wiki/Heike_Kamerlingh_Onnes

21 J. Bardeen, L.N. Cooper, and J.R. Schrieffer, “Microscopic Theory of Superconductivity” ,Phys. Rev. 106, 162 (1957)

22 J. Bardeen, L. N. Cooper, and J. R. Schrieffer, “Theory of Superconductivity”, Phys. Rev. 108, 1175 (1957)

23 A.P. Mackenzie, Y. Maeno, “ p-wave superconductivity”, Physica B: Physics of Condensed Matter, Volume 280, Issue 1-4, p. 148-153

24 J.G. Bednorz, A. Muller, “Possible high T_c superconductivity in the Ba-La-Cu-O system”, Z. Physik, B 64, 189 (1987).

25 A. Lebed, Springer Series in Materials Science 10, 1 (2008).

26 H. Takahashi, K. Igawa , K. Arii ,Y. Kamihara , M. Hirano , H. Hosono , “Superconductivity at 43 K in an iron-based layered compound $LaO_{1-x}F_xFeAs$”, Nature 453, 376 (2008)

27 W.L. McMillan, “Transition Temperature of Strong-Coupled Superconductors”,Phys. Rev. 167, 331 (1968)

28 B. D. Josephson (1962). "Possible new effects in superconductive tunneling". Phys. Lett. 1 (7): 251–253

29 E. Berg, E. Fradkin, S. Kilvelson, “Charge-4*e* superconductivity from pair-density-wave order in certain high-temperature superconductors”, Nature Physics 5, 830–833 (2009)

30 Duzer, Theodore Van, and C. W. Turner. Principles of Superconductive Devices and Circuits. Prentice Hall, 1999

31 R. Gross, A. Marx “Applied Superconductivity: Josephson Effect and Superconducting Electronics”, Chpater 4

32 G. Nanda, J. L. Aguilera-Servin, P. Rakyta, A. Kormányos, R. Kleiner, D. Koelle, K. Watanabe, T. Taniguchi, L. M. K. Vandersypen, and S. Goswami, "Current-Phase Relation of Ballistic Graphene Josephson Junctions", *Nano Lett.*, **2017**, *17* (6), pp 3396–3401

33 C. D. English, D. R. Hamilton, C. Chialvo, I. C. Moraru, N. Mason, and D. J. Van Harlingen,

"Observation of nonsinusoidal current-phase relation in graphene Josephson junctions ", Phys. Rev. B 94, 115435 (2016)

34 C. W. Hicks, T. M. Lippman, M. E. Huber, J. G. Analytis, J. H. Chu, A. S. Erickson, I. R. Fisher, and K. A. Moler, "Evidence for a Nodal Energy Gap in the Iron-Pnictide Superconductor LaFePO from Penetration Depth Measurements by Scanning SQUID Susceptometry" ,Physical Review Letters 103 127003 (2009)

35 H. Weng, X. Dai, and Z. Fang, "Exploration and Prediction of Topological Electronic Materials Based on First Principles Calculations" , MRS Bull. 39, 849 (2014).

36 C. Kane, E. Mele, "A New Spin on the Insulating State", Science 15 Dec 2006: Vol. 314, Issue 5806, pp. 1692-1693 DOI: 10.1126/science.1136573

37 H. Shi, D. Parker, M. Du, D. Singh, "Connecting Thermoelectric Performance and Topological-Insulator Behavior: Bi2Te3 and Bi2Te2Se from First Principles" , Physical Review Applied, Volume 3, Issue 1, id.014004

38 F. Pollmann, E. Berg, A. M. Turner, and M. Oshikawa, "Symmetry protection of topological phases in one-dimensional quantum spin systems", Phys. Rev. B 85, 075125 (2012)

39 X. Chen, Z.C. Gu, Z.X. Liu, X.G. Wen, "Symmetry-Protected Topological Orders in Interacting Bosonic Systems" , Science 21 Dec 2012: Vol. 338, Issue 6114, pp. 1604-1606

40 Th. Guhr, A. Müller-Groening, H.A. Weidenmüller, “Random-matrix theories in quantum physics: common concepts”, Phys.Rept.299:189-425,1998

41 https://en.wikipedia.org/wiki/Topological_insulator

42 X.L. Qi and S.C. Zhang, “Topological insulators and superconductors”, Rev. Mod. Phys. 83, 1057 (2011)

43 https://mappingignorance.org/2016/12/22/manipulating-topological-surface-states-molecular-adsorbates/

44 Y.L. Chen, J. Analytis, J.-H. Chu, Z. Liu, S.-K. Mo, X.-L. Qi, H. Zhang, D. Lu, X. Dai, and Z. Fang, “Experimental Realization of a Three-Dimensional Topological Insulator, Bi_2Te_3”, Science 325, 178 (2009)

45 http://hk-phy.org/articles/refrigerator/refrigerator_e.html

46 http://cdms.berkeley.edu/UCB/75fridge/inxsrc/dilution/index.html#1

47 https://www.ulvac.co.jp/wiki/en/4k-cryocooler/

48 G. Batey, M, Buehler, M, Cuthbert, T. Foster, A.J. Matthews, G. Teleberg, A. Twin, “Integration of superconducting magnets with cryogen-free dilution refrigerator systems ”, Elsevier Cryogenics 49 727–734 (2009)

49 M. Veldhorst, M. Snelder, M. Hoek, T. Gang, V.K. Guduru, X.L. Wang, U. Zeitler, W.G. van der Wiel, A.A. Golubov, H. Hilgenkamp, and A. Brinkman, “Josephson supercurrent through a topological insulator surface state”, Nat. Mater. 11, 417 (2012).

50 S. Cho, B. Dellabetta, A. Yang, J. Schneeloch, Z. Xu, T. Valla, G. Gu, M.J.Gilbert, N. Mason, “Symmetry protected Josephson supercurrents in three-dimensional topological insulators”, Nat.Commun. 4, 1689 (2012).

51 B. Sacepe, J.B. Oostinga, J. Li, A. Ubaldini, N.J.G. Couto, E. Giannini, and A.F. Morpurgo, "Gate-tuned normal and superconducting transport at the surface of a topological insulator", Nat. Commun. 2, 575 (2011).

52 D. Zhang, J. Wang, A.M. DaSilva, J.S. Lee, H.R. Gutierrez, M.H. W. Chan, J. Jain, and N. Samarth, "Superconducting proximity effect and possible evidence for Pearl vortices in a candidate topological insulator", Phys. Rev. B 84, 165120 (2011).

53 L. Galletti, S. Charpentier, M. Iavarone, P. Lucignano, D. Massarotti, R. Arpaia, Y. Suzuki, K. Kadowaki, T. Bauch, A. Tagliacozzo, F. Tafuri, and F. Lombardi, "Influence of topological edge states on the properties of Al/Bi2Se3/Al hybrid Josephson devices", Phys. Rev. B 89, 134512 (2014).

54 P. Zareapour, A. Hayat, S.Y. F. Zhao, M. Kreshchuk, A. Jain, D.C. Kwok, N. Lee, S.-W. Cheong, Z. Xu, A. Yang, G.D. Gu, S. Jia, R.J. Cava, and K.S. Burch, "Proximity-induced high-temperature superconductivity in the topological insulators Bi_2Se_3 and Bi_2Te_3", Nat. Commun. 3, 1056 (2012).

55 L. Maier, J.B. Oostinga, D. Knott, C. Brüne, P. Virtanen, G. Tkachov, E.M.Hankiewicz, C. Gould, H. Buhmann, and L.W. Molenkamp, "Induced Superconductivity in the Three-Dimensional Topological Insulator HgTe", Phys. Rev. Lett. 109, 186806 (2012).

56 F. Qu, F. Yang, J. Shen, Y. Ding, J. Chen, Z. Ji, G. Liu, J. Fan,X. Jing, C. Yang, and L. Lu, "Strong Superconducting Proximity Effect in Pb-Bi_2Te_3 Hybrid Structures" ,Sci. Rep. 2, 339 (2011).

57 F. Yang, F. Qu, J. Shen, Y. Ding, J. Chen, Z. Ji, G. Liu, J. Fan, C. Yang, L. Fu, and L. Lu, "Proximity-effect-induced superconducting phase in the topological insulator Bi_2Se_3", Phys. Rev. B 86, 134504 (2012).

58 J.B. Oostinga, L. Maier, P. Schüffelgen, D. Knott, C. Ames, C. Brüne, G. Tkachov, H. Buhman, L.W. Molenkamp, "Josephson Supercurrent through the Topological Surface States of Strained Bulk HgTe",Phys. Rev. X 3, 021007 (2013).

59 C. Kurter, A. D. K. Finck, P. Ghaemi, Y. S. Hor, D. J. Van Harlingen, "Dynamical gate-tunable supercurrents in topological Josephson junctions", Phys. Rev. B 90, 014501 (2014)

60 V. Orlyanchik, M. P. Stehno, C. D. Nugroho, P. Ghaemi, M. Brahlek, N. Koirala, S. Oh, and D. J. Van Harlingen. "Signature of a topological phase transition in the Josephson supercurrent through a topological insulator",Phys. Rev. B 93, 035307 (2016)

61 Y. S. Hor, A. Richardella, P. Roushan, Y. Xia, J. G. Checkelsky, A. Yazdani, M. Z. Hasan, N. P. Ong, and R. J. Cava, "p-type Bi_2Se_3 for topological insulator and low-temperature thermoelectric applications", Phys. Rev. B 79, 195208 (2009)

62 F.-T. Huang, M.-W. Chu, H. H. Kung, W. L. Lee, R. Sankar, S.-C. Liou, K. K. Wu, Y. K. Kuo, and F. C. Chou, "Nonstoichiometric doping and Bi antisite defect in single crystal Bi_2Se_3",Phys. Rev. B 86, 081104(R) – (2012)

63 YS Kim, M Brahlek, N Bansal, E Edrey, GA Kapilevich, K Iida, M Tanimura, "Thickness-dependent bulk properties and weak antilocalization effect in topological insulator Bi2Se3". Physical Review B 84 (7), 073109

64 B. Mulcahy, "The superconducting proximity effect in Bi_2Se_3 thin-films", PhD Thesis, UIUC, 2015 page 17

65 J. Horak, Z, Stary, P. Lostak, J. Pancir , “Anti-site defects in n-Bi2Se3 crystals”,Journal of Physics and Chemistry of Solids, vol. 51, issue 12, pp. 1353-1360

66 J. Analytis, R.D. McDonald, S.C. Riggs, J.H. Chu, G.S. Boebinger, I.R. Fisher, “Two-dimensional surface state in the quantum limit of a topological insulator ”, Nat. Phys. 2010, 6, 960−964.

67 Z. Ren, A.A. Taskin, S. Sasaki, K. Segawa, Y. Ando, “Optimizing $Bi_{2-x}Sb_xTe_{3-y}Se_y$ solid solutions to approach the intrinsic topological insulator regime”, Phys. Rev. B 84, 165311 (2011)

68 N. Koirala, M. Brahlek, M. Salehi, L. Wu, J. Dai, J. Waugh, T. Nummy, M. Han, J. Moon, Y. Zhu, D. Dessau, W. Wu, N. P. Armitage, S. Oh, “Record Surface State Mobility and Quantum Hall Effect in Topological Insulator Thin Films via Interface Engineering”, Nano Lett. 15, 8245–8249 (2015)

69 J.R. Williams, A.J. Bestwick, P. Gallagher, S.S. Hong, Y. Cui, A.S. Bleich, J.G. Analytis, I.R. Fisher, and D. Goldhaber-Gordon, “Unconventional Josephson Effect in Hybrid Superconductor-Topological Insulator Devices ”,Phys.Rev.Lett.109,056803(2012).

70 A.C. Potter and L. Fu Phys. “Anomalous supercurrent from Majorana states in topological insulator Josephson junctions”. Rev. B 88, 121109(R) (2013)

71 http://ncore.jku.at/pcar.php

72 J-D. Pillet, C. H. L. Quay1, P. Morfin, C. Bena, A. Levy Yeyati and P. Joyez, "Andreev bound states in supercurrent-carrying carbon nanotubes revealed", *Nature Physics* **6**, 965–969 (2010)

73 C Kurter, ADK Finck, YS Hor, DJ Van Harlingen. "Evidence for an anomalous current–phase relation in topological insulator Josephson junctions".Nature Communications 6, 7130

74 I. Sochnikov, A.J. Bestwick, J.R. Williams, T.M. Lippman, I.R. Fisher, D. Goldhaber-Gordon, J.R. Kirtley, and K.A. Moler. "Direct Measurement of Current-Phase Relations in Superconductor/Topological Insulator/Superconductor Junctions". *Nano Letters*, 2013, 13 (7), pp 3086–3092

75 I. Sochnikov, L. Maier, C.A. Watson, J.R. Kirtley, C. Gould, G. Tkachov, E.M. Hankiewicz, C. Brüne, H. Buhmann, L.W. Molenkamp, and K.A. Moler. "Nonsinusoidal Current-Phase Relationship in Josephson Junctions from the 3D Topological Insulator HgTe". Phys. Rev. Lett. 114, 06680

76 J. Wiedenmann et al., "4π-periodic Josephson supercurrent in HgTe-based topological Josephson junctions". Nat. Commun. 7, 10303 (2016)

77 Leonid P. Rokhinson, Xinyu Liu, and Jacek K. Furdyna "The fractional a.c. Josephson effect in a semiconductor–superconductor nanowire as a signature of Majorana particles ".*Nature Physics* 8, 795–799 (2012)

78 L. Fu, C. Kane, "Josephson current and noise at a superconductor/quantum-spin-Hall-insulator/superconductor junction". Phys. Rev. B 2009, 79, 161408(R)

79 R. Lutchyn, J, Sau, S. Das Sarma, "Majorana fermions and a topological phase transition in semiconductor-superconductor heterostructures". Phys. Rev. Lett. 2010, 105, 077001

80 D. Rainis, D. Loss, “Majorana qubit decoherence by quasiparticle poisoning”. Phys. Rev. B 2012, 85, 174533

81 B. van Heck, F. Hassler, A. Akhmerov, C. Beenakker, “Coulomb stability of the 4 pi-periodic Josephson effect of Majorana fermions”. Phys. Rev. B 2011, 84, 180502(R)